

University of Louisville

ThinkIR: The University of Louisville's Institutional Repository

Electronic Theses and Dissertations

1-2022

Engineering Lewis acidic materials for biomass conversion and battery applications.

Md Anwar Hossain
University of Louisville

Follow this and additional works at: <https://ir.library.louisville.edu/etd>



Part of the [Catalysis and Reaction Engineering Commons](#), and the [Other Chemical Engineering Commons](#)

Recommended Citation

Hossain, Md Anwar, "Engineering Lewis acidic materials for biomass conversion and battery applications." (2022). *Electronic Theses and Dissertations*. Paper 3826.
<https://doi.org/10.18297/etd/3826>

This Doctoral Dissertation is brought to you for free and open access by ThinkIR: The University of Louisville's Institutional Repository. It has been accepted for inclusion in Electronic Theses and Dissertations by an authorized administrator of ThinkIR: The University of Louisville's Institutional Repository. This title appears here courtesy of the author, who has retained all other copyrights. For more information, please contact thinkir@louisville.edu.

ENGINEERING LEWIS ACIDIC MATERIALS FOR BIOMASS CONVERSION AND
BATTERY APPLICATIONS

By

Md. Anwar Hossain

B.S. (Chemical Engineering) Shahjalal University of Science and Technology, 2013

M.S. (Chemical Engineering) The University of Louisville, 2020

A Dissertation

Submitted to the J.B. Speed School of Engineering of the University of Louisville

in Partial Fulfillment of the Requirements

for the Degree of

Doctor of Philosophy

in Chemical Engineering

Department of Chemical Engineering

University of Louisville

Louisville, Kentucky

May 2022

Copyright 2022 by Md. Anwar Hossain

All right reserved

ENGINEERING LEWIS ACIDIC MATERIALS FOR BIOMASS CONVERSION AND
BATTERY APPLICATIONS

By

Md. Anwar Hossain

B.S. (Chemical Engineering) Shahjalal University of Science and Technology, 2013

M.S. (Chemical Engineering) The University of Louisville, 2020

A Dissertation Approved on

March 23, 2022

by the following Dissertation Committee:

Dr. Noppadon Sathitsuksanoh

Dr. Gerold A. willing

Dr. Vance W. Jaeger

Dr. Lee Thompson

DEDICATION

To my Mother.

ACKNOWLEDGEMENTS

I am most grateful to my parents, siblings, and family members. They always believe in me and provide unconditional love and encouragement throughout my academic journey.

First, I would like to express my deepest and most sincere gratitude to Dr. Noppadon Sathitsuksanoh, my advisor, for allowing me to learn more than the classroom could ever teach. He trained me to think beyond textbook concepts and challenge myself. I appreciate his understanding, encouragement, and support in these last five years. Also, I would like to thank my committee members, Profs. Gerold Willing, Lee Thompson, and Vance Jeager for their guidance throughout my dissertation.

Second, I would like to thank Drs. Teerawit Prasomsri, Sarttrawut Tulaphol, Than Khoa Phung, and Prof. Shashi Lalvani for their guidance and insightful discussions about my projects. Also, I want to thank Drs. Jacek Jasinski, Hui Wang, and Arjun Thapa for their support and training on material characterization and battery testing techniques, and Drs. Supareak Prasertdam and Thana Maihom for their help with Density Functional Theory calculations to elucidate the chemical pathways of lignin conversion and ionic diffusion in battery electrolytes.

Last but not least, I want to thank Mohammad Shahinur Rahaman, my friend, fellow lab member, and collaborator on various projects. Also, I would like to thank my friends, Riyad, Sharmin, Omor Sadi, Dr. Musa, Tasnim Kazi, Dr. Mamun, Dr. Ekramul Islam, Dr. Rocky, Dr. Paul, Susana, and Saumya for being there for me for the past five years.

ABSTRACT

ENGINEERING LEWIS ACIDIC MATERIALS FOR LIGNIN UPCYCLING AND HIGH-PERFORMANCE LITHIUM METAL BATTERIES

Md. Anwar Hossain

March 23, 2022

My long-term goal is to develop catalytic systems to produce renewable energy for a sustainable society. The overall research objective of my dissertation is to advance understanding of Lewis acidic materials for (1) conversion of renewable lignin into phenolics and (2) enhanced cycling stability of lithium metal batteries to safely store renewable electricity from wind and solar, thereby laying the groundwork for our transition to a sustainable society.

Petroleum is a conventional feedstock for current transportation fuels (gasoline, diesel, and jet fuels). However, petroleum is a finite resource and produces greenhouse gases (CO_2 and CH_4) upon processing, which contributes to climate change. Therefore, we need to develop ways to tap into alternative feedstocks. Many researchers have investigated the use of catalytic conversion of lignocellulosic biomass to produce biofuels (bioethanol). During bioethanol production, carbohydrates (cellulose and hemicellulose) are digested to produce bioethanol. The residual lignin is left behind. The ability to catalytically convert lignin into high-value chemicals will incentivize biorefineries and promote a sustainable bioeconomy.

Electricity is another renewable energy that can be produced from wind and solar. The major challenge in using electricity-driven transportations (electric vehicles) lies in their storage in lithium metal batteries. However, chemical and electrochemical reactions in conventional lithium-metal batteries are not stable.

The movement of undesired anions promotes capacity decay and hazardous lithium dendrite growth. As a result, these batteries have short lives and short-circuiting, which leads to fire and explosion. The ability to control the reactivity of the ions in the electrolytes will enable safety and promote future electric vehicles for a cleaner environment. My dissertation focuses on the development of Lewis acidic materials to address the challenges in (1) lignin upcycling and (2) the safety and cyclability of lithium metal batteries. First, lignin is an oxygen-rich phenolic polymer. To efficiently release the phenolic monomers from lignin, I developed the Lewis acid catalysts in the form of oxygen vacancies to activate the oxygen functionality of lignin. Second, I grafted the Lewis acidic metal-organic frameworks (MOFs) onto the polypropylene separator to immobilize the TFSI anions in conventional electrolytes (1M LiTFSI in organic solvents). The developed materials restrict the mobility of anions and polyselenides, thereby improving the lithium-selenium batteries' capacity retention and cycling stability.

I divided this dissertation into six chapters to cover background about Lewis acidic materials and their uses for catalytic lignin upgrading and lithium-selenium batteries. The first four chapters of this dissertation describe the engineering/development of the Lewis acidic material for the catalysis of bioderived organics, lignin. Then, chapter five describes the incorporation of the Lewis acidic MOFs into a polypropylene separator to improve battery capacity and safety. Incorporating the Lewis acidic MOFs controlled ion transport properties, thereby restricting the mobility of undesired anions and polyselenides and improving capacity retention in lithium-selenium batteries. Finally, Chapter six suggests future research directions to create next-generation alkali metal-based batteries that are safe and powerful to face future challenges for developing a sustainable carbon zero society.

TABLE OF CONTENTS

	Page
Acknowledgments.....	iii
Abstract	iv
List of Tables	x
List of Figures	xii
Chapter 1. Introduction	1
Chapter 2. Catalytic Isomerization of dihydroxyacetone to lactic acid by heat-treated zeolites	4
Introduction.....	4
Material and methods.....	7
Results.....	9
Discussion.....	16
Conclusion	19
Supporting information.....	20
Chapter 3. Catalytic cleavage of the β -O-4 aryl ether bonds of lignin model compounds by Ru/C catalyst	25
Introduction.....	25
Material and methods.....	27
Results and discussion	30
Conclusion.....	39
Supporting information.....	40

Chapter 4. Unlocking self-hydrogen for hydrogenolysis of lignin by a dual function	
Ru/RuOx/C catalyst	45
Introduction.....	45
Material and methods.....	46
Results.....	49
Discussion.....	60
Conclusion.....	63
Supporting information.....	64
Chapter 5. Metal-organic framework separator as polyselenide filter for high-performance lithium-selenium batteries	82
Introduction.....	82
Material and methods.....	84
Results.....	89
Discussion.....	100
Conclusion.....	102
Supporting information.....	103
Chapter 6. Conclusion and Future work.....	113
References	114
Appendices	135
Curriculum Vitae	137

LIST OF TABLES

	Page
Chapter 2	
Table 1. Physical properties and acid densities of catalysts.....	11
Table S1. List of chemicals/reagents used in this study.....	20
Table S2. Catalytic performance of selected Zeolite catalysts.....	20
Table S3. Catalytic performance of selected solid catalysts	21
Chapter 3	
Table 1. Conversion and Product selectivity of PPE and PPE-OH hydrogenolysis.....	35
Table S1. List of chemicals/reagents used in this study.....	40
Table S2. Pretreatment conditions for the Ru/C catalyst.....	41
Table S3. The Ru and RuO ₂ content (mol.%) calculated from H ₂ -TPR.....	41
Table S4. Composition of the Ru/C catalysts calculated from H ₂ -TPR and TGA.....	42
Table S5. Conversion and product selectivity of the PPE and PPE-OH	42
Table S6. Conversion and product selectivity as a function of reaction time.....	43
Table S7. Conversion and product selectivity as a function of Ru content.....	44
Chapter 4	
Table 1. Enthalpy (ΔH) in eV of direct PPE and PPE-OH hydrogenolysis	55
Table 2. Acetophenone conversion by Ru/RuO _x /C in ethanol and dioxane.....	57
Table S1. List of chemicals/reagents used in this study.....	64
Table S2. Important atomic distances in PPE and PPE-OH molecules.....	70

Table S3. Atomic Bader charge change of essential atoms.....	74
Table S4. Ru and RuO _x content of the used Ru/RuO _x /C catalyst.....	78
Table S5. Meerwein–Ponndorf–Verley (MPV) reduction of acetophenone.....	79
Table S6. Hydrogenolysis of the real lignin over Ru/RuO _x /C catalyst.....	80
Table S7. Relative integrals of the C _α -OH and C _α =O peaks in four technical lignin.....	81

Chapter 5

Table S1. Chemicals and supplies used in this work.....	103
Table S2. FTIR peak assignments.....	107
Table S3. Charge transfer resistance (R ₂) and Warburg resistance (W ₂)	108
Table S4. Diffusion coefficient of lithium ion (D _{Li+}) for	109
Table S5. Selected separators used in lithium-selenium batteries.....	110
Table S6. Selected metal-organic framework-based separators for battery systems.....	111

LIST OF FIGURES

	Page
Chapter 2	
Figure 1. Graphical abstract of catalytic Isomerization of dihydroxyacetone	4
Figure 2. Scheme of chemical pathway for lactic acid production.....	5
Figure 3. XRD (A) and FTIR (B) spectra of modified ZSM-5	10
Figure 4. Product evolution of the dihydroxyacetone isomerization	13
Figure 5. Product evolution of pyruvaldehyde rehydration.....	15
Figure 6. TGA and DTG profiles of the spent catalysts.....	16
Figure 7. Proposed chemical pathway for the dihydroxyacetone conversion.....	18
Figure S1. XRD spectra of the modified ZSM-5 at differetn treatment temperature....	21
Figure S2. N ₂ adsorption/desorption isotherm of the modified XSM-5 catalyst.....	22
Figure S3. TGA Profile of the ZSM-5 with adsorbed n-propylamine.....	22
Figure S4. Product evolution of dihydroxyacetone isomerization.....	23
Figure S5. DRIFT spectra of adsorbed pyridine (Py) on modified ZSM-5.....	23
Figure S6. Thermal stability of lactic acid by modified ZSM-5	24

Chapter 3

Figure 1. Graphical abstract of catalytic cleavage of the β -O-4 aryl ether bonds	25
Figure 2. An example of truncated (poplar) lignin structure.....	27
Figure 3. H ₂ -TPR profiles of Ru/C catalyst from different pretreatment conditions.....	32
Figure 4. XRD patterns of investigated catalysts. Note: metallic Ru (○) and RuO ₂ (*)..	34
Figure 5. The proposed reaction pathway of hydrogenolysis of PPE-OH over Ru/C....	36
Figure S1. Changes in H ₂ -TPR profiles of Ru/C after reduction and passivation.....	41
Figure S2. H ₂ -TPR profiles of the Ru/C catalyst over reaction time.....	43
Figure S3. H ₂ -TPR profiles of the spent Ru/C catalyst after four recycles.....	44

Chapter 4

Figure 1. Cleavage of β -O-4 linkages of veratrylglycerol- β -guaiacyl ether.....	51
Figure 2. Mechanistic study of the hydrogenolysis of O1-C1 bond on Ru(111).....	54
Figure 3. Cleavage of the β -O-4 bond of PPE-OH, (1b) by Ru/Ru _x /C	56
Figure 4. Hydrogenolysis of the technical lignin over Ru/RuO _x /C catalyst.....	59
Figure 5. Correlation between total C _{α} integral and hydrogenolysis yield	60
Figure 6. Proposed reaction pathway for conversion of model β -O-4 compounds.....	63
Figure S1. The optimized geometry of the isolated adsorbate molecules	67
Figure S2. Slab model of Ru(111) surface projected along the (010)-direction	67
Figure S3. Optimized structures in the top and side view of PPE and PPE-OH	71
Figure S4. Cleavage of β -O-4 bond of veratrylglycerol- β -guaiacyl ether.....	71
Figure S5. Cleavage of β -O-4 bond of veratrylglycerol- β -guaiacyl ether by Bulk Ru....	72

Figure S6. The charge density difference cross-sectional profile at the Ru(111).....	73
Figure S7. Evolution profiles of reaction products from cleavage of β -O-4.....	76
Figure S8. Cleavage of the β -O-4 bond of PPE-OH (1b) by Ru/RuO _x /C in 2-propanol..	77
Figure S9. Relationship between donor number and the selectivity toward	78
Figure S10. Portions of the HSQC NMR spectra for the technical lignin.....	80

Chapter 5

Figure 1. Illustration of flexible MOF separator and physical properties.....	90
Figure 2. Permeation tests of polypropylene and PCN separator.....	92
Figure 3. Changes of current with time during polarization of a Li/Li symmetric cell.....	93
Figure 4. Galvanostatic cycling voltage profiles of a Li/Li symmetric cell.....	95
Figure 5. Cyclic voltammetry of cells with polypropylene and PCN separator.....	96
Figure 6. Rate performance with PCN and polypropylene separators.....	99
Figure 7. X-Ray Photoelectron spectra of the PCN separator.....	99
Figure S1. Iron oxo cluster (A), linker (B), and crystal structure (C) of PCN-250.....	103
Figure S2. Physical properties of the PCN-250 MOF	105
Figure S3. Thermogravimetric analysis of the selenium encapsulated carbon.....	106
Figure S4. SEM Images of PCN-250 with particle size measurements	106
Figure S5. FTIR spectra of polypropylene (PP), PCN-250 particles.....	107
Figure S6. Cyclic voltammetry of the Li/Se cell.....	109
Figure S7. SEM images of PCN separator.....	110

CHAPTER 1

INTRODUCTION

1.1 Overview

Petroleum is the conventional feedstock for most current fuels, chemicals, and plastics. However, petroleum is finite, and processing petroleum produces a large amount of greenhouse gas (CO_2 and CH_4), contributing to climate change [1]. Therefore, we need to (1) find alternative renewable feedstocks and (2) develop catalytic upgrading processes to transform them into products similar to what we can get from petroleum.

Lignocellulosic biomass and wind/solar are major renewable resources for energies, chemicals, and materials. The use of these renewable resources for the production of fuels and chemicals potentially mitigates climate change and promotes a sustainable society [2-4]. Researchers have processed lignocellulose into fuels and chemicals. Wind and solar are renewable energy sources, which can be stored in the form of electricity in batteries. Using renewable energies from lignocellulose and wind/solar will provide a gateway to a sustainable society. However, tapping into these renewable energies is not an easy task. Lignocellulose has a lot of oxygen atoms, which makes them reactive and corrosive. As a result, we need to activate these oxygen atoms with Lewis acid catalysts to upgrade them into high-value chemicals [5-7]. Common Lewis acid catalysts for conversion of biomass and biomass-derived compounds include transition metal oxide (RuO_2 , MoO_3 , Al_2O_3) [8, 9], porous inorganic materials (modified zeolites, and metal-organic framework) [10-12]. Similarly, although conventional lithium-based batteries, such as lithium-ion and lithium metal batteries, have been used in consumer electronics and electric vehicles, lithium is highly reactive with organic electrolytes, potentially leading to capacity decay and fire/explosions.

A major reason for the lack of safety and capacity retention of lithium-based batteries is the movement of anions in the conventional electrolytes, causing polarization gradient, undesired Li dendrite growth, capacity fade, and thermal runaway. Coincidentally, common anions in electrolytes contain oxygen atoms. As a result, we can apply Lewis acid catalysts to control the anion movement and improve the safety and longevity of lithium-based batteries [13-18]. Therefore, we need to develop Lewis acid catalytic strategies to upgrade lignocellulose and enhance the performance of lithium-based batteries for a sustainable future. My thesis focuses on the development of Lewis acidic materials to (1) convert biomass to chemicals and (2) promote the safety and long-term performance of lithium metal batteries.

1.2 Background

1.2.1 Background of lignin conversion and its relation to Lewis acid sites

Lignin, a major component of plant biomass, is a potential renewable source of phenolics [19]. Lignin consists of three lignol monomers, p-hydroxyphenyl (H), guaiacyl (G), and syringyl (S), derived from p-coumaryl, coniferyl, and sinapyl alcohols [20]. These lignols are linked together by C_β-O-4 bonds (C-O bonds) and C-C bonds (i.e., β-5, and β-β). The lignol's C-O bonds are the most abundant (~ 40-60% of total lignin bonds) [21, 22]. Therefore, to use lignin for chemicals, it is necessary to break the abundant C_β-O-4 linkages to release phenolics. Acid-catalyzed conversion of the lignin to phenolics/aromatics is a promising approach. Mineral acids such as H₂SO₄ [23], H₃PO₄ [24] are well-known acid catalysts for lignin depolymerization. However, they are corrosive and hard to recycle [25]. Heterogeneous solid acid catalysts, such as zeolites (ZSM-5, H-MOR, H-Beta) [26, 27], and metal catalysts, such as Ru/C, Ni/C, Pd/C, Pd/Al₂O₃, CuMgO_x, NiRu, and CuCr₂O₄·CuO, have been studied to break the C_β-O bonds of lignin [28, 29]. However, these solid acid catalysts deactivated quickly due to coke formation [30]. Therefore, we need to develop efficient catalytic systems to maximize the yield of phenolics from lignin.

1.2.2 Background on oxygen vacancies as Lewis acid catalysts

Transition metal oxides (TMOs) are promising catalyst candidates [31, 32]. Reduced metal oxides generate oxygen vacancies, which act as Lewis acid sites to activate oxygen atoms

of the lignin and facilitate selective cleavage of the C-O bonds [33]. However, the effect of oxygen vacancy contents on the C-O cleavage remained unknown. Therefore, understanding the extent of oxygen vacancies of transition metal oxide catalysts to the C-O cleavage will aid in the efficient depolymerization of lignin.

1.2.3 Background on metal-organic frameworks as Lewis acid catalysts

Metal-organic frameworks (MOFs) are porous materials with exceptional chemical and structural tunability. MOFs are synthesized by connecting metal clusters with organic linkers. Due to the high surface area and porous nature, MOFs have been extensively studied for gas adsorption, gas sensor development [34-36], catalysis, and energy storage [37]. The interconnected pores of MOFs enabled the diffusion of ions [38]. MOFs' defects (Lewis acidic sites) can interact with anions through Lewis acid-base interaction and anchor them [39].

Additionally, by size confinement of MOFs' pore, anion can also get trapped inside the pore, thus improving Li-ion mobility [40]. Despite their potential, the use of MOFs for battery applications is still in its infancy. Clearly, further studies are needed to understand the effect of Lewis acidic MOFs on the improved safety and cycling stability of lithium-based batteries.

1.2.4 Background on lithium-metal batteries

The rechargeable lithium metal batteries are key components of consumer electronics and electric vehicles. Lithium metal batteries' safety and long cycle life are desired traits [41, 42]. However, reactive lithium ions and anion gradient in conventional electrolytes cause non-uniform lithium deposition onto the electrode, leading to undesired Li dendrite growth, capacity fade, thermal runaway, and fire/explosion [43]. The ability to control the anion movement in electrolytes can improve safety and capacity retention over prolonged charge/discharge cycles.

CHAPTER 2

CATALYTIC ISOMERIZATION OF THE DIHYDROXYACETONE TO LACTIC ACID BY HEAT TREATED ZEOLITES¹

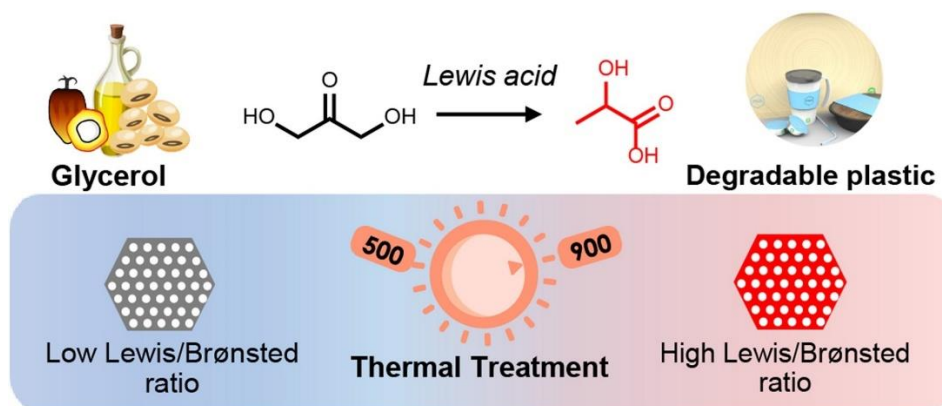


Figure 1. Graphical abstract of catalytic Isomerization of dihydroxyacetone to lactic acid by heat treated zeolites

1. Introduction:

Production of biofuels and bioproducts from lignocellulosic biomass has the potential to mitigate CO₂ emissions and contribute to a sustainable economy [44, 45]. Lactic acid (LA, 2-hydroxypropanoic acid) is an important lignocellulose-derived precursor for the

¹ This chapter is published in *Applied Catalysis A: General* (Hossain et al., 2021, *Appl. Catal. A: Gen.V.611*, 5 February 2021, 117979)

production of food, chemicals, cosmetics, pharmaceuticals, and biodegradable plastics [46]. A rising market for lactic acid is in the production of biodegradable poly (lactic acid) [47-49]. Poly(lactic acid) has many applications, such as in sutures apparel, carpet, and food containers [50]. Moreover, lactic acid can be used for the synthesis of green solvents (lactate esters) [51].

Lactic acid is currently produced by bacterial fermentation of sugars and/or glycerol as feedstocks. The advantage of fermentation is its high selectivity toward lactic acid. Its major drawback is slow kinetics; adequate yield can require up to 3-6 days [52, 53]. The chemical pathway is a faster route to the production of LA using glucose, fructose, and glycerol as feedstocks. Glucose/fructose undergoes retro-aldol to dihydroxyacetone, whereas glycerol undergoes oxidation to dihydroxyacetone. It is generally accepted that dihydroxyacetone undergoes a cascade reaction of (1) dihydroxyacetone dehydration to pyruvaldehyde and (2) subsequent pyruvaldehyde hydration to lactic acid using acid catalysts (**Fig. 2**) [54, 55].

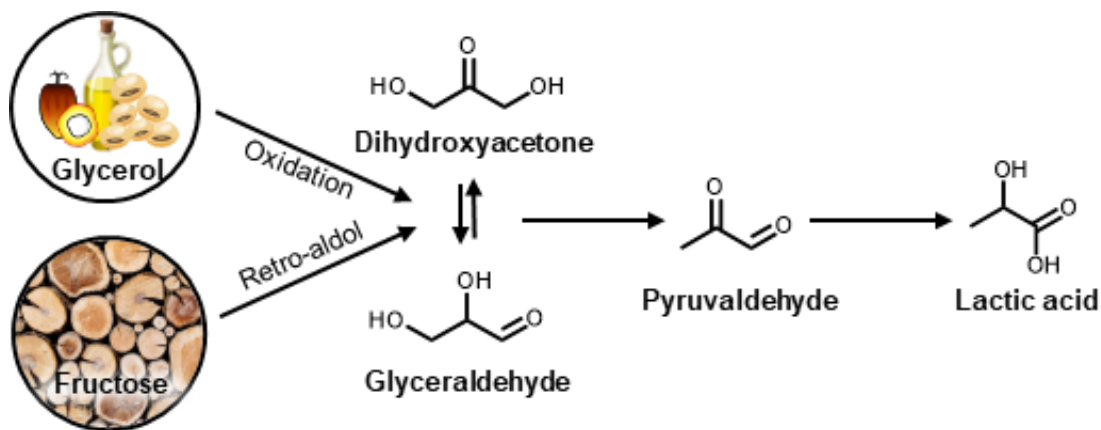


Figure 2. Scheme of chemical pathway for lactic acid production.

Homogeneous catalysts, such as mineral acids (HCl, H₂SO₄, and H₃PO₄) [54, 55] and Lewis acid salts (AlCl₃ and CrCl₃) [55, 56] are active catalysts for dihydroxyacetone isomerization to lactic acid. However, homogeneous catalysts have the classic problem of requiring catalyst separation and product purification. Therefore, it is greatly desirable to develop highly selective solid acid catalysts for dihydroxyacetone isomerization to lactic

acid. Zeolites are commonly used as solid acid catalysts in the chemical and petroleum industries [57-59]. Their heat stability, shape selectivity, and tunable acidity make zeolites versatile in many acid-catalyzed reactions, such as aromatization of alkenes [60-62], esterification [63-68], alkylation [69-71], and isomerization [69, 72-74]. Among all zeolites studied for dihydroxyacetone isomerization to lactic acid, Sn-containing zeolites showed higher selectivity toward lactic acid [75-77]. However, despite their high selectivity, the commercial-scale production of Sn-containing β -zeolites is challenging because of a complicated synthesis procedure; this condition has slowed adoption of Sn-containing β -zeolites in industrial applications [78]. Clearly, industry needs additional simple, yet efficient, heterogeneous catalysts with high lactic acid selectivity.

Investigators have found that heat treatment of zeolites enhanced the activity of their Lewis acids (LAS) and improved paraffin conversion [79], hexane conversion [80], and methane aromatization [81]. The major reason for activity enhancement was the formation of extra-framework aluminum (EFAL) species by dehydroxylation of the Brønsted acid sites (BAS) of the parental zeolites [82]. These aluminum species of EFAL occur in various forms, such as Al^{3+} , $\text{Al}(\text{OH})_2^+$, $\text{Al}(\text{OH})_2^{2+}$, $\text{Al}(\text{OH})_2$, $\text{AlO}(\text{OH})$ and Al_2O_3 , exhibiting the Lewis acid sites (LAS) [82, 83]. Heat treatment to generate LAS within zeolites is commercially accessible. However, there is poor understanding of the function of LAS generated from heat treatment and BAS of zeolites for DHA isomerization to LA in water.

Here we show the tunable LAS density of heat treated ZSM-5 catalysts (15 Si/Al ratio) and their activity in dihydroxyacetone isomerization to lactic acid in water. Heat treatment of ZSM-5 in the range of 700-900°C created EFAL with Al^{3+} Lewis acid sites. The generation of LAS was confirmed by X-ray diffraction, Fourier Transform Infrared Spectroscopy, N_2 adsorption/desorption, and Diffuse Reflectance Infrared Fourier Transform Spectroscopy with adsorbed pyridine. The enhancement in lactic acid selectivity by high-temperature treatment of ZSM-5 implied that the LAS were responsible for the dihydroxyacetone isomerization to lactic acid.

2. Material and Methods:

2.1. Materials. All chemicals were used as received unless otherwise noted. Their CAS numbers, purity, and manufacturers are listed in **Table S1**. ZSM-5 (15 Si/Al ratio) was obtained from Zeolyst[®] International (Conshohocken, PA, USA).

2.2. Catalyst preparation

The modified catalysts were prepared by heating ZSM-5 in air at 500, 700, and 900°C in a tube furnace. In short, the ZSM-5 samples were placed in the ceramic boat. The temperature was raised at a rate of 5°C/min and held isothermally for 10 h [84]. The samples were cooled to ambient temperature and stored in a desiccator. The heat treated ZSM-5 catalysts at 500, 700, and 900°C were referred to as Z-500, Z-700 and Z-900. The Z-900 catalyst was washed with 0.1 M HCl at 65°C for 6 h to remove the extra framework alumina [78]. The acid-washed sample was denoted as Z-900-AW.

2.3. Dihydroxyacetone isomerization to lactic acid and product analysis

Dihydroxyacetone isomerization was performed in 15 mL glass vials in an oil bath. In short, ~60 mg dihydroxyacetone (0.67 mmol) was dissolved in 4 mL deionized water. Approximately 20 mg catalyst was added to the pressure vial, which was sealed and stirred at 140°C for varying reaction times. The reaction product was analyzed with an Agilent High-Pressure Liquid Chromatography (HPLC, Santa Clara, CA, USA) equipped with a diode-array detector (DAD) and refractive index detector (RID). The reactants, intermediates, and products were separated by a Bio-rad[®] Aminex 87H column with 4 mM H₂SO₄ as the mobile phase. The dihydroxyacetone conversion, product yield, and product selectivity were calculated as follows:

$$\text{Dihydroxyacetone conversion (\%)} = \frac{\text{Dihydroxyacetone reacted (mol)}}{\text{Initial dihydroxyacetone (mol)}} \times 100$$

$$\text{Product yield (\%)} = \frac{\text{Product formed (mol)}}{\text{Initial dihydroxyacetone (mol)}} \times 100$$

$$\text{Product selectivity (\%)} = \frac{\text{Product yield (\%)}}{\text{Dihydroxyacetone conversion (\%)}} \times 100$$

2.4.Characterization of catalysts

Infrared spectra of the zeolites were recorded on a JASCO-4700 Fourier transform infrared (FTIR) spectrometer (Easton, MD, USA), equipped with an attenuated total reflection stage (ATR, Pike Technologies, Madison, WI, USA). The surface area and pore volume of zeolites were measured using N₂ adsorption/desorption by a Tristar Micromeritics (Norcross, GA, USA) instrument. Prior to the measurement, the samples were pretreated at 160 °C for 2 h with a Micromeritics FlowPrep and sample degasser. The surface area and pore volume of catalysts were determined by N₂ adsorption/desorption using the Brunauer–Emmett–Teller (BET) [85] and Barrett–Joyner–Halenda (BJH) equations [86]. X-ray diffraction (XRD) analysis of samples was conducted on a Bruker D8 Discover diffractometer (Billerica, MA, USA) using CuK_α radiation and 2θ ranging from 10° to 60° with 0.2 second/step and 0.02 °/step. The Brønsted acid site (BAS) density of the catalysts was quantified by temperature-programmed desorption-thermal gravimetric analysis (TPD-TGA) using n-propylamine as a probe molecule [87]. In short, catalysts were exposed to saturated n-propylamine at 50°C for 12h. The resulting samples were pretreated at 100°C for 1h under N₂ flow (100 cc/min) to remove the physisorbed n-propylamine. Then, the temperature was increased at a rate of 10°C/min to a maximum of 500°C.

To examine the acid properties, Diffuse Reflectance Infrared Fourier Transform Spectroscopy (DRIFTS) with adsorbed pyridine was performed on all catalysts using the JASCO-4700 FTIR spectrometer, equipped with a PIKE DiffuseIR® cell. In short, all samples were first dehydrated at 150°C for 4h to remove physisorbed water. Approximately 5 mg catalysts were positioned in the aluminum sample cup and exposed to saturated pyridine vapors by flowing 50 cc/min N₂ for 30 min. Then, the physisorbed pyridine was removed at 150°C under N₂ for 30 min. The samples were heated under 50 cc/min N₂. The DRIFT spectra were recorded with a resolution of 4 cm⁻¹ from 4000–1000 cm⁻¹ for 256 scans. The DRIFT spectra of adsorbed pyridine showed three distinct bands

between 1600-1400 cm^{-1} . The DRIFT bands at 1545 and 1445 cm^{-1} were assigned to the pyridine coordinated with Brønsted and Lewis acid sites, respectively [84, 88]. The Lewis acid/Brønsted acid (LAS/BAS) ratio was determined from the ratio of intensities (integrals of peak areas) of the DRIFT bands at 1450 and 1545 cm^{-1} [89].

Spent catalysts were analyzed by thermogravimetric analysis (TGA) under N_2 flow (100 cc/min) ramping from 50 to 700°C. TGA and differential TGA profiles were used to determine the weight loss of catalysts. Weight loss up to 250°C was attributed to physisorbed water, and the weight loss between 250-700°C was attributed to the carbonaceous coke on the spent catalysts [90].

3. Results & Discussion

Results

We studied the effect of heat treatment of ZSM-5 zeolites (Si/Al =15) for dihydroxyacetone (DHA) isomerization to lactic acid in a batch reactor. We performed heat pretreatment of ZSM-5 at 500, 700 and 900°C. We refer to the treated zeolites as Z-500, Z-700, and Z-900. We selected ZSM-5 with a Si/Al ratio of 15 because it had moderate acid sites, which made it possible to observe changes in acid sites after heat treatment. Then, we characterized the zeolites for changes in chemical structure and acidity, and we determined how the changes affected dihydroxyacetone isomerization to lactic acid.

Changes in chemical structure and acid properties of ZSM-5 catalysts after heat treatment

To measure the effects of heat treatment on the chemical structure of ZSM-5 catalysts, first, we characterized ZSM-5 by XRD and FTIR. The major XRD peaks of all ZSM-5 catalysts were similar and consistent with reported spectra [84, 91]. Thus, the crystal structure of ZSM-5 was preserved after heat treatment (**Fig. S1**). An increase in treatment temperature from 500 to 900°C caused a right-shift of (051) peak ($2\theta = 23.1^\circ$) (**Fig. 3A**). This shift of (051) peak with increasing temperature indicated a shortening of Si-O-Si bond length and contraction of the unit cells due to the reversible monoclinic to

orthorhombic phase transition [92]. We further characterized these catalysts by FTIR to confirm the shortening of Si-O-Si bond length. One of the characteristic peaks of the ZSM-5 is its 1055 cm^{-1} band, assigned to the internal vibration of Si, AlO_4 tetrahedra (**Fig. 3B**). Following heat treatment, the internal vibration peak shifted toward the higher wavenumber because of an increase in Si-O bonds in relation to Al-O bonds [93]. The up-shift of 1050 cm^{-1} band corroborated our XRD results.

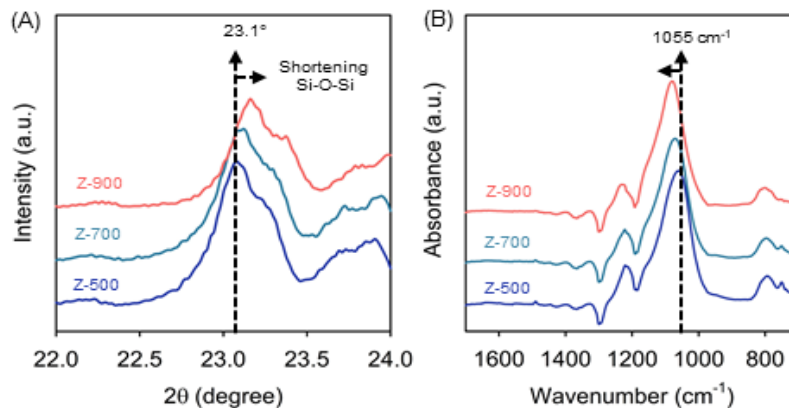


Figure 3. XRD (A) and FTIR (B) spectra of modified ZSM-5 at different treatment temperatures.

Next, we performed N_2 adsorption/desorption on our catalysts to quantify changes in surface area and pore volume after heat treatments. We calculated BET surface area and BJH pore volume from the N_2 adsorption/desorption isotherms (**Fig. S2**). The surface area and pore volume of the heat-treated catalysts increased slightly with increasing temperature (**Table 1**).

To examine changes in acid site type and density due to the heat treatment, we performed TPD-TGA with adsorbed n-propylamine and DRIFTS with adsorbed pyridine on our catalysts. TPD-TGA profiles of heat-treated zeolites showed a progressive decrease in the strong acid site ($>250^\circ\text{C}$). We calculated the BAS density. The Z-500 catalyst had 0.55 mmol amine/g catalyst, in agreement with the reported value [94]. The BAS of the modified catalysts decreased with increasing temperature (**Table 1**). The DRIFT spectra of

adsorbed pyridine enabled determination of LAS/BAS ratio (**Fig. S3B and Table 1**). An increase in temperature increased LAS/BAS ratio.

Table 1. Physical properties and acid densities of catalysts.

Catalyst	BET surface area (m ² /g)	Pore volume (cm ³ /g)	Brønsted acid density (μmol/g)	(BAS) ^a	LAS/BAS ^b	LAS ^c (μmol/g)
Z-500	402	0.20	550		0.08	42
Z-700	464	0.25	410		0.14	56
Z-900	485	0.23	110		0.58	64
Z-900AW	488	0.27	60		0.05	3

^a measured by TGA-TPD with 2-propylamine, ^b measured by DRIFTS with adsorbed pyridine,

^c calculated using BAS and LAS/BAS

We observed a slight increase in LAS. Hoff et al. showed that an increase in temperature of ZSM-5 from 550 to 900°C decreased BAS by 4.0-fold and increased LAS/BAS ratio by 2.5-fold. In theory, zeolites have both BAS and LAS. BAS are derived from the hydrogen atoms of the zeolite framework [95]. Upon heat treatment, the zeolite framework undergoes dehydroxylation, which generates extra framework aluminum (EFAL). The resulting EFAL species are in various forms, such as oxoaluminum cations (AlO⁺, Al(OH)₂⁺, and AlOH²⁺), neutral species (AlOOH and Al(OH)₃), and/or alumina cluster inside the supercage zeolites [96]. As a result, the BAS of the zeolites after heat treatment decreased and the LAS/BAS ratio increased. These results corroborated our findings and suggested that we could increase LAS density by heat treatment. As measured by TPD-TGA, we determined that an increase in treatment temperature caused a slight increase in LAS. In sum, the heat treatment generated the Lewis acid sites in the form of EFAL and decreased the Brønsted acid sites.

Catalytic performance of the heat treated ZSM-5 on the dihydroxyacetone isomerization

To examine the performance of the modified catalysts, we performed dihydroxyacetone isomerization at 140°C. Dihydroxyacetone conversion progressively increased over time and reached >90% by 6h in all cases (**Fig. 4A**). Pyruvaldehyde and lactic acid were major products of this reaction. We observed a small amount of glyceraldehyde in the presence of catalysts, which suggested that dihydroxyacetone isomerization to glyceraldehyde occurred in the presence of these catalysts. As a control, the blank experiment (no added catalyst) showed that dihydroxyacetone conversion increased over time and reached >90% by 6h. We observed a gradual increase in pyruvaldehyde yield with a maximum of 32% by 6h. However, we did not observe lactic acid in the blank. Takagaki et al. [97] also showed that, in the absence of catalysts, dihydroxyacetone was converted to pyruvaldehyde, a finding that corroborates our observations.

Interestingly, with added catalysts, dihydroxyacetone conversion profiles were similar to the blank experiment. This phenomenon suggested that dihydroxyacetone conversion was a thermal reaction. With catalysts, the yield of PA increased and reached the maximum at about 2h, then progressively decreased along with an increase in lactic acid yield. These results suggested that pyruvaldehyde was an intermediate product of dihydroxyacetone isomerization to lactic acid. This volcanic behavior of pyruvaldehyde over time was similar to the reported trend [98, 99]. An increase in treatment temperature enhanced the selectivity of catalysts toward lactic acid. Z-900 had the highest lactic acid yield of 50% after 6h compared with 39% for Z-700 and 21% for Z-500. The increasing trend of lactic acid yield matched a corresponding increase in the LAS density of the catalysts (**Table 1**). By plotting the yields of lactic acid and pyruvaldehyde with respect to LAS density, we observed that PA formation was relatively insensitive to the LAS density (**Fig. 4B**). However, an increase in LAS density enhanced the formation of lactic acid. We hypothesized that dihydroxyacetone dehydration was a thermal reaction. To test this hypothesis, we performed dihydroxyacetone isomerization in water at 90, 120, and 140°C (**Fig. S4**). We observed pyruvaldehyde as the only reaction product. At 90°C, the reaction mixture was clear, and we observed only a slight dihydroxyacetone conversion (<8%) after

6h. At 120°C, the pyruvaldehyde yield progressively increased and reached 29% at 69% dihydroxyacetone conversion (42% pyruvaldehyde selectivity) after 6h. Moreover, the reaction mixture was homogenous and light brown, which suggested formation of pyruvaldehyde (pyruvaldehyde is yellow/brown). Similarly, at 140°C, the pyruvaldehyde yield increased over time and reached 43% at 85% dihydroxyacetone conversion (51% pyruvaldehyde selectivity) at 6h.

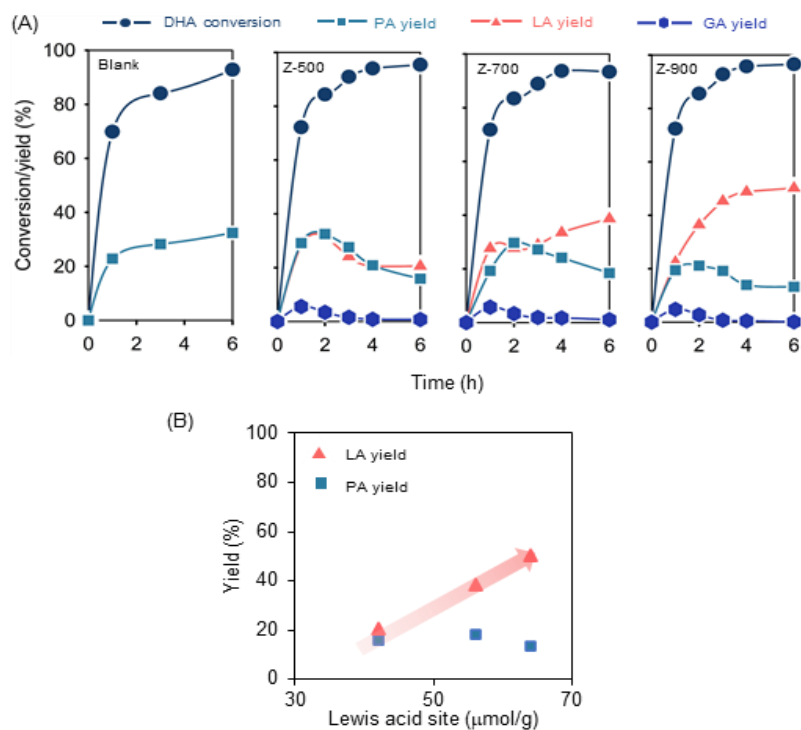


Figure 4. Product evolution of the dihydroxyacetone isomerization by modified ZSM-5 (A). Relationship between yields of lactic acid and pyruvaldehyde at 6 h as a function of LAS density (B). Reaction condition. 60 mg dihydroxyacetone, 20 mg catalyst, 4 g H₂O at 140 °C. DHA = dihydroxyacetone, GA = glyceraldehyde, PA = pyruvaldehyde, and LA = lactic acid.

The reaction mixture became dark-brown, which suggested a higher amount of pyruvaldehyde formed compared with reaction at 120°C. In addition, after 3h, we observed black particles suspended in the reaction mixture, which indicated formation of coke (**Fig. S4 inset**). These results showed that dihydroxyacetone dehydration to pyruvaldehyde

occurred more readily without added catalysts at temperature $>120^{\circ}\text{C}$. However, as the temperature rose to 140°C , degradation of pyruvaldehyde became favorable. Our findings agreed with those of West et al. who observed that pyruvaldehyde degradation was favorable at high temperature ($>115^{\circ}\text{C}$) [100]. These results supported our hypothesis that the dihydroxyacetone dehydration to pyruvaldehyde was driven by the reaction temperature, and LAS was needed to convert pyruvaldehyde to lactic acid. In addition, our results suggested that LAS were active sites for pyruvaldehyde rehydration, in agreement with previous studies [101, 102].

Pyruvaldehyde rehydration by heat treated ZSM-5

To decouple the activities of the catalysts in dihydroxyacetone dehydration and pyruvaldehyde rehydration, we used pyruvaldehyde as a reactant. Our blank experiment showed a progressive increased pyruvaldehyde conversion with no observable lactic acid yield, which suggested that pyruvaldehyde thermally decomposed over time (**Fig. 5**). Z-900 gave the highest lactic acid yield of 50% after 6h. Interestingly, the lactic acid yield profiles of Z-500 (low LAS) and Z-900 (high LAS) with pyruvaldehyde as a reactant were similar to the yield profiles with dihydroxyacetone as a reactant (**Fig. 4**). These results suggested that dihydroxyacetone dehydration to pyruvaldehyde was a thermal reaction, whereas pyruvaldehyde rehydration to lactic acid was acid-catalyzed. Importantly, the LAS density controlled the pyruvaldehyde rehydration activity.

To further confirm the importance of LAS for pyruvaldehyde rehydration, we performed pyruvaldehyde rehydration with the acid-washed Z-900 (Z-900AW). Acid washing removed the EFAL species, sources of LAS, without modifying the porous properties of zeolites [103]. The Z-900AW catalyst showed a weak DRIFT band of adsorbed pyridine (1145 cm^{-1}) (**Fig. S5**), which suggested that most LAS of Z-900AW were removed after acid-wash. The pyruvaldehyde conversion and lactic acid yield profiles of Z-900AW were similar to the profiles of Z-500.

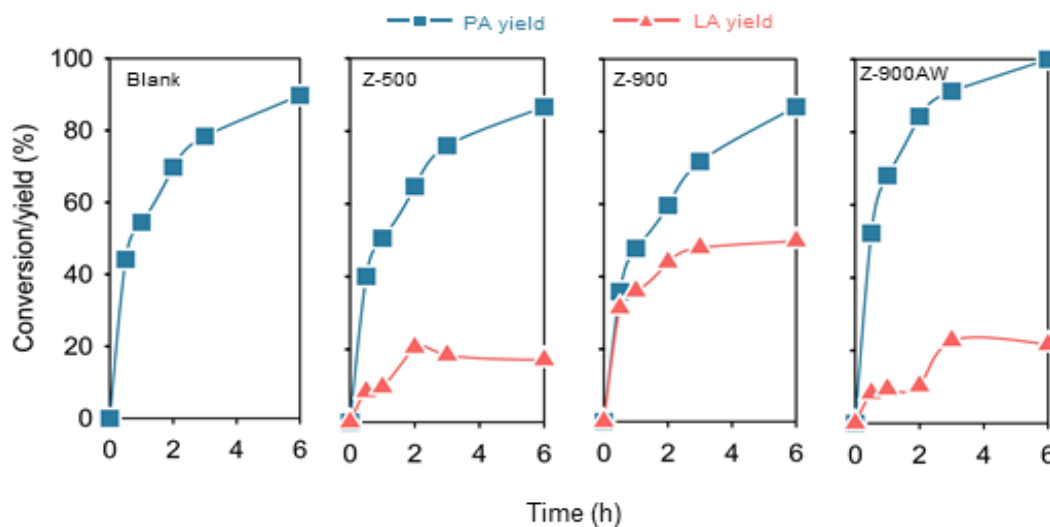


Figure 5. Product evolution of pyruvaldehyde rehydration by modified ZSM-5. Reaction condition. 60 mg pyruvaldehyde, 20 mg catalyst, 4 g H₂O at 140 °C

We further characterized spent catalysts by thermal gravimetric analysis (TGA) and differential thermogravimetry (DTG) to determine their deactivation mechanism related to acid site characteristics. Based on the TGA and DTG profiles, we observed the final weight loss in the order of Z-500 > Z-700 > Z-900. These weight loss values from spent catalysts were attributed to the formation of unwanted carbonaceous deposits, i.e., coke. These results suggested that Z-500 formed the highest amount of coke. This order was consistent with the abundance of BAS (**Fig. 6B**). These results indicated that BAS was responsible for the formation of coke.

To determine the stability of lactic acid, we heated lactic acid at 140°C for 6h without catalyst (blank) and with catalysts, Z-500 and Z-900. Lactic acid conversion was <10% in all cases (**Fig. S6**); thus, lactic acid was thermally stable under this experimental condition. Moreover, these results suggested that the catalysts did not cause side reactions with lactic acid.

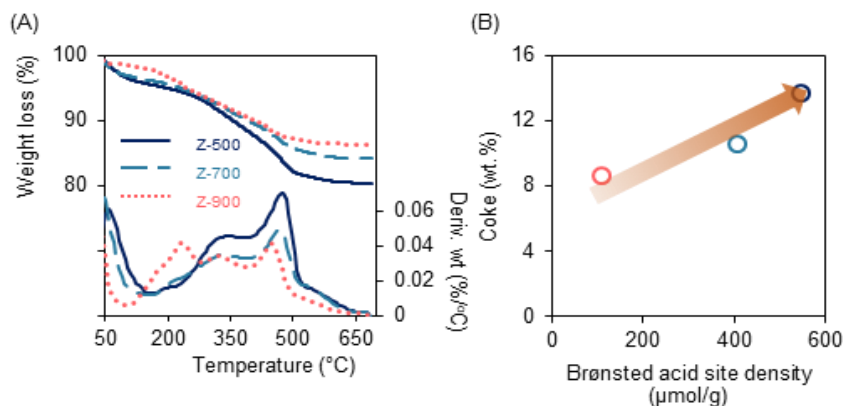


Figure 6. TGA and DTG profiles of the spent catalysts (A) and the relationship between coke formation and Brønsted acid site density (B).

Discussion

We investigated a heat treatment strategy to generate active Lewis acid sites (LAS) within ZSM-5. These LAS were active sites for dihydroxyacetone isomerization in water. The dihydroxyacetone isomerization reaction is a cascade of (1) dihydroxyacetone dehydration to pyruvaldehyde, followed by (2) pyruvaldehyde rehydration to lactic acid. Specifically, our results demonstrated that the dihydroxyacetone dehydration step was driven by reaction temperature, and the LAS were needed for pyruvaldehyde rehydration to lactic acid. Previously, little was known about the activities of the different acid sites in the reaction.

One of our most significant findings was that the high temperature treatment drove the modified ZSM-5 toward a high lactic acid selectivity. The heat treated ZSM-5 had a high LAS density. The dihydroxyacetone dehydration to pyruvaldehyde was a thermal reaction and pyruvaldehyde was formed readily at 140°C, whereas LAS were needed to convert the resulting pyruvaldehyde to lactic acid. Moreover, the amount of LAS was consistent with the order of the catalytic performance, which suggested that the LAS were the active sites for pyruvaldehyde rehydration. Dapsens et al. [78] showed that an increase in LAS density by desilication of MFI zeolites enhanced the lactic acid selectivity of dihydroxyacetone conversion at 140°C for 6h. After acid washing, the LAS density of the

desilicated MFI decreased, resulting in a decrease in the lactic acid. Takagaki et al. [97] used supported chromium and titanium oxide catalysts with varying compositions to generate catalysts with various LAS/BAS ratios for dihydroxyacetone conversion. They found that catalysts with a high LAS were more selective toward LA than those with low LAS. Our results agree with the findings of Dapsens et al. [78] and Takagaki et al. [97]

Another significant finding was that BAS did not have any activity in dihydroxyacetone isomerization. Moreover, the presence of BAS caused unwanted coke formation from pyruvaldehyde decomposition under our experimental condition (140°C). The spent catalyst with high BAS (Z-500) had more coke compared to catalysts treated at 900°C (Z-900). Takagaki et al. [97] showed that the presence of BAS in catalysts lowered the LA selectivity, results that corroborate our findings. Similarly, Nakajima et al. [101] used a Brønsted acid catalyst, H₂SO₄, for dihydroxyacetone isomerization and pyruvaldehyde rehydration. They did not observe any lactic acid yield at 100°C, a further confirmation of our findings. In comparing blank controls of dihydroxyacetone isomerization and pyruvaldehyde rehydration, we found that the blank control of dihydroxyacetone isomerization produced pyruvaldehyde as the only product, whereas the blank control of pyruvaldehyde rehydration did not produce any observable products. These results suggested that dihydroxyacetone dehydration to pyruvaldehyde was a thermal conversion and LAS was needed to convert pyruvaldehyde to lactic acid. Considering together the effects of reaction temperature, LAS, and BAS, we propose the chemical pathway of the modified ZSM-5 for dihydroxyacetone isomerization shown in **Fig. 7**. Dihydroxyacetone dehydration to pyruvaldehyde proceeded with reaction temperature (140°C). The LAS generated within modified ZSM-5 was responsible for the selective dihydroxyacetone isomerization to lactic acid.

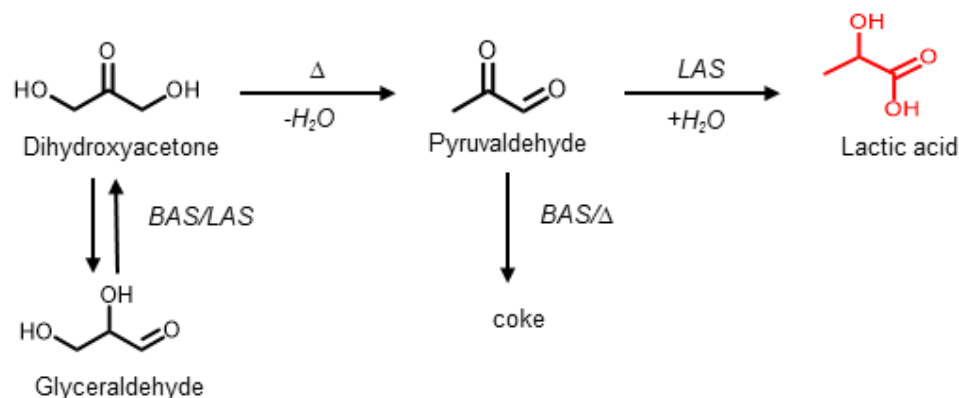


Figure 7. Proposed chemical pathway for the dihydroxyacetone conversion to lactic acid by thermally treated ZSM-5. LAS = Lewis acid sites, BAS = Brønsted acid sites, Δ = heat.

We summarized the performance of selected catalysts for dihydroxyacetone isomerization. West et al. compared the catalytic performance of different zeolites with different Si/Al ratios. They found that all zeolites were active in dihydroxyacetone isomerization, and the LA selectivity was in the following order: H-USY (Si/Al = 6) > H- β (Si/Al = 12.5) > H-MOR (Si/Al = 10) > H-ZSM-5 (Si/Al = 11.5). Moreover, the zeolite with a low Si/Al ratio was more selective to lactic acid, and H-USY (Si/Al = 6) was the most selective to lactic acid (71% lactic acid selectivity) (**Table S2**). Although these zeolites were active for dihydroxyacetone isomerization, their catalytic performance was still inferior to the Sn-based catalysts (Sn-containing β -zeolites [104, 105] and Sn-containing silica [106]) with a high selectivity (>90%) to lactic acid at a full conversion (**Table S3**). Two major limitations of using Sn-based catalysts are (1) a long and complicated synthesis [78], and (2) a scarcity of tin [107].

Clear advantages of this heat treatment approach are (1) the applicability to commercially available ZSM-5, and (2) the ability to control the LAS and BAS densities of ZSM-5 is a superior property compared with the active Sn-containing catalysts for dihydroxyacetone isomerization. Moreover, this strategy can be used for other acid-catalyzed reactions, such as dehydration [108], esterification [109], isomerization [110], etherification [111], and cascade reactions in which both LAS and BAS are needed, such

as hydroxymethylfurfural production from cellulose [112, 113]. The proximity of EFAL and Brønsted acid sites can lead to enhance catalytic activity of alkane cracking [114, 115]. The enhancement of catalytic activity depends on the EFAL properties, such as proximity of EFAL concentration, speciation, location in the framework, distribution, and proximity of Bronsted acid sites [116]. Our work could be extended by identifying the EFAL features using ^{29}Si and ^{27}Al magic angle spinning nuclear magnetic resonance (MAS-NMR) spectroscopy in combination with density functional theory calculations [117, 118] and correlating the results of MAS-NMR and density functional theory with catalytic activity. This information will be important for the development of a cost-effective and sustainable catalytic process for lactic acid production from biomass. In addition, the recyclability and change in mechanical property after catalyst recycling should be assessed to ensure long catalyst lifetime.

Conclusion

We investigated dihydroxyacetone isomerization in water using heat treated ZSM-5. The treatment at elevated temperature increased the Lewis acid sites density and decreased Brønsted acid site density of modified ZSM-5, which promoted high lactic acid selectivity in water. Dihydroxyacetone isomerization to lactic acid is a cascade of dehydration to pyruvaldehyde, followed by pyruvaldehyde rehydration to lactic acid. We demonstrated that dihydroxyacetone dehydration to pyruvaldehyde readily occurred at 140°C and reached 50% lactic acid yield after 6h using heat treated ZSM-5 at 900°C . The high LAS density of heat treated ZSM-5 was responsible for the pyruvaldehyde rehydration. This heat treatment strategy offers a new basis to tune LAS density for biomass processing reactions, including isomerization, dehydration, and esterification.

Supporting Information Chapter 2

Catalytic Isomerization of dihydroxyacetone to lactic acid by heat treated zeolites

Table S1. List of chemicals/reagents used in this study			
Material/Chemical	Supplier	Purity	CAS Number
ZSM-5	Zeolyst® International (Conshohocken, PA, USA)	-	-
Dihydroxyacetone	Oakwood Chemical (Estil, SC, USA)	95 %	96-26-4
Pyruvaldehyde	VWR International (Radnor, PA, USA)	40 %	78-98-8
Lactic acid	VWR International (Radnor, PA, USA)	88 %	79-33-4
Glyceraldehyde	Spectrum Chemical MFG Corp (New Brunswick, NJ, USA)	92.3%	56-82-6
H ₂ SO ₄	VWR International (Radnor, PA, USA)	98 %	7664-93-9
n-propylamine	VWR International (Radnor, PA, USA)	>99%	107-10-8
Pyridine	Chem-Impex International (Wood Dale, IL, USA)	99.97%	110-86-1
N ₂ gas	Welder supplies (Louisville, KY, USA)	industrial grade: 99.999%	-

Table S2. Catalytic performance of selected zeolites for dihydroxyacetone isomerization to lactic acid							
Entry	Catalyst	Si/Al ratio	Condition	Conversion (mol %)	Lactic acid yield (mol %)	Selectivity (mol%)	Ref.
1	Modified ZSM-5	15	140 °C, 6 h, in H ₂ O	96	50	52	This study
2	H-USY	6	125 °C, 24 h, in H ₂ O	99	71	72	[119]
3		30		99	47	47	
4	H-beta	12.5		99	63	64	
6		19		99	37	37	
7	H-ZSM-5	11.5		99	32	32	
8		20		99	22	22	
9	H-MOR	10		99	39	39	

Table S3. Catalytic performance of selected solid catalysts for dihydroxyacetone isomerization to lactic acid						
Entry	Catalyst	Condition	Conversion (mol %)	Lactic acid yield (mol %)	Selectivity (mol%)	Ref.
1	Modified ZSM-5	140 °C, 6 h, in H ₂ O	96	50	52	This study
2	Pb-Sn-containing β -zeolites	190 °C, 2 h, in H ₂ O	99	52	52	[120]
3	Sn-containing Y-zeolites	80 °C, 5 h, in H ₂ O	99	89	90	[104]
	Sn-containing β -zeolites	125 °C, 24 h, in H ₂ O	100	90	90	[121]
4	NbPOa	150 °C, 6 h, in H ₂ O	90	42	47	[122]
5	Silica modified tin(iv) phosphates	140 °C, 5 h, in H ₂ O	100	94	94	[123]
6	Cr-Ti oxides/SiO ₂	130 °C, 5 h, in H ₂ O	100	80	80	[124]
7	H-USY-6 (Si/Al = 6)	125 °C, 24 h, in H ₂ O	99	71	72	[119]
8	H-beta (Si/Al = 12.5)		99	63	64	
9	H-USY-30 (Si/Al = 30)		99	47	47	

aContinuous process

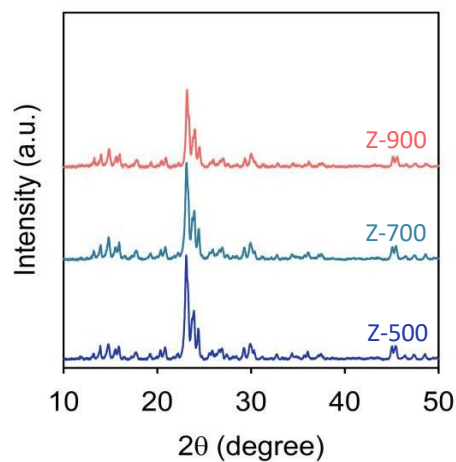


Figure S1. XRD spectra of the modified ZSM-5 at different treatment temperatures.

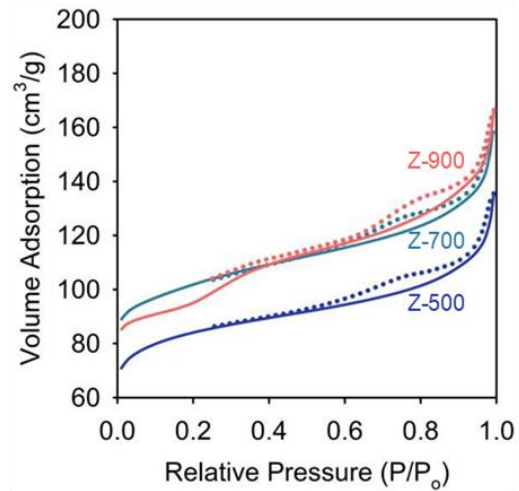


Figure S2. N₂ adsorption/desorption isotherm of the modified XSM-5 catalyst.

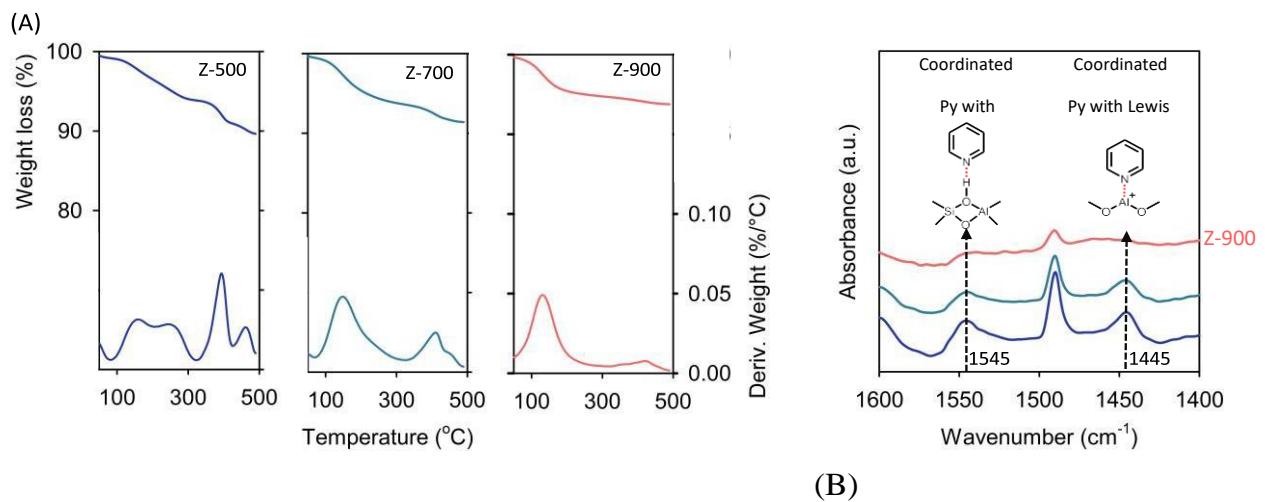


Figure S3. TGA Profile of the ZSM-5 with adsorbed n-propylamine (A) and FTIR spectra of the adsorbed pyridine (Py) on modified ZSM-5 (B)

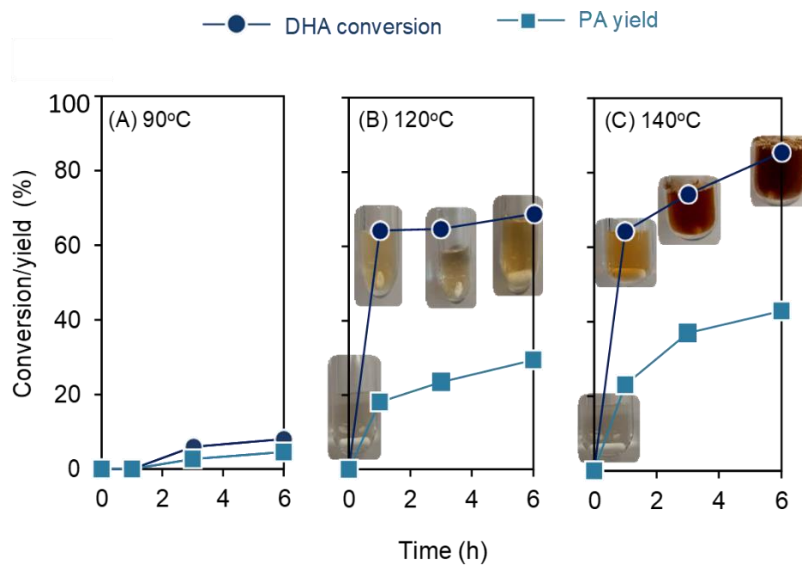


Figure S4. Product evolution of dihydroxyacetone isomerization without added catalysts at 90, 120, and 140 °C. Reaction condition. 60 mg dihydroxyacetone, 4 g H₂O. DHA = dihydroxyacetone, PA = pyruvaldehyde

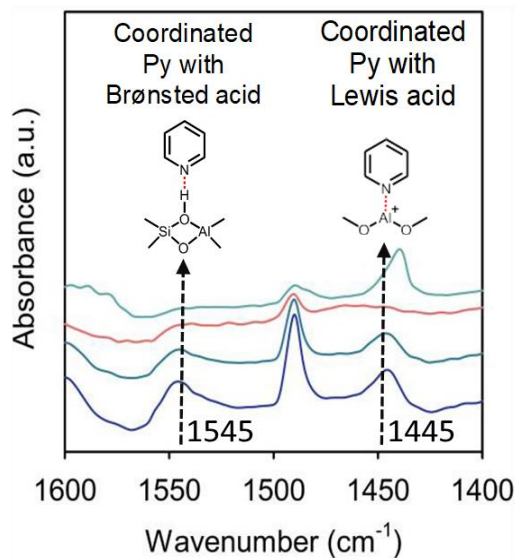


Figure S5. DRIFT spectra of adsorbed pyridine (Py) on modified ZSM-5 with and without acid wash

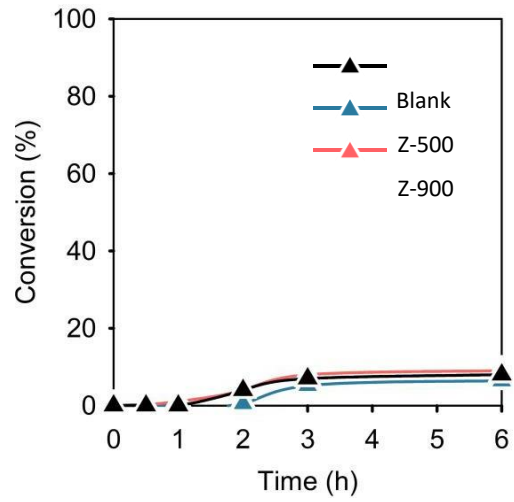


Figure S6. Thermal stability of lactic acid by modified ZSM-5. Reaction condition. 60 mg Lactic acid, 20 mg catalyst, 4 g H₂O at 140 °C.

CHAPTER 3

CATALYTIC CLEAVAGE OF THE β -O-4 ARYL ETHER BOND OF LIGNIN MODEL COMPOUNDS BY Ru/C CATALYST ²

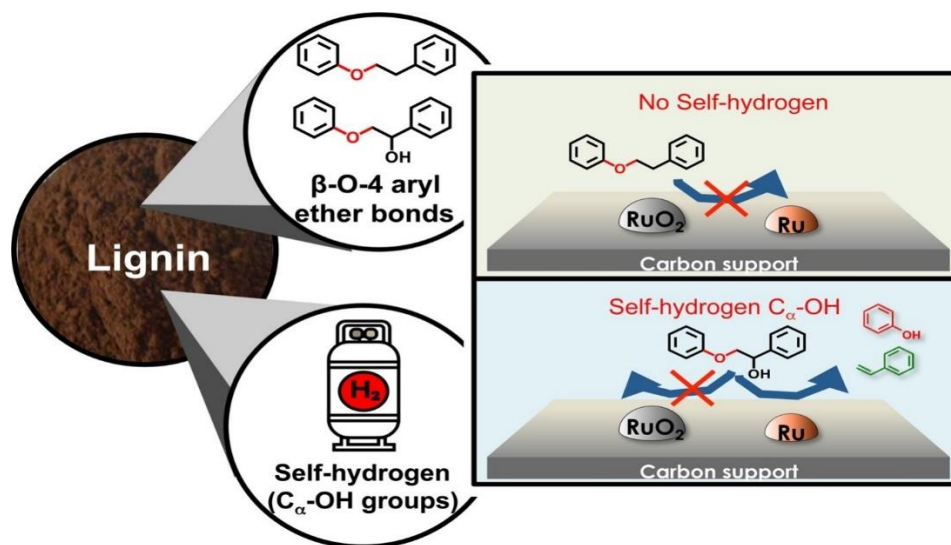


Figure 1. Graphical abstract of catalytic cleavage of the β -O-4 aryl ether bonds of lignin model compounds by Ru/C catalyst

Introduction.

Aliphatic and aromatic hydroxyl groups [125]. These linkages and functional groups make lignin a stiff and rigid structure, giving plants strength and protecting them from external disturbances such as insects, disease, and weather. This rigid structure of lignin is another reason why it is difficult to break lignin into aromatic monomers.

² This chapter is published in *Applied Catalysis A: General* (Hossain et al., 2019, *Appl. Catal. A: Gen.*, V.

582, 25 July 2019, 117100

To release renewable aromatic monomers, investigators have used hydrogenolysis by metal catalysts, such as Ru/C, Ni/C, Pd/C, Pd/Al₂O₃, CuMgO_x, NiRu, and CuCr₂O₄·CuO, to break the abundant C_β-O bonds of lignin [126-137]. Typically, a high H₂ pressure (≥ 10 bar) is required for hydrogenolysis [133, 138, 139]; however, the high H₂ pressure causes undesired side reactions of over-hydrogenating the aromatic rings, cracking, and coke formation [138]. Moreover, the hydrogen sources are not naturally available and renewable, making H₂-mediated hydrogenolysis uneconomic on a large scale [140, 141]. To minimize the effect of side reactions, the industry requires hydrogen-lean or hydrogen-free catalytic systems.

Oxophilic metals, such as ruthenium (Ru), have partially filled d-bands. The oxophilicity of Ru enables strong interaction with oxygen atoms in the adsorbates, resulting in the direct cleavage of C-O bonds [142-144]. Previous studies have shown that reducible RuO₂ catalysts have Lewis acid sites that facilitate the hydrodeoxygenation of furanics in the liquid phase [145, 146]. Supported Ru catalysts have been applied to the hydrogenolysis of lignin and its model compounds [147, 148], the effect of Ru and RuO₂ on the hydrogenolysis and hydrodeoxygenation of lignin is not well understood. The partial oxidation of Ru to RuRuO₂ creates a bifunctional catalyst containing: (1) Ru metal sites, catalyzing hydrogenolysis/hydrogenation; and (2) RuO₂ Lewis acid sites, facilitating hydrogenolysis [145]. We hypothesized that the aliphatic -OH groups (C_α-OH) of lignin could serve as internal hydrogen donors; the released hydrogen would break lignin's C_β-O bonds without further aromatic ring saturation. We further expected that this hydrogenolysis reaction would occur with a Ru/C catalyst having an optimal Ru/RuO₂ composition.

To test these conjectures, we synthesized Ru/C catalysts with various ratios of Ru/RuO₂ and assessed their activities in hydrogenolysis of the C_β-O bond in two lignin model compounds: 2-phenoxy-1-phenylethanol and 2-phenyl ethyl phenyl ether. The aliphatic C_α-OH group of 2-phenoxy-1-phenylethanol enabled the hydrogenolysis of the C_β-O bonds in the absence of H₂. An increase in Ru content enhanced hydrogenolysis activity. The elimination of the H₂ requirement in lignin hydrogenolysis provides a simple yet efficient approach for lignin conversion to aromatic chemicals.

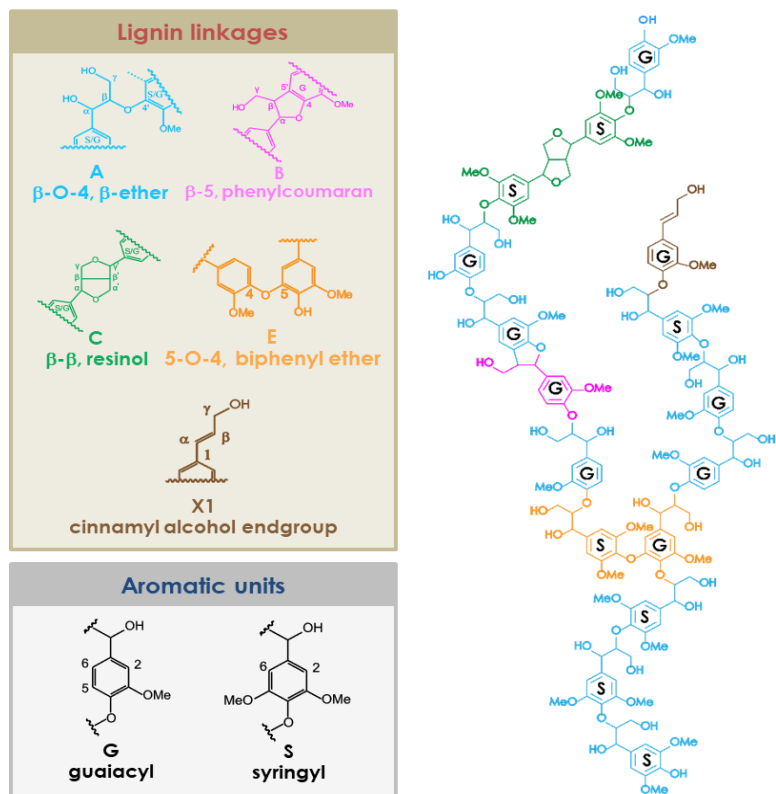


Figure 2. An example of truncated (poplar) lignin structure. This lignin model depicts β -O-4 aryl ether bonds as the abundant linkages.

2. Experimental

2.1. Materials

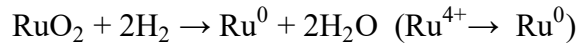
All reagents were used as received. Their manufacturers, purity, and CAS numbers are shown in Table S1.

2.2. Catalysts pretreatment and characterization

To tailor the catalyst composition, the commercial Ru/C catalyst (parental Ru/C) was treated in various conditions before catalytic testing. For reduction, the fresh Ru/C catalyst was reduced in H₂ flow of 40 cc/min at 250°C for 3h, followed by the 12h passivation in air, to form the Ru/C-Red catalyst. For oxidation, the fresh Ru/C catalyst

was oxidized in pure O₂ flow of 40 cc/min at 200°C for 3h to create the Ru/C-Ox catalyst. The commercial Ru/C and commercial pre-reduced Ru/C catalysts were also used as references. Descriptions of these Ru/C catalysts and their pretreatment conditions are summarized in **Table S2**.

X-ray diffraction (XRD) was performed with a Bruker D8 Discover diffractometer (Billerica, MA, USA) using CuK_α radiation in the 2θ range from 20° to 60° with 1 second/step (0.02 increment). H₂ Temperature-Programmed Reduction (H₂-TPR) experiments were performed with a Micromeritics ChemiSorb 2720 equipped with a thermal conductivity detector (TCD) (Norcross, GA, USA). About 20-40 mg of sample was pretreated at 250°C for 1h under He flow to remove adsorbed water. Then, the sample was cooled to room temperature under He flow. TPR profiles were recorded by heating the samples from room temperature to 800°C at a heating rate of 10°C/min in the 10.01% H₂/Ar at a flow rate of 40 cc/min. The RuO₂ content in the Ru/C catalysts was calculated by the following reaction:



H₂ consumption and mole of metallic Ru and RuO₂ were calculated using the known H₂ (vol.%) as a calibrant as follows:

$$\text{H}_2 \text{ consumption (mol H}_2\text{/g total Ru)} = \frac{\sum \text{Area}_{\text{outlet peaks}}}{\text{Area}_{\text{calibrant}}} \times \frac{\text{mole}_{\text{calibrant}}(\text{mol})}{\text{mass}_{\text{catalyst}}(\text{g})} \times$$

$$\frac{1}{\text{Ru loading (wt.\%)}}$$

$$\text{mole}_{\text{RuO}_2}(\text{mol}) = \text{mole}_{\text{O}_2} = \frac{1}{2} \text{mole}_{\text{H}_2 \text{ consumption}}$$

$$\text{mole}_{\text{metallic Ru}}(\text{mol}) = \text{mole}_{\text{total Ru}} - \text{mole}_{\text{RuO}_2}$$

$$\text{RuO}_2 \text{ in total Ru (mol.\%)} = \frac{\text{mole}_{\text{RuO}_2}}{\text{mole}_{\text{Ru}} + \text{mole}_{\text{RuO}_2}} \times 100$$

Energy Dispersive X-ray Spectroscopy (EDS) was conducted on the spent Ru/C catalyst to assess the change in the Ru content after the reaction. EDS was performed on the Thermo Scientific™ FEI Nova600 FEG Scanning Electron Microscope (SEM) equipped with EDS (Hillsboro, OR, USA).

2.3. Hydrogenolysis of lignin model compounds

All reactions were performed in a 25 mL autoclave reactor (Parr Instrument, Moline, IL, USA). The reactant concentrations were 1 wt.% of 2-phenoxy-1-phenylethanol or 2-phenyl ethyl phenyl ether in ethanol. The catalyst loading was 20 wt.% (~18.9 mg catalyst) with respect to the reactant (94.68 mg reactant in 12 mL ethanol solution). Prior to the reaction, the reactor was purged three times with N₂ to remove O₂. The reactor was then pressurized to 8 bar under N₂ at room temperature (for consistency). The hydrogenolysis reaction was performed at 280°C for 4h with a stirring rate of 500 rpm. The reaction was stopped by quenching in a cold water bath. The reaction sample was centrifuged to remove any residual solids, then diluted with ethanol prior to the product analysis. Dodecane was used as an internal standard.

The reactants and products were identified and quantified by the Agilent 7890B GC (Agilent Technologies, Santa Clara, CA, USA) equipped with Mass spectrometry (MS) and Flame Ionization Detectors (FID). An HP-5MS column (30mx0.25mmx0.25µm, Agilent Technologies, Santa Clara, CA, USA) was used for product separation with the following temperature program: injection temperature 275°C and FID detector temperature 300°C; split ratio 1:50. The temperature program started at 45°C and increased at 10°C/min to 250°C, then held for 20 min. Reactant conversion, product selectivity, and specific activity were calculated using the pre-determined response factors with dodecane as an internal standard. The calculations are as follows:

$$\text{Conversion (\%)} = \frac{\text{mole of reactant reacted}}{\text{initial mole of reactant}} \times 100\%$$

$$\text{Selectivity (\%)} = \frac{\text{mole of product generated}}{\text{mole of feed reacted}} \times 100\%$$

$$\text{Specific activity (mmol/(g}_{\text{Ru}} \cdot \text{h}))} = \frac{\text{mole of feed reacted}}{\text{weight of Ru} \times \text{time}}$$

2.4. Catalyst stability evaluation

The catalyst stability was examined by conducting catalyst recycling experiments for four times. After the reaction, the spent catalyst was recovered by filtration and reused without washing/drying in the next experiment. The reactants and products from each recycle run were quantified by GC-MS/FID. The Ru content of the spent catalyst from each recycle run was analyzed by H₂-TPR. In separate experiments, the spent catalyst was sampled with the reaction products after each recycle run into the U-shaped reactors directly for H₂-TPR to minimize the catalyst oxidation in air.

3. Results and Discussion

To examine the effect of metallic Ru and RuO₂ on the hydrogenolysis of the C_β-O bonds, we varied the amount of Ru and RuO₂ by treating the parental Ru/C in various conditions (**Table S2**). The commercial pre-reduced Ru/C served as the control. We used H₂-TPR and XRD to determine the amount of RuO₂ in these four catalysts and identify their phases, respectively. We correlated changes in Ru content with the hydrogenolysis activities of the catalysts toward the C_β-O bonds of the lignin model compounds.

3.1. Catalysts pretreatment and their reducibility

The relative Ru and RuO₂ content in Ru/C catalyst play an important role in hydrogenolysis of the C_β-O bonds. We first used the H₂-TPR technique to determine the amount of Ru and RuO₂ in the four catalysts. Using H₂ as a stoichiometric reductant, we found that, as the catalyst temperature increased from 50 to 350°C, the reduction profiles of Ru/C catalysts showed two major reduction peaks. The first reduction peak appeared at <100°C and the second reduction peak occurred at >100°C (**Figure 3**). The presence of

two reduction peaks suggested that ruthenium took different oxidation states while reducing from Ru^{4+} (RuO_2) to Ru^0 (metallic Ru). The H_2 -TPR profile of the pre-reduced-Ru/C showed a small reduction peak at 74°C . This reduction peak was observed previously in Ru/ CeO_2 and Ru/C catalysts [149]. The commercial Ru/C catalyst (parent) had two observable reduction peaks at $<100^\circ\text{C}$ and $>200^\circ\text{C}$ with a shoulder peak at 246°C . The first reduction peak at low temperature appeared to be broad doublets. Other investigators have observed doublets with Ru supported on Al_2O_3 , ZrO_2 , CeO_2 , and carbon [143, 149, 150]. Doublets are hypothesized to form because of (1) the strong interaction between Ru species and the support [149, 151], and (2) the reduction of Ru^{4+} to Ru^{2+} , suggesting the formation of easily reducible surface species. The second reduction peak ($>200^\circ\text{C}$) could be assigned to the reduction of Ru^{2+} to Ru^+ or the reduction of Ru^{2+} to Ru^0 (metallic Ru) [152-157]. After reducing the parental Ru/C in H_2 , the second reduction peak at 205°C and the shoulder peak at 246°C disappeared (**Figure S1**) and the H_2 -TPR profile became similar to that of pre-reduced Ru/C. This result suggested that this H_2 -TPR condition was sufficient to completely reduce the Ru^{4+} to Ru^0 . Then, we allowed this catalyst to passivate in the air for 12 h to generate partial RuO_2 phase. We used the term Ru/C-Red to represent this sample. The Ru/C-Red had a similar H_2 -TPR profile to that of Ru/C. However, its first reduction peak was rather broad and the second reduction peak was shifted to a higher temperature (217°C) compared with that of the parental Ru/C (205°C). Next, we oxidized the parental Ru/C using O_2 flow at 200°C for 3h to obtain the Ru/C-Ox sample. We observed a shift of the second reduction peak from 205°C to 135°C , indicating that there were structural changes in RuO_2 from oxidation. The large reduction peak at 135°C on the Ru/C-Ox resulted from the formation of larger RuO_2 particle sizes, decreasing the interaction between supports and RuO_2 [158-162]. We also used these H_2 -TPR profiles to determine the Ru and RuO_2 content in all catalysts.

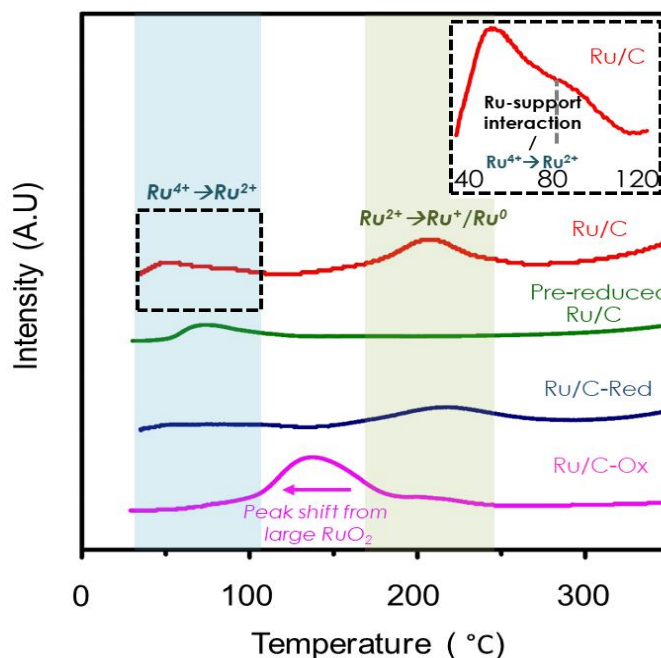


Figure 3. H₂-TPR profiles of Ru/C catalyst from different pretreatment conditions.

The Ru content in the Ru/C catalysts, calculated based on the H₂ consumption, was in the following order: pre-reduced Ru/C (95.3%) > Ru/C-Red (85.5%) > Ru/C (82.0%) > Ru/C-Ox (74.7%) (**Table S3**). The parental Ru/C catalyst had ~82% Ru (metallic) and ~18% RuO₂. Ru/C-Red, reduced Ru/C catalyst by H₂ and passivated in the air to generate RuO₂, had a 22% decrease in RuO₂ content. After oxidizing the parental Ru/C, the RuO₂ content of the Ru/C-Ox increased ~28% compared to that of parental Ru/C. For Ru/C-Ox, the carbon support was oxidized during the pretreatment, causing a relative increase in Ru content per total gram of Ru/C-Ox. We used thermogravimetric analysis of the Ru/C catalysts, phase identification by XRD spectra, and an estimated amount of RuO₂ and Ru content by H₂-TPR to determine the mass percentage of Ru, RuO₂, and C (**Table S4**). These results indicated that after oxidation, the Ru/C-Ox lost carbon support by ~22 wt.%. These Ru/C catalysts were used in the hydrogenolysis of the lignin model compounds.

H₂-TPR results confirmed the reducibility of the Ru/C catalysts. They demonstrated that we could tune the oxidation state of Ru/C under various pretreatment conditions [147]. Our results also illustrated that ruthenium was easily passivated, as shown in the formation of RuO₂ under the ambient condition. The use of commercial Ru/C catalyst needs to be with cautions because it can be passivated, affecting the Ru and RuO₂ contents. The catalyst pretreatment conditions affected the grain size and dispersion/agglomeration of Ru catalysts on supports. For example, the shift of the reduction peak to the lower reduction temperature of the Ru/C-Ox (compared to that of parental Ru/C) suggested an increase in the grain size of the RuO₂. The change in grain size of catalyst also affects its catalytic activity [163]. To identify changes in Ru and RuO₂ phases and grain size of catalysts, we applied the XRD technique on all catalysts.

3.2. Identification of Ru and RuO₂ phases and determination of catalyst grain sizes

XRD spectra of Ru/C catalysts revealed the Ru and RuO₂ phases and their degrees of dispersion on the carbon support (**Figure 4**). The parental Ru/C and pre-reduced Ru/C catalysts had broad XRD spectra, suggesting that (1) the metallic Ru and RuO₂ were highly dispersed on the carbon, and (2) their grain sizes were small [137]. After the reduction in H₂ and passivation, the Ru/C-Red illustrated three XRD peaks, associated with the presence of metallic Ru at 2 θ of ~39° for Ru(100), 42° for Ru(002), and 44° for Ru(101) [157, 164]. The crystallite sizes of the Ru catalysts were calculated from the Debye-Scherrer equation and the broadening of the main peaks [165]. The mean crystallite size was ~4.4 nm for Ru(100) and Ru(101). The peak Ru(002) had low intensity, and we did not calculate its crystallite size. In the case of Ru/C-Ox, we observed sharp XRD peaks associated with the presence of Ru and RuO₂. The three XRD diffraction peaks of Ru (100), (002), and (101) became more pronounced compared with the diffraction peaks from the Ru/C post-reduction. This increase in peak intensity resulted from (1) the lower content of the carbon support due to the oxidation of carbon and (2) the sintering of the Ru, which formed larger Ru aggregates. Our calculation showed that the crystallite size of the Ru was ~19-25 nm. Three XRD peaks of RuO₂ emerged, corresponding to RuO₂(110), RuO₂(101), and RuO₂(211) at 2 θ of 28, 35, and 54° respectively [155-157]. We attributed the emergence of these RuO₂ peaks to (1) the oxidation of the metallic Ru, forming RuO₂

and/or (2) the sintering of the RuO₂ particles into larger RuO₂ particles. The crystallite sizes of RuO₂ were determined to be ~6-10 nm. The formation of the larger RuO₂ particles observed by XRD corroborated the shift of the reduction temperature to lower temperature in the H₂-TPR profile.

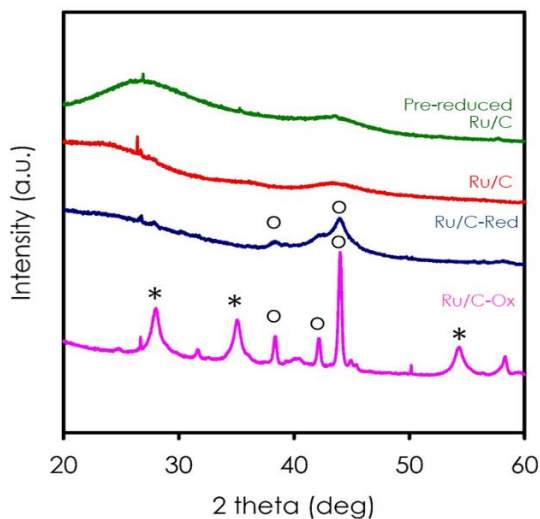


Figure 4. XRD patterns of investigated catalysts. Note: metallic Ru (○) and RuO₂ (*).

3.3. Catalytic activity of parental Ru/C catalyst in hydrogenolysis of the β -O-4 aryl ether bond

We tuned the Ru/C catalyst's oxidation states under various oxidation and reduction conditions, generating four catalysts, Ru/C, pre-reduced Ru/C, Ru/C-Red and Ru/C-Ox. Then we characterized these catalysts by H₂-TPR to determine the Ru content and probed for their hydrogenolysis activity on lignin model compounds. To assess the activity of the C _{α} -hydroxyl (C _{α} -OH) group on the hydrogenolysis of the C _{β} -O bond, we first tested the parental Ru/C on 2-phenethyl phenyl ether (1a) and 2-phenoxy-1-phenylethanol (1b) under N₂. The parental Ru/C was not active for hydrogenolysis of 2-phenethyl phenyl ether (1a), whereas it promoted 52.5% conversion on 2-phenoxy-1-phenylethanol (1b) (**Table 1**). Ethylbenzene (2) and phenol (4) were major reaction products, confirming the occurrence of the hydrogenolysis reaction. Typically, hydrogenolysis of the C _{β} -O bond requires high H₂ pressure and metal catalysts, including NiMo sulfide, Ni, and Pd [31, 133, 138, 139].

However, our results showed that the -OH group at the C α position (C α -OH) enabled cleavage of the C β -O bond by Ru/C at 280°C in the absence of H $_2$.

Table 1. Conversion and product selectivity from hydrogenolysis of 2-phenethyl phenyl ether (1a) and 2-phenoxy-1-phenylethanol (1b) over Ru/C catalyst.

Entry	Feed	Conversion (%)	Selectivity (%)					1a
			2	3	4	5	6	
1	1a	-	-	-	-	-	-	-
2	1b	52.5	25.4	6.8	34.6	8.2	3.7	20.1
3	1b*	52.7	13.2	7.4	33.6	21.9	-	13.6

Reaction condition: 280°C, 4 h, 8 bar N $_2$, 1 wt.% reactant/ethanol, 20 wt.% catalyst loading. * 1,4-dioxane was used as a solvent.

Zhang et al. observed similar products for hydrogenolysis of 2-phenoxy-1-phenylethanol on NiMo sulfide catalysts, but H $_2$ and alcohol were needed [139]. Based on our identified reaction products (**Table 1**), we proposed a reaction pathway (**Figure 5**) wherein Ru/C catalyzed the hydrogenolysis of C β -O bond of 2-phenoxy-1-phenylethanol (1b) by activation of C α -OH. The activation of C α -OH resulted in hydrogen transfer and the hydrogenolysis of C β -O bond and yielded phenol (4) and phenylethanone (5). If the Ru/C catalyst only catalyzed hydrogenolysis of the C β -O bond of 2-phenoxy-1-phenylethanol (1b), we could only observe phenol (4) and phenylethanone (5). In our case, the presence of 2-phenethyl phenyl ether (1a), ethylbenzene (2), styrene (3), and *p*-ethylacetophenone (6) indicated that Ru also catalyzed side reactions. The presence of styrene (3) and ethylbenzene (2) suggested that 1-phenylethanone (5) underwent hydrodeoxygenation to form styrene as an intermediate. The styrene was then hydrogenated to ethylbenzene.

The formation of *p*-ethylacetophenone (6) occurred by the alkylation of phenylethanone (5) and ethanol. We did not observe this product when the reaction was run in dioxane.

Moreover, in dioxane as a solvent, the selectivity toward p-ethylacetophenone (6) was low (<4%). Ru/C also catalytically cleaved C α -OH of 2-phenoxy-1-phenylethanol, forming 2-phenethyl phenyl ether (1a) by the undesired deoxygenation pathway [166]. Cao et al. used PdCl₂, Pd/C, and Ru/C under 70 bar CO₂ and found a high yield of 2-phenethyl phenyl ether (1a) [167]. In that study, the formation of 2-phenethyl phenyl ether (1a) resulted from the formation of the better leaving group, -OH₂⁺, derived from the hydroxyl group at the C α -OH position with the second hydrogen derived from ethanol [167].

Although our result suggested that Ru/C activated the C α -OH to release its hydrogen for hydrogenolysis of the C β -O bond in an ethanol solvent, we could not rule out the possibility that hydrogen was derived from ethanol. Ethanol is a polar protic solvent, known to donate hydrogen under the reaction condition we employed. Thus, to decouple the contribution of hydrogen from C α -OH and ethanol, we ran a similar experiment using a non-hydrogen donor solvent, the aprotic polar solvent 1,4-dioxane. Interestingly, we obtained 52.7% conversion of 2-phenoxy-1-phenylethanol (1b), similar to the yield in the ethanol solvent (Entry 3, Table 1).

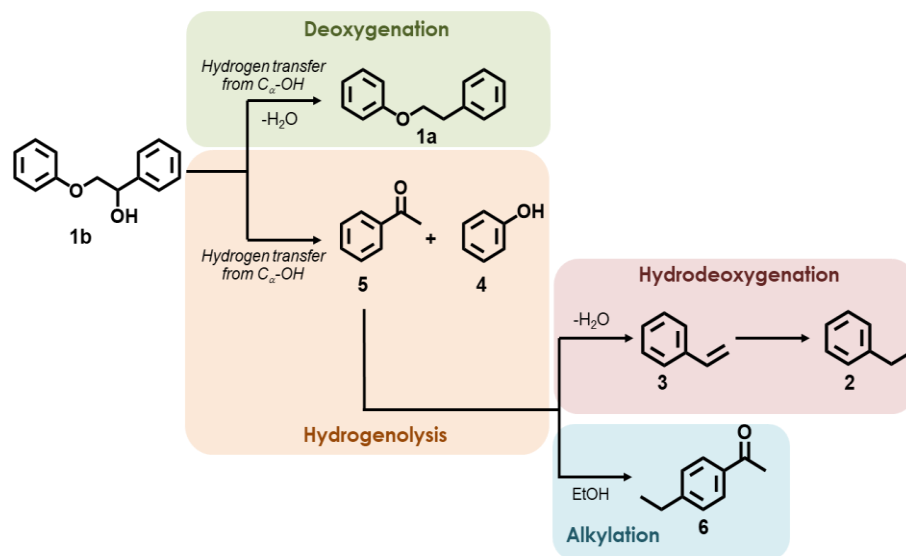


Figure 5. The proposed reaction pathway of hydrogenolysis of 2-phenoxy-1-phenylethanol over Ru/C catalyst with C α -OH as the hydrogen source.

However, using dioxane as a solvent, we found a lower selectivity toward aromatic hydrocarbon products ($\Sigma(2,3) = 20.6\%$) compared with selectivity in ethanol (32.2%). A previous study on hydrogenolysis of 2-phenethyl phenyl ether (1a) on Pd/C showed a 30% yield of ethylbenzene (2) in isopropanol, but ethylbenzene is not observed in dioxane and toluene [167]. These results demonstrated that Ru activated C_{α} -OH, releasing hydrogen to form “hydrogen pool” for hydrogenation to cleave C_{β} -O bond [167]. Moreover, ethanol promoted the hydrodeoxygenation reaction as shown by a higher selectivity toward aromatic hydrocarbon products compared with selectivity in dioxane. In addition, ethanol can be obtained from renewable resources. For these reasons, we used ethanol in the remaining studies. Next, we wanted to compare the effect of Ru content in the Ru/C catalyst in hydrogenolysis of C_{β} -O bond. We tuned the Ru content by applying various pretreatment conditions.

3.4. Catalytic activity of Ru and RuO₂ catalysts in hydrogenolysis of the β -O-4 aryl ether bond

To assess the effects of Ru and RuO₂ in hydrogenolysis of the C_{β} -O bond, we evaluated Ru/C catalysts under various pretreatment conditions to obtain various Ru content (Table S5). For each Ru/C catalyst, we calculated the catalytic activity for reactant conversion per (total) gram of Ru per unit time. The reaction using the pre-reduced Ru/C had the highest hydrogenolysis activity of 112 mmol reactant/g_{Ru}*h, whereas the Ru/C-Ox had the lowest hydrogenolysis activity of 4 mmol reactant/g_{Ru}*h. One reason for this difference is that the Ru/C-Ox had the highest RuO₂ content (25%) and large crystallite sizes of Ru and RuO₂ (~19-25 nm for Ru and ~6-10 nm for RuO₂) from aggregation and/or sintering of the small Ru and RuO₂ particles. The large Ru crystallite size lowered the surface of the active sites, resulting in lower catalytic activity [163]. Moreover, RuO₂ has a weak oxygen surface bonding to bridge oxygen atoms on the RuO₂ surface [168]. Conversely, metallic Ru has a

strong adsorption interaction with oxygen and –OH group [169-171], which promotes the hydrodeoxygenation of 2-phenethyl phenyl ether (1a) and ethylbenzene (2). The increasing trend of the catalytic activity with increasing metallic Ru suggested that the metallic Ru was the active phase for the hydrogenolysis of C β -O bonds. Moreover, metallic Ru was the active site that activated C α -OH, releasing this “self-hydrogen” from 2-phenoxy-1 phenylethanol (1b). The surface of RuO $_2$ on the Ru/C catalyst exists upon oxidation of Ru when exposed to air during storage/handling. Our H $_2$ -TPR results also showed that Ru was passivated under the ambient condition, changing the Ru and RuO $_2$ contents and affecting catalytic activity. The use of alcohol as a solvent is beneficial because alcohol can reduce the RuO $_2$ in-situ, maintaining the catalyst in the active form and enhancing the catalytic activity over time [172]. We hypothesized that, during the reaction, RuO $_2$ would be reduced in-situ when ethanol was the solvent [173, 174], enhancing the catalytic activity. To test this hypothesis, we performed the hydrogenolysis of the 2-phenethyl phenyl ethanol (1b) in ethanol over 12h. We determined the Ru content of the spent catalyst by sampling the spent catalyst with the reaction products after each reaction into the U-shaped reactors directly for H $_2$ -TPR. By doing so, we minimized the catalyst oxidation in air. We observed an increase in reactant conversion over time and reached 99.7% after 12h (Table S6). Moreover, the Ru content of the spent catalyst increased as a function of time and reached 3.5 % at 12h (Figure S2). The selectivity toward aromatic product yields ($\Sigma(2,3)$) remained ~31-35% regardless of reaction time. This increase in reactant conversion was correlated with an increase in metallic Ru from the in-situ RuO $_2$ reduction in ethanol.

3.5. Catalyst stability and its recyclability

Metallic Ru was an active phase for hydrogenolysis of 1b and the Ru/C catalysts were reduced in-situ in the presence of ethanol. To assess the stability of the Ru/C catalyst, we recycled our catalyst four times and determined the reactant conversion and product selectivity. We used H₂-TPR to determine changes in the Ru content of the spent Ru/C catalysts after each recycle. We observed a slight increase in metallic Ru content after recycles (Figure S3). The reactant conversion increased in the second recycle from 52.5% (fresh Ru/C) to 73.1% (after second recycle) (Table S7) and progressively decreased to 55.5% after four recycles. With these results, we hypothesized that the catalyst deactivated because of the Ru leaching out of the carbon support into the solution. Thus, we performed an elemental analysis of the spent catalyst by EDS. Our EDS results showed ~50 wt.% decrease in Ru content in the spent catalyst after four recycles. These results suggested that the Ru was not stable in ethanol under the investigated condition and leached out in the solution. Previous studies have shown a similar leaching behavior of Ru into the reaction solution [175-177]. The stability of supported Ru depends on many factors, such as Ru precursors, types of supports, reaction solvents, and interactions between catalyst with reactants/intermediates/products [178]. Further investigation is needed to identify the root cause of Ru leaching and to improve the stability of the supported Ru for hydrogenolysis of lignin model compounds.

4. Conclusions

Lignin is a potential renewable aromatic feedstock. Rigidity and cross-linked lignin polymers make lignin difficult to be cleaved, releasing monoaromatic compounds. Lignin consists of ~50-65% β -O-4 aryl ether (C β -O) bonds and abundant aliphatic and aromatic hydroxyl groups. We have demonstrated that the Ru catalyst catalyzed the hydrogenolysis of C β -O bonds of a lignin model compound using the internal hydrogen source from C α -OH. These results provide an alternative and efficient strategy for lignin conversion without a requirement for external, high-pressure H₂. We pretreated Ru catalysts in various conditions and identified the metallic Ru as the active phase for hydrogenolysis of C β -O

bonds. X-ray diffraction (XRD) and H₂ Temperature-programmed reduction (TPR) measurements supported that the Ru was the active site for hydrogenolysis of C_β-O bonds. The use of alcohol as a reaction solvent enabled the in-situ reduction of RuO₂ from Ru/C, increasing catalytic activity over time. These results have potential application in lignin conversion to aromatic chemicals from pulp and paper manufacturing and from biorefineries.

Supporting information Chapter 3

Catalytic cleavage of the β-O-4 aryl ether bonds of lignin model compounds by Ru/C catalyst

Table S1. List of chemicals/reagents used in this study			
Chemical	Supplier	Purity	CAS Number
2-phenoxy-1-phenylethanol	Ark Pharm Inc.	97%	42487-72-3
2-phenethyl ether	phenyl Frinton Laboratories Inc.	98-99%	40515-89-7
Ethanol	VWR	200 proof	64-17-5
H ₂ gas	Welder supplies	research grade: 99.999%	-
O ₂ gas	Welder supplies	research grade: 99.998%	-
N ₂ gas	Welder supplies	industrial grade: 99.9995%	-

Table S2. Pretreatment conditions for the Ru/C catalyst		
Catalyst	Notation	Source
1	Ru/C	Commercial 5% Ru/C
2	pre-reduced Ru/C	Commercial pre-reduced 5% Ru/C
3	Ru/C-Red	Commercial 5% Ru/C (catalyst #1) reduced under H ₂ flow (40 cc/min) at 250°C for 3h and passivated in the air for 12h
4	Ru/C-Ox	Commercial 5% Ru/C (catalyst #1) oxidized under O ₂ flow (40 cc/min) at 200°C for 3h

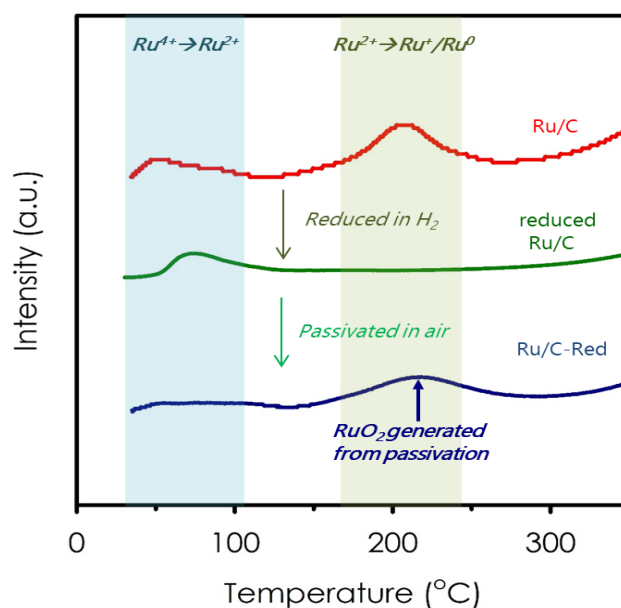
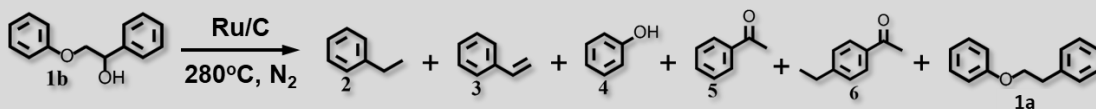


Figure S1. Changes in H₂-TPR profiles of Ru/C after reduction and passivation

Table S3. The Ru and RuO ₂ content (mol.%) calculated from H ₂ -TPR		
Catalyst	Ru metallic (%)	RuO ₂ (%)
Pre-reduced Ru/C	87	13
Ru/C-Red	86	14
Ru/C	82	18
Ru/C-Ox	75	25

Table S4. Composition of the Ru/C catalysts calculated from H₂-TPR and gravimetric analysis

Catalyst	Ru metallic (wt.%)	Ru in RuO ₂ (wt.%)	Oxygen (wt.%)	Carbon (wt.%)
pre-reduced Ru/C	4.15	0.64	0.20	95.00
Ru/C-Red	4.09	0.69	0.22	95.00
Ru/C	3.88	0.85	0.27	95.00
Ru/C-Ox	18.71	6.35	2.01	72.94

Table S5. Conversion and product selectivity of 2-phenoxy-1-phenylethanol over investigated catalysts.

Catalyst	Specific activity (mmol)/(g _{Ru} * h)	Selectivity (%)					
		2	3	4	5	6	1a
pre-reduced Ru/C	112	39.4	-	26.7	1.3	2.6	27.1
Ru/C-Red	77	26.3	5.8	34.8	10.1	1.9	20.7
Ru/C	65	25.4	6.8	34.6	8.2	3.7	20.1
Ru/C-Ox	4	9.2	10.9	39.2	25.0	9.4	6.2

Reaction condition: 280°C, 4 h, 8 bar N₂, 1 wt.% reactant/ethanol, 20 wt.% catalyst loading.

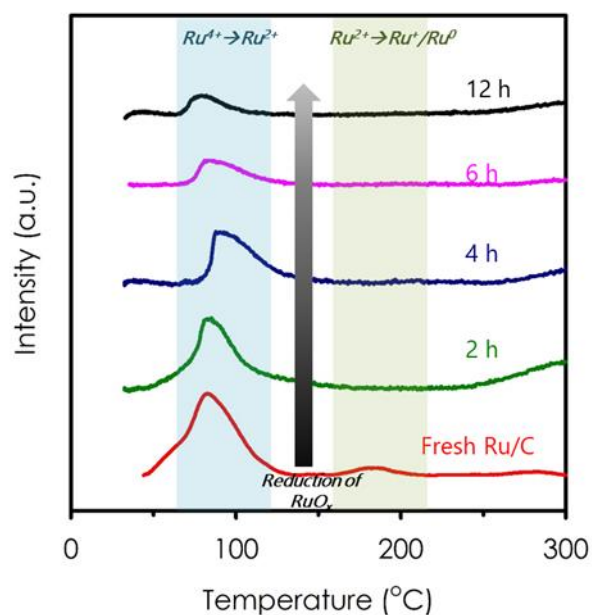
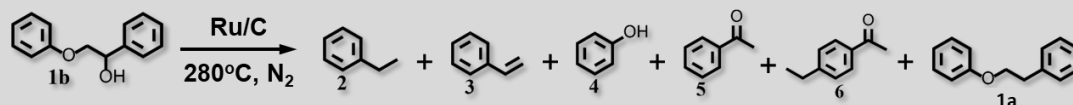


Figure S2. H₂-TPR profiles of the Ru/C catalyst over reaction time

Table S6. The evolution of conversion and product selectivity from the hydrogenolysis of 2-phenoxy-1-phenylethanol (1b) on the Ru/C catalyst as a function of reaction time and Ru content.



Time (h)	Conversion (%)	Selectivity (%)		Ru (%)
		Σ (2,3)	1a	
4	52.5	32.2	20.1	87.9*
6	94.8	35.4	26.5	88.1
12	99.7	31.3	30.5	96.5

Reaction condition: 280°C, 8 bar N₂, 1 wt.% reactant/ethanol, 20 wt.% catalyst loading. Ru (%) was determined from the H₂-TPR. *The fresh Ru/C had ~82% Ru content.

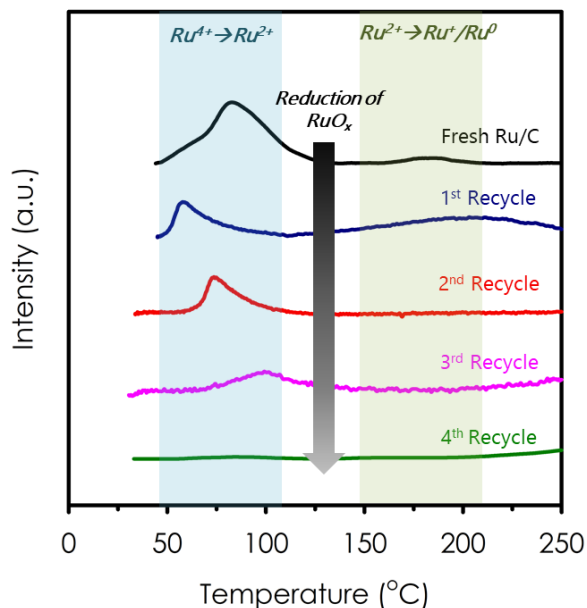
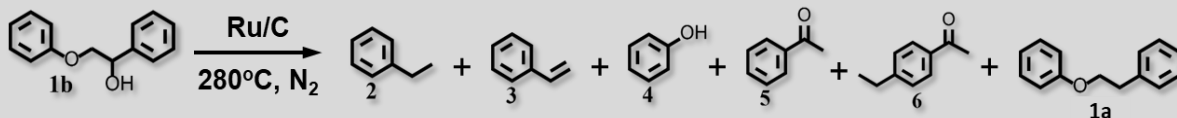


Figure S3. H₂-TPR profiles of the spent Ru/C catalyst after four recycles

Table S7. The change in conversion and product selectivity from the hydrogenolysis of 2-phenoxy-1-phenylethanol (1b) over Ru/C catalyst as a function of recycling and Ru content.



Run #	Conversion (%)	Selectivity (%)		Ru (%)
		Σ (2,3)	1a	
1	52.5	32.2	20.1	87.9*
2	73.1	33.8	21.0	86.2
3	63.3	33.1	19.8	87.3
4	55.5	25.3	12.5	92.9
1	52.5	32.2	20.1	87.9*

Reaction condition: 280°C, 4 h, 8 bar N₂, 1 wt.% reactant/ethanol, 20 wt.% catalyst loading.

Ru (%) was determined from the H₂-TPR. *The fresh Ru/C had ~82% Ru content.

CHAPTER 4
UNLOCKING SELF-HYDROGEN FOR HYDROGENOLYSIS AND MEERWEIN-
PONNDORF VERLEY REDUCTION OF LIGNIN BY DUAL FUNCTIONAL
Ru/RuO_x/C CATALYST

1. Introduction

Catalytic cleavage of aryl C-O ethers is an important step for lignin conversion to small phenolics for subsequent upgrading to fuels and chemicals [179-186]. The β -O-4 bonds are ~ 40-60% of total lignin linkages [22, 187]. As a result, to use lignin, it is important to break the abundant β -O-4 linkages to release phenolic monomers [188]. Hydrogenolytic cleavage of β -O-4 linkages is effective at breaking C-O bonds [189-199]. However, it requires a combination of high hydrogen pressure (> 10 bar) and polar solvents to improve hydrogen solubility for the reaction [191, 200]. The high hydrogen pressure leads to aromatic ring saturation (e.g., alkyl cyclohexanes and cyclohexanols), wasting the valuable hydrogen and aromaticity of the compounds.[201-203] The major challenge in lignin hydrogenolysis is the selective C-O cleavage without hydrogenating the aromatic rings [204-206]. Moreover, high pressure necessitates expensive equipment, increasing both the operating and capital costs of the process.[207] In addition, the limited amount of dissolved hydrogen in the solvents can cause undesired side reactions (coke formation) [208]. Hence, the amount of hydrogen in the reaction needs to be balanced for efficient hydrogenolysis of lignin.

Ru-based catalysts have been reported as active catalysts in lignin hydrogenolysis in the liquid phase [209-212]. Xiao et al. showed that the hydrogenolysis of enzymatic mild acidolysis lignin from willow was accomplished by Ru catalysts in methanol and 30 bar H₂ [213]. Wu et al. revealed that the Ru catalyst catalyzed hydrogenolysis of lignin model C-O compounds using 2-propanol as the hydrogen-donor source [214]. Li et al. used Ru catalysts to hydrogenolyze birch organosolv lignin in methanol under 30 bar H₂, which provided 26.6 wt.% monomers [215]. Liu et al. used Ru/C catalyst to hydrogenolyze deep-eutectic solvent fractionated lignin at 220-220°C under 40 bar H₂ [216]. The resulting monomer yield was 24 wt.%. Recently, we found that Ru catalyst was active in catalyzing the model β -O-4 compound with C α -OH groups without hydrogen-donor solvents and/or external H₂ [202]. The Ru catalyst was easily passivated and contained RuO_x. However, the mechanism of this hydrogenolytic cleavage of C α -OH groups by the Ru/RuO_x catalyst has not been explained. The lack of this information slows down the conversion of lignin in biorefineries.

In this contribution, we reported the mechanistic study by which the aliphatic OH groups (C α -OH) affected the hydrogenolysis of lignin model compounds and four technical lignin by the Ru/RuO_x/C catalyst. We demonstrated that the presence of C α -OH groups promoted Ru-catalyzed dehydrogenation of the lignin model compound into the keto intermediate and facilitated the β -O-4 cleavage using self-hydrogen; the use of hydrogen-donor solvents was not necessary. Further, we elucidated alcohols, hydrogen-donor solvents, enabled the Meerwein–Ponndorf–Verley reduction of the keto products by RuO_x, and facilitated subsequent hydrodeoxygenation and hydrogenation to hydrocarbons.

1. Materials & Methods

1.1. Materials

The 2-phenoxy-1-phenylethanol (PPE-OH) [190, 217, 218], 2-phenethyl phenyl ether (PPE) [219-221], veratrylglycerol- β -guaiacyl ether (VGE)[222-224] were used as model β -O-4 compounds. PPE-OH and PPE contained C α -OH and C α -H, respectively. VGE had C α -OH with methoxy substitute on the ring to represent the realistic functional groups on

technical lignin. The Ru/RuOx/C catalyst used in this study was the commercial 5% supported Ru catalyst on activated carbon from Alfa Aesar (Haverhill, MA, USA). The Ru⁰ and RuOx, measured by H₂ temperature-programmed reduction (H₂-TPR), were 59 and 41 wt.%, respectively. The H₂-TPR procedure was explained in the Method section. The pre-reduced Ru/C catalyst was used as a control. All reagents and catalysts were used as received unless otherwise noted. They were stored in the glove box to prevent oxidation. Their manufacturers, purity, and CAS numbers are shown in Table S1.

1.2. Hydrogenolysis of lignin model β -O-4 compounds

All reactions were performed in a 25 mL autoclave reactor (Parr Instrument, Moline, IL, USA). The reactant concentration was ~1 wt.% of lignin model compounds in organic solvents unless otherwise noted. The catalyst loading was 20 wt.% (~20 mg catalyst, 2 mol.% Ru) with respect to reactant (100 mg reactant in 10 g solvent solution). Before the reaction, the reactor was purged three times with N₂ to remove air. The reactor was then pressurized to 8 bar N₂ or H₂ at ambient temperature to minimize the evolution of hydrogen and the consistency of the experiment. The hydrogenolysis reaction was performed at 280 °C for 4 h with a stirring rate of 600 rpm to minimize mass transfer limitation. The reaction was stopped by quenching in a cold water bath. The reaction sample was withdrawn, centrifuged to remove residual solids, and diluted with ethanol before product analysis.

1.3. Reaction product identifications and quantifications

Changes in reactants and products during the cleavage of β -O-4 bonds were identified and quantified by the Agilent 7890B GC (Agilent Technologies, Santa Clara, CA, USA) equipped with Mass spectrometry (MS) and Flame Ionization Detectors (FID). An HP-5MS column (30m \times 0.25mm \times 0.25 μ m, Agilent Technologies, Santa Clara, CA, USA) was used for product separation with the following temperature program: injection temperature 275 °C and FID detector temperature 300 °C; split ratio 1:50. The temperature program started at 45 °C and increased at 10 °C/min to 250 °C, then held for 20 min. The change in reactant and products was determined using dodecane as the internal standard. Reactant conversion, product yield, and product selectivity were calculated as follows:

$$\text{Conversion (\%)} = \frac{\text{reactant reacted (mol)}}{\text{reactant initial (mol)}} \times 100\%$$

$$\text{Yield (\%)} = \frac{\text{product formed (mol)}}{\text{reactant initial (mol)}} \times 100\%$$

$$\text{Selectivity (\%)} = \frac{\text{yield (\%)}}{\text{conversion (\%)}} \times 100\%$$

1.4. Elemental analysis of technical lignins

The C, H, N, S contents of technical lignins were analyzed by the Perkin Elmer CHNS 2400 Series II Analyzer (Waltham, MA, USA). The detection limit for C, H, N, and S is 0.2%. The oxygen content was calculated by subtraction (O [wt.%] = 100 - the sum of CHNS).

1.5. Nuclear Magnetic Resonance Spectroscopy

To quantify the relative amounts of hydroxyls at the C_α-position in each of the technical lignins, we used two-dimensional (2D) heteronuclear single quantum correlation (HSQC) Nuclear Magnetic Resonance (NMR) experiments. Briefly, approximately 60 mg of technical lignins (steam-exploded yellow poplar, soda, organosolv, and kraft lignins) were weighed into a 7 inch 5-mm NMR tube and dissolved directly in 500 μl DMSO-*d*₆ and sonicated for 1 h. The dissolved samples were homogeneous, translucent, and flowable solutions. NMR spectra were acquired on a Bruker-Biospin AVANCE III HD™ 500 MHz spectrometer (Rheinstetten, Germany) fitted with a nitrogen-cooled 5-mm Prodigy™ TCI gradient cryoprobe with inverse geometry. HSQC experiments were acquired using adiabatic Bruker pulse program hsqcetgpsisp2.2 with an FID size (TD) of 2048 and 1024 (F2 and F1), acquisition time (AQ) of 0.170 and 0.0189 sec. (F2 and F1), 8 scans, and delay (D1) of 1. The HSQC spectra were processed and integrated as previously described[225] using TopSpin 3.6.2 software such that the ¹H and ¹³C of the C_α contour were semi-quantifiable relative to the methoxyl contour.

1.6. H₂ temperature-programmed reduction

To investigate the reduction of the Ru/RuO_x/C catalyst, H₂ Temperature-Programmed Reduction (H₂-TPR) experiments were performed by a Micromeritics ChemiSorb 2720 equipped with a thermal conductivity detector (TCD) (Norcross, GA, USA). About 20-40 mg of sample was pretreated at 250°C for 1h under He flow to remove adsorbed water. Then, the sample was cooled to ambient temperature under He flow. TPR profiles were recorded by heating the samples from ambient temperature to 800°C at 10°C/min in 10.01% H₂/Ar at a flow rate of 40 cc/min. The amount of metallic Ru and RuO_x was determined by integrating the H₂ consumption profile with respect to the H₂ standard. The Ru and RuO_x were 59 and 41 wt.%, respectively. Hence, we referred to our catalyst as Ru/RuO_x/C throughout the manuscript.

1.7. Computational methods

To elucidate the hydrogenolytic mechanism, the density functional theory (DFT) was performed by creating the model Ru catalyst and lignin model compounds using the Vienna ab initio simulation package (VASP) Version 5.4.4.[226-229] The detailed information of computational parameters, model construction of the Ru surface, and optimized structures of model compounds (**Figs. S1-S3** and **Table S2**), are shown in *Supplementary Information*.

2. Results

2.1. Effect of C_α-hydroxyl groups on the cleavage lignin model compounds by Ru/RuO_x/C

To assess the importance of the C_α-OH on the hydrogenolysis of the β-O-4 bond, we run reaction in 2-Butanone over Ru/RuO_x/C catalyst under N₂, using 2-phenyl ethyl phenyl ether (PPE, 1a), 2-phenoxy-1-phenylethanol (PPE-OH, 1b), and veratrylglycerol-β-guaiacyl ether (VGE, 1c) as model compound of lignin. We choose 2-Butanone and N₂ to eliminate the contribution of H₂ from external sources. There were only ~4% conversion of the PPE model compound after 4h of reaction in 2-Butanone at 280 °C reaction temperature. On the contrary, when the reaction was conducted with the PPE-

OH and VGE model compound, 88 and 69 % conversion were achieved respectively. In case of the PPE-OH (1B), phenol (4) and acetophenone (5) are the major products from the cleavage of the β -O-4 bond, where 4-methoxyphenol/ guaiacol (6) and 4-allyl-1,2-dimethoxybenzene /methyl eugenol (7) are the major product from VGE (1c). This product distribution from the reactions suggest for the selective cleavage of the β -O-4 bond functional group plays an important role. Moreover, the unreactivity of PPE (1a) suggested that C_{α} -OH was critical in the enhanced reactivity of model β -O-4 compounds for hydrogenolysis by Ru/RuO_x/C catalyst without hydrogen-donor solvents and external H₂.

We further assess the importance of the C_{α} -OH, we performed conversion of these three model β -O-4 compounds, using Ru/RuO_x/C catalyst in dioxane under N₂ (**Fig. 1**). We chose dioxane and N₂ to decouple the hydrogen contribution from hydrogen-donor solvents (alcohols) and external H₂. Heating these model compounds with Ru/RuO_x/C catalyst in dioxane under N₂ differed in reactant conversion. When using PPE, we observed little to no conversion. Whereas PPE-OH and VGE showed a similar conversion of ~51-53%. We observed phenol (4) and acetophenone (5) as major products from PPE-OH (1b) and 4-methoxyphenol/ guaiacol (6) and 4-allyl-1,2-dimethoxybenzene /methyl eugenol (7) from VGE (1c). These products suggested that PPE-OH (1b) and VGE (1c) underwent hydrogenolysis and the presence of methoxy groups in VGE (1c) did not hinder the reactivity to hydrogenolysis. Moreover, the unreactivity of PPE (1a) suggested that C_{α} -OH was critical in the enhanced reactivity of model β -O-4 compounds for hydrogenolysis by Ru/RuO_x/C catalyst without hydrogen-donor solvents and external H₂.

To determine the effect of alcohols as hydrogen-donor solvents in hydrogenolysis of lignin model compounds, we conducted hydrogenolysis by Ru/RuO_x/C catalyst in ethanol under N₂ on PPE (1a), PPE-OH (1b), and VGE (1c) (**Fig. S4A**). PPE (1a) was not reactive to hydrogenolysis by Ru/RuO_x/C catalyst. Whereas heating PPE-OH (1b) and VGE (1c) with Ru/RuO_x/C catalyst in ethanol resulted in cleavage of β -O-4 bond. PPE-OH (1c) yielded 53% conversion with 25% ethylbenzene (2), 7% styrene (3), 35% phenol (4), and 8% acetophenone (5), and 20% PPE (1a) selectivities. A greater ethylbenzene (2) selectivity in ethanol compared with that in dioxane suggested that ethanol promoted

hydrodeoxygenation and hydrogenation reactions. VGE (1c) yielded 99% conversion with 45% 1-ethyl-4-methoxybenzene (6), 43% 4-methoxyphenol (7), 10% 4-methoxyphenethyl alcohol (8) selectivities. These results suggested (1) C α -OH played a crucial role in the hydrogenolysis of β -O-4 bond, and (2) hydrogen-donor solvent (ethanol) promoted subsequent side reactions, but it was not necessary.

Next, we performed the same hydrogenolysis of PPE (1a) and PPE-OH (1b) in H₂ by Ru/RuO_x/C catalyst. Under H₂, we obtained 51% PPE conversion with 13% ethylbenzene (2), 8% phenol (4), and 68% 4-methoxyphenol (7) selectivities, compared with no activity under N₂. Moreover, we obtained 89% PPE-OH conversion under H₂ with 26% phenol (4), 3% acetophenone (5), and 27% 4-methoxyphenethyl alcohol (8) selectivities, a conversion higher than under N₂ (53%). These results suggested that added H₂ enhanced the hydrogenolysis rates of β -O-4 bonds by Ru/RuO_x/C. Together, these results confirmed that the presence of C α -OH group was important in activating the hydrogenolysis of the β -O-4 bond.

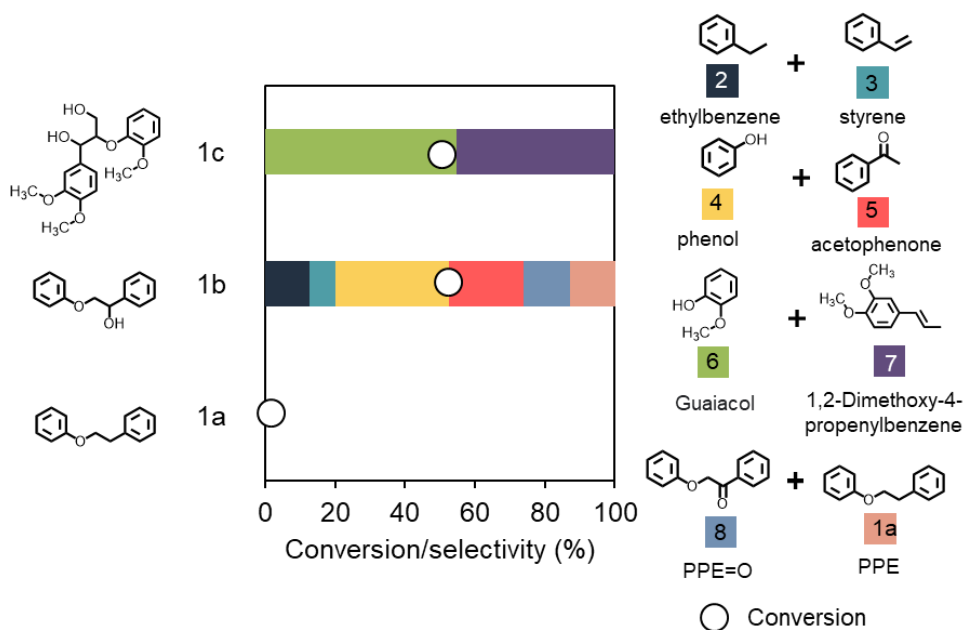


Figure 1. Cleavage of β -O-4 linkages of veratrylglycerol- β -guaiacyl ether (1c), 2-phenoxy-1-phenylethanol (1b), and 2-phenyl ethyl phenyl ether (1a) by Ru/RuO_x/C in dioxane under N₂. Reaction condition: 280°C, 8 bar N₂, 1 wt.% reactant/dioxane, 20 wt.% catalyst loading, 4h.

To decouple the contribution from Ru and RuO_x, we tested the RuO₂ catalyst for hydrogenolysis PPE, PPE-OH, and VGE in dioxane. The RuO₂ catalyst was not active for hydrogenolysis of PPE, PPE-OH, and VGE in dioxane (**Fig. S5**). Whereas RuO₂ in ethanol yielded similar products as those in dioxane (**Fig. 1**). These results suggested that Ru in Ru/RuO_x/C activated C_α-OH group for hydrogenolysis of β-O-4 bonds of model β-O-4 compounds.

2.2. Charge analysis of reactant adsorption on Ru(111) surface

To elucidate how C_α-OH group promoted β-O-4 hydrogenolysis, we performed the charge analysis using charge density differences (CDD), and the Bader charge analysis to investigate the adsorption stability of PPE and PPE-OH on the Ru (111) surface (**Fig. S6**). The positive and negative Bader charge change values (ρ) described electron gain and loss during an adsorption process, respectively. During PPE and PPE-OH adsorption, the electron depletion from the top Ru (111) surface and electron accumulation around carbon atoms of the benzene rings suggested that strong adsorption of PPE and PPE-OH take place by an electron transfer from Ru (111) surface to the two benzene rings of PPE and PPE-OH. Moreover, in the case of PPE, a shorter atomic distance between O1 of PPE and Ru (111) surface indicated another contact point between PPE and Ru (111) surface apart from the benzene rings, which resulted in stronger adsorption between PPE molecule and Ru (111) surface (**Table S3**).

Compared with PPE adsorption on Ru (111), PPE-OH adsorption increased the distance between the O1 atom and the Ru (111) surface and decreased the distance between H1 and Ru (111). These results suggested that the presence of -OH reduced the O1-Ru (111) interaction and promoted the H1-Ru (111) interaction (which is weaker than O1-Ru (111) interaction).[230] Furthermore, the Bader charge analysis suggested that the Ru (111) surface acted as an electron donor to the adsorbed PPE and PPE-OH. Moreover, a higher electron gain of the PPE-OH molecule (+2.17 |e|) indicated the PPE-OH was more active than PPE. Interestingly, the majority of the electron gain on the PPE-OH was located around the H1 atom. Whereas the electron gains were dispersed throughout the PPE

molecule. Thus, we postulated that the electron accumulation at the H1 atom of PPE-OH promoted the dehydrogenation of the PPE-OH molecule. This dehydrogenation step of H1 in PPE-OH was essential to the O1-C1 bond activation (β -O-4 cleavage), which corroborated previous findings [134, 231, 232]. The undetected O1-C1 bond cleavage in PPE was speculated due to the lack of this dehydrogenation step.

3.3 Mechanistic study of O1-C1 bond cleavage in PPE and PPE-OH on Ru (111) surface

To test the abovesaid hypothesis, we further investigated the O1-C1 activation (β -O-4) mechanism in PPE and PPE-OH using their stable configurations and calculated the enthalpy of the proposed reaction step (**Fig. 2**). The initial PPE and PPE-OH adsorption on the Ru (111) surface was denoted as **ISA** and **ISB**, respectively. For the PPE system, the O1-C1 bond of **ISA** was directly cleaved to the distance of 3.96 Å, which formed the final hydrogenolysis product, **FSA**, with the reaction enthalpy of -0.93 eV (**Fig. 2A**). Based on our charge analysis, we concluded that the cleavage of PPE-OH proceeded by the formation of an intermediate. Thus, we postulated that for the PPE-OH system, the O1-C1 bond of **ISB** was cleaved by two possible pathways: (1) direct cleavage to **FSB1** (**Fig. 2B**) and (2) indirect cleavage by forming intermediate (int B) before the final product **FSB2** (**Fig. 2C**). We found that the direct O1-C1 cleavage in the direct cleavage had the ΔH of -1.31 eV with the O1-C1 atomic distance in **FSB1** of 2.99 Å (**Table 1**).

The indirect O1-C1 cleavage proceeded with the deprotonation of H1 in **ISB** to Ru(111) surface to form an intermediate int B with ΔH of -0.78 eV and then hydrogenolysis to form **FSB2** with the ΔH of -1.07 eV. The indirect cleavage of PPE-OH resulted in the total enthalpy changes of 1.85 eV, higher than that of the direct cleavage. These results suggested that the indirect pathway (**ISB** to **FSB2**) was more favorable than that of the direct one (**ISB** to **FSB1**). These results further suggested the C_{α} -OH group in PPE-OH promoted the dehydrogenation of H1 and formed a keto intermediate (PPE=O) before hydrogenolysis of β -O-4 bonds into keto product (acetophenone) and phenol. These calculations were in good agreement with the hydrogenolysis results of lignin model compounds (**Fig. 1**).

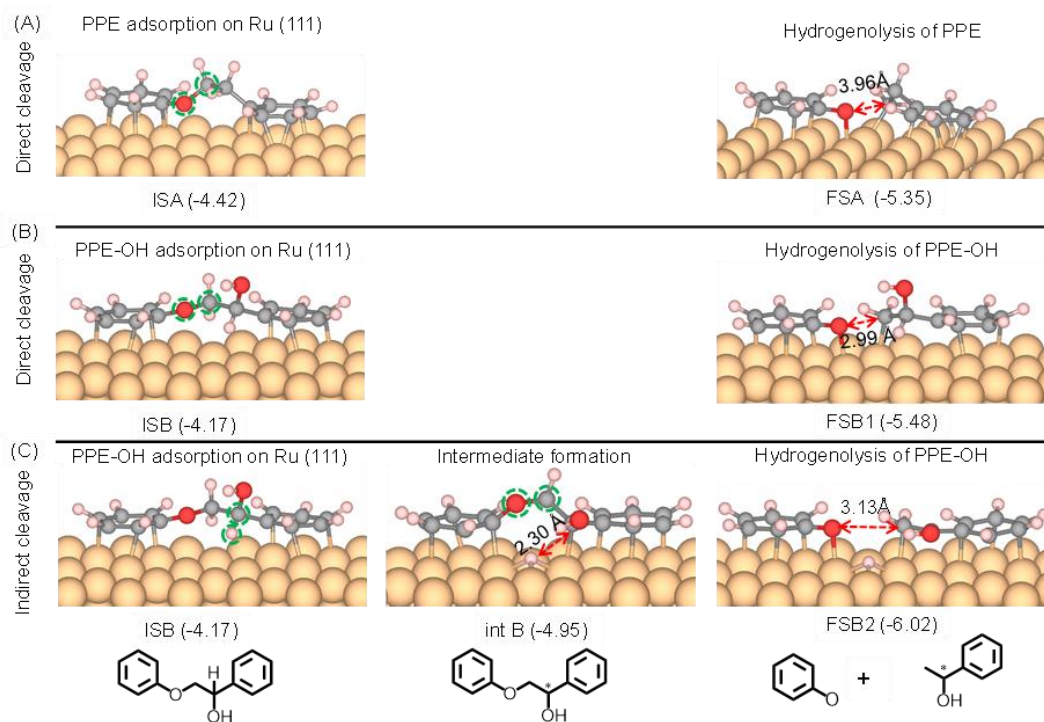


Figure 2. Mechanistic study of the hydrogenolysis of O1-C1 bond on Ru(111) of the PPE and PPE-OH reactant proceeding by (A) direct hydrogenolysis of PPE and (B) PPE-OH and (C) indirect hydrogenolysis of PPE-OH. Note that IS, int, and FS denoted initial structure, intermediate, and final structure, respectively. The value in the bracket is the enthalpy of that stage.

To understand how reaction solvents affected β -O-4 hydrogenolysis and promoted side reactions (hydrodeoxygenation and hydrogenation), we performed hydrogenolysis of PPE-OH by Ru/RuO_x/C catalyst under N₂ in (1) aprotic solvents (dioxane, ethyl acetate, and 2-butanone) and (2) protic solvents (ethanol, 1-propanol, 2-propanol, and 2-butanol) (**Fig. 3**).

Table 1. Enthalpy (ΔH) in eV of direct PPE and PPE-OH hydrogenolysis, and the indirect hydrogenolysis of PPE-OH all on Ru(111) surface

Reaction Pathway	Reaction step	ΔH (eV)
Direct hydrogenolysis	ISA to FSA	-0.93
	ISB to FSB1	-1.31
Indirect hydrogenolysis	ISB to int B (dehydrogenation)	-0.78
	Int B to FSB2 (hydrogenolysis)	-1.07

3.5. Effect of solvents on the formation of keto intermediate and β -O-4 bond cleavage of lignin model compounds

On the basis of our computational findings that the presence of the C_{α} -OH group in PPE-OH facilitated the dehydrogenation and β -O-4 bond cleavage, we expected to observe the β -O-4 bond cleavage of PPE-OH in both aprotic and protic solvents. As expected, the Ru/RuO_x/C catalyst was active in hydrogenolysis of PPE-OH (1b) in both aprotic and protic solvents, with the conversion of PPE-OH higher than 50% (*see detail in Supplementary Information*). The 2-phenoxy-1-phenylethanone (PPE=O) (8) was formed as a product in both solvent systems. The evolution of PPE=O over time in dioxane had a volcano shape (**Fig. S7**). Moreover, the decrease in PPE=O corresponded to increased phenol (4) and acetophenone (5) selectivities. These results suggested that PPE=O was an intermediate product and converted to phenol and acetophenone (*see details in the Supplementary Information*). It should be noted that the formation of PPE=O was fast in 2-propanol (**Fig. S8**). Moreover, we observed the saturated phenolics and aromatics, which is in agreement with the literature reported findings.[233-236] These results suggested that protic solvents facilitated not only the hydrogenolysis but also subsequent hydrodeoxygenation and hydrogenation.

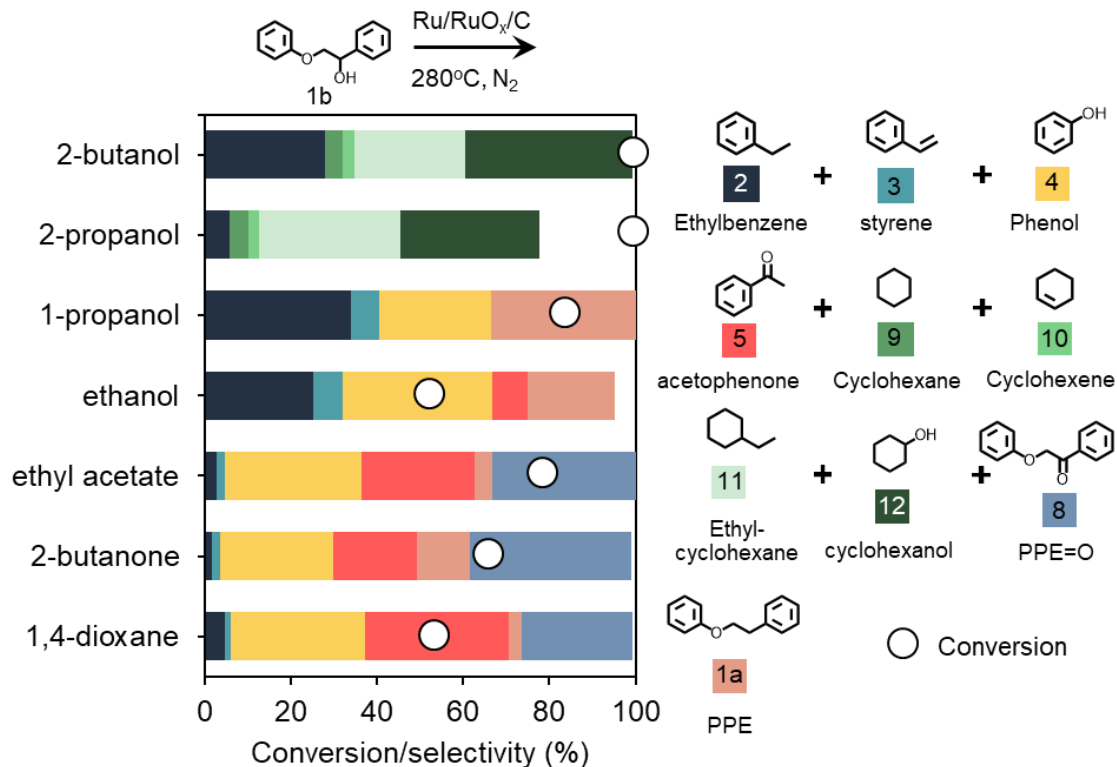
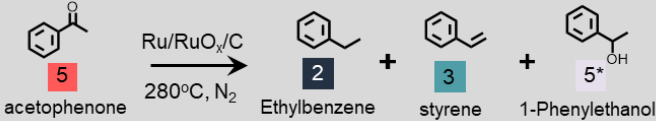


Figure 3. Cleavage of the β -O-4 bond of 2-phenoxy-1-phenylethanol (PPE-OH, 1b) by Ru/RuO_x/C in selected protic and aprotic polar solvents. Reaction condition: 280°C, 4 h, 8 bar N₂, 1 wt.% 2-phenoxy-1-phenylethanol/solvent, 20 wt.% catalyst loading.

Next, we determined the effect of donor number of solvents on the C-O cleavage or hydrodeoxygenation selectivity (**Fig. S9**). The β -O-4 cleavage took place in both solvent systems. However, protic solvents promoted hydrodeoxygenation. An increase in donor number enhanced the hydrodeoxygenation. Finally, we characterized the used Ru/RuO_x/C catalyst in selected solvents by H₂-TPR to determine the Ru/RuO_x ratio change. The Ru/RuO_x ratio of used catalysts followed the donor number of reaction solvents (**Table S4**). Together, these results suggested that (1) PPE-OH underwent dehydrogenation into PPE=O, a keto intermediate, in both aprotic and protic solvents, which corroborated our quantum calculations showing C $_{\alpha}$ -OH promoted the dehydrogenation by Ru catalyst (**Fig. 2**) and (2) hydrogen donating ability of solvents affected the oxidation state of Ru catalysts and subsequent hydrodeoxygenation.

2.3. Meerwein–Ponndorf–Verley (MPV) reduction initiated hydrodeoxygenation

To identify the formation pathway of styrene and ethylbenzene, we performed similar experiments using Ru/RuO_x/C catalyst and acetophenone (keto product, 5) as the reactant in dioxane and ethanol. We selected these solvents as proxies for aprotic and protic solvents. Using dioxane as a solvent, we had no catalytic activity (<3%) (**Table 2**). In contrast, we had 24% acetophenone conversion in ethanol after 0.5 h. We observed three reaction products, ethylbenzene (2), styrene (3), and 1-phenylethanol (5*). The presence of ethylbenzene and styrene suggested the hydrodeoxygenation of acetophenone only took place in protic solvents. The presence of 1-phenylethanol suggested the occurrence of MPV reduction. Moreover, we observed a decrease in benzyl alcohol and an increase in ethylbenzene yields over time. These results indicated that 1-phenylethanol underwent hydrodeoxygenation into styrene and subsequent hydrogenation into ethylbenzene.

Table 2. Acetophenone conversion by Ru/RuO _x /C in ethanol and dioxane						
						
Solvent	Entry	Time (h)	Conversion (%)	Selectivity (%)		
				2	3	5*
Ethanol	1	0.5	24	58	4	22
	2	1	33	77	5	18
	3	2	73	83	4	2
Dioxane	4	0.5	<3	-	-	-
	6	2	<3	-	-	-

Reaction condition: 280°C, 4 h, 8 bar N₂, 1 wt.% 2-phenoxy-1-phenylethanol/solvent, 20 wt.% catalyst loading. HDO extent = sum of 2 and 3 selectivities. MPV extent = selectivity of 5*.

Our catalyst contained 41% RuO_x (Ru/RuO_x ratio = 1.4, **Table S4**). The Ru/RuO_x ratio of the used catalysts in dioxane remained fairly constant (1.6). Whereas used catalysts in ethanol showed an increase in Ru/RuO_x ratio (3.8), which suggested that RuO_x was reduced into metallic Ru in ethanol. We expected that the oxygen vacancies in RuO_x were

the active sites for the MPV reaction of acetophenone to styrene and subsequent ethylbenzene. So we reduced the Ru/RuO_x/C catalyst in ethanol for 12h to increase the Ru/RuO_x ratio from 1.4 to 10.1 and used acetophenone as a reactant. As a control, the fresh Ru/RuO_x/C catalyst was active for MPV as evidenced by 96% selectivity to ethylbenzene and benzyl alcohol at 73% acetophenone conversion after 2 h (**Table S5**). Whereas the reduced Ru/RuO_x/C catalyst in ethanol for 2h showed only 25.5% conversion of acetophenone after 2h. At a prolonged reaction time of 6h, the reduced catalyst showed 40% MPV extent, lower than that of fresh catalyst at a similar conversion. We also observed a byproduct, (1-ethoxyl)benzene, 6*), which suggested that etherification occurred. These results suggested that RuO_x was the active site for the MPV. Moreover, MPV initiated hydrodeoxygenation and hydrogenation.

2.4. Validation with technical lignin and proposed chemical pathway of breaking lignin by Ru/RuO_x/C

The chemical structure of technical lignin is more complex than that of model compounds. Although the β -O-4 bond is the most abundant lignin linkage, technical lignin contains functional groups (i.e., methoxy) and other C-O bonds (α -O-4 and 4-O-5) and C-C bonds (β -5 and β - β) [237, 238]. These functionalities and bonds affected the hydrogenolysis activity of catalysts and product distribution. To validate the importance of the C α -OH group of lignin's β -O-4 cleavage, we applied Ru/RuO_x/C to four types of technical lignin: (1) steam-exploded yellow poplar lignin (YL), (2) organosolv lignin (OL), (3) kraft lignin (KL) and (4) soda lignin (SL) using ethanol as a solvent. We identified nine phenolic monomers as reaction products (**Fig. 4**). Of the technical lignin, YL gave the highest monomer yield of 28 wt.% after 12h (**Table S6**). A further increase in reaction time from 12 to 24h did not improve the product yield. Similarly, OL and SL gave an increase in monomer yield from 4 to 12h. A further increase in reaction time from 12 to 24h did not improve their monomer yields. The overall monomer yield of 28 wt.% from YL is higher than those in the literature [25, 239]. For example, Wang et al. reported ~10 wt.% yields of phenolic monomers from technical lignin by Mo-derived catalysts.[240] Because we expected that the foregoing monomer yield of 28 wt.% from YL lignin was due to its high

C_{α} -OH and C_{α} =O concentrations, we performed HSQC NMR on technical lignin samples to determine the C_{α} -OH and C_{α} =O contents (**Fig. S10**).

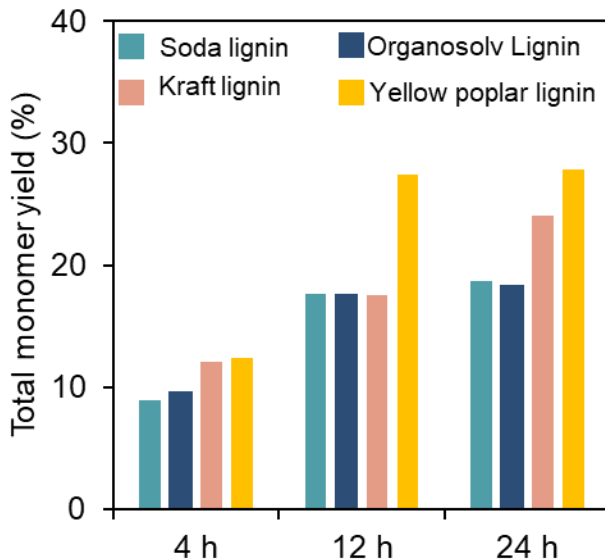


Figure 4. Hydrogenolysis of the technical lignin over Ru/RuO_x/C catalyst in ethanol under N₂. Reaction condition. 280°C, 8 bar N₂, 1 wt.% lignin, 20 wt.% catalyst loading.

From the HSQC spectra of the technical lignin and the corresponding integral data (**Table S7**), the quantity of C_{α} -OH groups was the highest in the YL, closely followed by the KL and SL. The OL gave the lowest amount of C_{α} hydroxyls. The quantity of C_{α} =O groups was the highest in SL, followed by YL and KL. Looking at the percent of the sum of the integrals for C_{α} , YL had the highest total integral, followed by KL, SL, and OL. Interestingly, the ranking of the total C_{α} integral was in the same order as the hydrogenolysis yield. These results suggested the importance of C_{α} -OH groups in the cleavage of the β -O-4 bond. Since YL has a higher C_{α} integral compared to other lignin, using YL provided a higher amount of monomer yields. Similarly, after C_{α} -OH and C_{α} =O were utilized, no further hydrogenolysis of YL occurred. We found that there was a threshold in relative integrals of C_{α} -OH that promoted the total hydrogenolysis yield (**Fig. 5**). The total integrals of C_{α} higher than 0.04 considerably enhanced the hydrogenolysis of lignin. Surprisingly, although KL had a high sulfur content of 0.9 wt.%, the hydrogenolysis

yield of KL at 24h was 24 wt.%, higher than those of OL and SL, which had 0.2-0.3 wt.% sulfur. Sulfur typically poisoned metal catalysts, such as Pt, Co, and Ni [241-243]. Future studies will determine the fate of sulfur in lignin and how sulfur content affects metal catalysts and lignin hydrogenolysis activity.

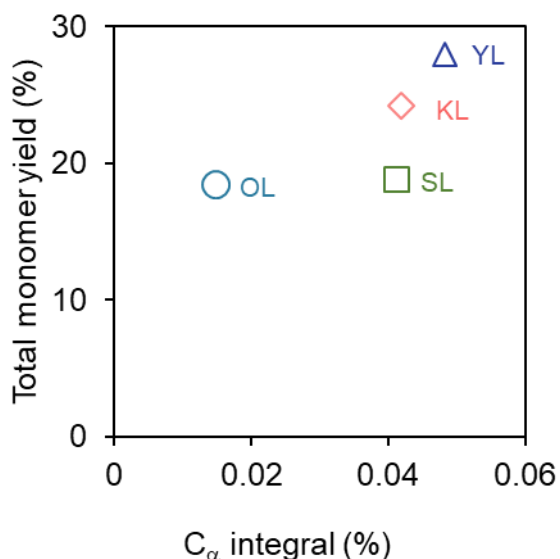


Figure 5. Correlation between total C_{α} integral and hydrogenolysis yield of technical lignin. Total C_{α} integral = area of C_{α} -OH + C_{α} =O. Condition: Reaction condition: 280°C, 8 bar N_2 , 1 wt.% Lignin, 20 wt.% catalyst loading, and 24 h. YL= yellow poplar steam-exploded lignin, OL = organosolv lignin. KL= kraft lignin, SL = soda lignin

3. Discussion

In this work, we identified the effect of C_{α} -OH groups for hydrogenolysis of model β -O-4 compounds and technical lignin by the Ru/RuO_x/C catalyst using combined experiments and computations. The challenge in lignin hydrogenolysis is the selective cleavage of C-O bonds without hydrogenating the aromatic rings to preserve the aromatic values of monomers [204-206, 244]. Here, we showed the presence of C_{α} -OH groups in lignin model compounds initiated the dehydrogenation of C_{α} -OH into the keto intermediate (C_{α} =O), which facilitated the hydrogenolysis of β -O-4 bonds into phenol and keto product (acetophenone) without added hydrogen-donor solvents and external H₂ gas. Using

hydrogen-donor solvents enabled the Meerwein–Ponndorf–Verley (MPV) reduction of the keto product and facilitated the hydrodeoxygenation and hydrogenation. We applied this concept to four technical lignin with varying C_{α} -OH and C_{α} =O contents to validate this concept of C_{α} -OH promoted hydrogenolysis of lignin.

Our most significant finding was that hydrogen-donor solvents initiated the MPV reduction of the keto product (acetophenone) by Ru/RuO_x/C catalyst and facilitated its subsequent hydrodeoxygenation to styrene and hydrogenation to ethylbenzene. Most lignin hydrogenolysis studies used H₂ gas and/or alcohols as reaction solvents to enhance the H₂ solubility for C-O cleavage. The oxophilic nature of the Ru catalysts enables the formation of the RuO_x Lewis acid sites under a reducing environment, such as alcohols [245-248]. These RuO_x species are active sites for MPV reduction. Jae et al. reported that RuO₂ mainly catalyzed MPV reaction of the 5-hydroxymethylfurfural to 2,5-bis(hydroxymethyl)furan in propanol and metallic Ru catalyzed hydrogenolysis of 2,5-bis(hydroxymethyl)furan to dimethylfuran [172]. Jenness et al. used Density Functional Theory to demonstrate that RuO₂ surface catalyzed MPV of furfural to furfuryl alcohol [249]. These results corroborate our findings. In contrast, Mironenko et al. [248] and Gilkey et al. [245] showed the both Ru and RuO₂ catalyzed MPV reduction of furfural to furfuryl alcohol in 2-propanol. The RuO₂ catalyzed direct intermolecular hydride transfer from alcohol to furfural. However, the metallic Ru followed a Horiuti-Polanyi-type reaction. Hence, we could not rule out the possibility of metallic Ru catalyzed the keto product's hydrogenation and facilitated the hydrodeoxygenation. Further studies will focus on identifying the hydrogenation pathway of metallic Ru. Together, MPV reduction of the keto product (acetophenone) in hydrogen donor solvents (ethanol) by the RuO_x in Ru/RuO_x/C catalyst was a key step that led to hydrodeoxygenation and hydrogenation products. Hence, the choice of solvents in Ru/RuO_x/C catalytic systems affected product selectivity [210, 250, 251].

Another significant finding was the elucidation of the chemical pathway of the β -O-4 hydrogenolysis by the Ru/RuO_x/C catalyst, which involved the C_{α} -OH groups of lignin in promoting the dehydrogenation to the keto intermediate (C_{α} =O) without the hydrogen-donor solvents and H₂. Luo et al. [252] showed that C_{α} -OH of the lignin β -O-4 model

compound acted as a hydrogen donor group and facilitated the photo-mediated hydrogenolysis by ZnIn_2S_4 . Our previous work demonstrated that the presence of the $\text{C}_\alpha\text{-OH}$ group enabled the $\beta\text{-O-4}$ bond cleavage of lignin $\beta\text{-O-4}$ model compounds by the Ru catalyst [253]. Given that most studies use alcohols as solvents for hydrogenolysis of lignin $\beta\text{-O-4}$ model compounds to increase solubility of the reactants and products and or provide hydrogen, we need to decouple the effect of chemical functionality and hydrogen-donor solvents on the hydrogenolysis reaction.

In contrast to these findings, this dehydrogenation step occurs without hydrogen-donor solvents and/or H_2 . Zhou et al. [254] and Andrade et al. [255] investigated Pd catalysts for hydrogenolysis of model $\beta\text{-O-4}$ compounds with $\text{C}_\alpha\text{-OH}$. They observed a keto intermediate and proposed the hydrogenolysis of $\beta\text{-O-4}$ bonds by Pd catalysts underwent keto-enol tautomerization intermediate step prior to $\beta\text{-O-4}$ cleavage into the keto product. These results are in agreement with our observation in the Ru catalyst system.

This dehydrogenation step facilitated the cleavage of $\beta\text{-O-4}$ bonds because the keto intermediate had a lower bond dissociation energy of the $\beta\text{-O-4}$ bond (227.8 kJ/mol with $\text{C}_\alpha=\text{O}$) compared with that of $\text{C}_\alpha\text{-OH}$ (274.0 kJ/mol) [232]. These results are consistent with the previous observations by Rahimi et al. [256] and Nguyen et al. [257], showing that the oxidized lignin ($\text{C}_\alpha=\text{O}$) enabled a facile $\beta\text{-O-4}$ cleavage. Although these studies suggested the importance of the functional group at C_α for the $\beta\text{-O-4}$ cleavage, the mechanism of this hydrogenolysis by Ru catalysts in the presence of $\text{C}_\alpha\text{-OH}$ groups remains unclear. Our combined experimental and computational results revealed that the presence of $\text{C}_\alpha\text{-OH}$ initiated the dehydrogenation and formation of the keto intermediate ($\text{C}_\alpha=\text{O}$), which is more susceptible to $\beta\text{-O-4}$ bond cleavage into phenol and keto products. In addition, this concept is applicable to the technical lignin and yielded >27 wt.% phenolics.

Our findings advance our understanding of the participation of $\text{C}_\alpha\text{-OH}$ of lignin in hydrogenolysis by Ru/RuO_x without external H_2 . Together with experimental and computational results, we postulated the chemical pathway of hydrogenolysis of $\beta\text{-O-4}$

linkages by Ru/RuO_x/C (**Fig. 6**). The presence of the C_α-OH enabled the dehydrogenation by Ru catalysts into the keto intermediate (C_α=O) and facilitated the β-O-4 bond cleavage without hydrogen-donor solvents and/or external H₂ gas. The use of hydrogen-donor solvents enabled the MPV reduction of the keto product (acetophenone) for subsequent hydrodeoxygenation and hydrogenation. Although the design of catalysts for lignin hydrogenolysis remains a challenge, the mechanistic insights gained from this work could guide (1) the development of the lignin fractionation process to provide the chemical functionality that facilitates the cleavage of β-O-4 bonds of lignin; and (2) the design of solvent systems to control the product distribution.

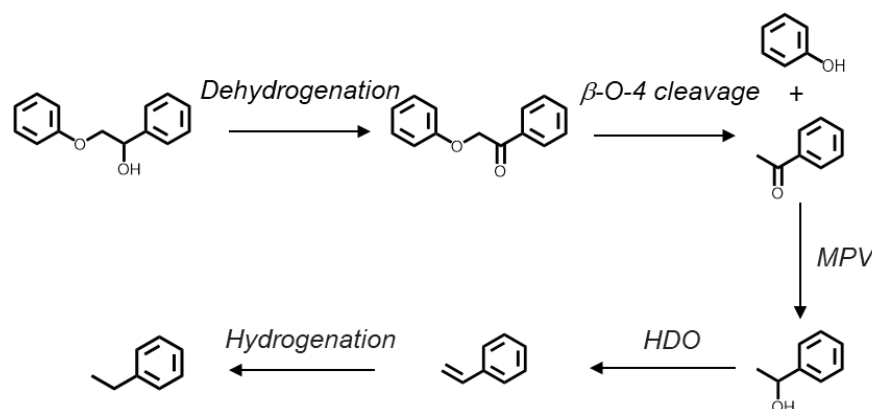


Figure 6. Proposed reaction pathway for conversion of model β-O-4 compounds with C_α-OH group and by Ru/RuO_x/C catalyst

4. Conclusion

Selective hydrogenolysis of lignin is important in the productions of phenolic and aromatic chemicals. We demonstrated the aliphatic hydroxyl groups (C_α-OH) of lignin model compounds were important in hydrogenolysis of β-O-4 linkages by Ru/RuO_x/C. The use of hydrogen donor solvents and external H₂ was not necessary in the C-O cleavage. The presence of the C_α-OH group in the lignin model compounds and technical lignin promoted the charge transfer and formation of stable keto intermediate. The keto intermediate formation facilitated the β-O-4 cleavage into alcohol and keto products. The use of alcoholic solvents initiated MPV of the keto product by RuO_x for subsequent hydrodeoxygenation and hydrogenation. These findings expand our understanding in the

effect of lignin functionality and RuO_x on lignin conversion by Ru/RuO_x/C catalyst. Future studies will use the whole cell wall biomass to bypass the costly lignin fractionation step and catalyst recycling.

Supplementary Information Chapter 4

Unlocking self-hydrogen for hydrogenolysis of lignin by a dual function Ru/RuO_x/C catalyst

Table S1. List of chemicals/reagents used in this study				
Chemical	Supplier	Purity	CAS Number	
2-phenoxy-1-phenylethanol (PPE-OH) for β -O-4 with C $_{\alpha}$ -OH	Ark Pharm Inc., USA	97%	42487-72-3	
2-phenethyl phenyl ether (PPE) for β -O-4	Frinton Laboratories Inc., USA	98-99%	40515-89-7	
Diphenyl ether (DPE) for 4-O-5 bond	Sigma, USA	99%	101-84-8	
Benzyl phenyl ether (BPE) for α -O-4 bond	Sigma, USA	98%	946-80-5	
Veratrylglycerol- β -guaiacyl ether for β -O-4 with C $_{\alpha}$ -OH and methoxy substitution on the ring	AstaTech, Inc., USA	97%	10535-17-8	
Kraft lignin (KL)	Ingevity, USA	-	-	
Yellow poplar steam exploded lignin (YL)	Wolfgang Glasser's lab Virginia Tech, USA	-	-	
Soda lignin (SL, Protobind)	Wolfgang Glasser's lab Virginia Tech, USA	-	-	
Organosolv lignin (OL)	Wolfgang Glasser's lab Virginia Tech, USA	-	-	
Ethanol	VWR, USA	200 proof	64-17-5	
1-propanol	TCI America, USA	>99.5%	71-23-8	
2-propanol	TCI America, USA	>99.5%	67-63-0	

2-butanol	TCI America, USA	>99.0%	
1,4-dioxane	VWR, USA	>99.9%	123-91-1
2-butanone	VWR, USA	>99.5%	78-93-3
Ethyl acetate	VWR, USA	>99.5%	141-78-4
5% Ru/C	Alfa Aesar, USA	N/A	7440-18-8
(pre-reduced) 5% Ru/C (in ~50% water) as a control	Alfa Aesar, USA	N/A	7440-18-8
H ₂ gas	Welder supplies, USA	research grade: 99.999%	-
O ₂ gas	Welder supplies, USA	research grade: 99.998%	-
N ₂ gas	Welder supplies, USA	industrial grade: 99.9995%	-

1.1 Quantum calculation methods

1.1.1 Density functional theory calculations.

All optimized geometries were determined based on periodic density functional theory (DFT) calculations [258] using the Vienna ab initio simulation package Version 5.4.4 (VASP) [259, 260]. The interactions between valence electrons and ion core were presented by projector augmented wave (PAW) potential [261, 262]. The exchange-correlation function, along with the generalized gradient approximation (GGA) by Perdew, Burke, and Ernzerhof (PBE) was used to determine the interaction between valence and core ions [263]. The $5 \times 3 \times 1$ of Monkhorst-Pack grid was used to construct the Brillouin-zone [264]. The geometry optimization was performed within the conjugate gradient method [265], with cut-off energy for the minimization were determined as 400eV. Moreover, the parameters of energy convergence criteria of 1.0×10^{-6} eV/atom and force convergence criteria, lower than 0.05 eV/Å, were applied. We selected the convergence criteria of 1.0×10^{-6} eV/atom for high precision. The added force convergence improved the accuracy of the calculation. The partial occupancies were determined by generating the Methfessel-Paxton scheme[266] with a smearing energy of 0.2 eV. Furthermore, the Van der Waals correction of the D3 method proposed by

Grimme *et al.* [267] was also adopted. Adding Van der Waals correction increased the accuracy of the calculation, which was a critical parameter to describe the bonding in C and H atoms.

The Ru (111) surface was used to represent the Ru catalyst in all calculations because it was the most stable facet of the Ru catalyst [268-270]. The interactions between reactant molecules, PPE and PPE-OH, and Ru (111) surface during the adsorption process were determined via the adsorption energy (E_{ads}) calculated as follows.

$$E_{\text{ads}} = E_{\text{complex}} - (E_{\text{Ru111}} + E_{\text{mol}}) \quad (1)$$

Where E_{complex} is the energy of the optimized adsorbate-adsorbed catalyst surface (the adsorption of PPE and PPE-OH on Ru (111) surface), E_{Ru111} is the energy of the optimized Ru (111) surface, and E_{mol} is the energy of an optimized isolated PPE and PPE-OH molecules under vacuum. A negative E_{ads} value indicated the attractive interaction between the adsorbate and the catalyst surface. Whereas a positive value suggested the desorption reaction. To confirm the interaction between reactant molecules, possible intermediates, and the Ru (111) surface during the hydrogenolysis reaction, the charge distribution and electronics charge density difference during adsorption process were determined by the Bader charge ($\Delta\rho_{\text{Bader}}$) analysis[271-274] described as follows:

$$\Delta\rho_{\text{Bader}} = \rho_{\text{total}} - \rho_{\text{Ru(111)}} - \rho_{\text{mol}} \quad (2)$$

Where ρ_{total} , $\rho_{\text{Ru(111)}}$, and ρ_{mol} are partial charge densities of the adsorbate-adsorbed surface, clean Ru(111) surface, and the isolated adsorbate molecule, respectively.

1.1.2 Model Information

The model information of isolated PPE and PPE-OH molecules was depicted in

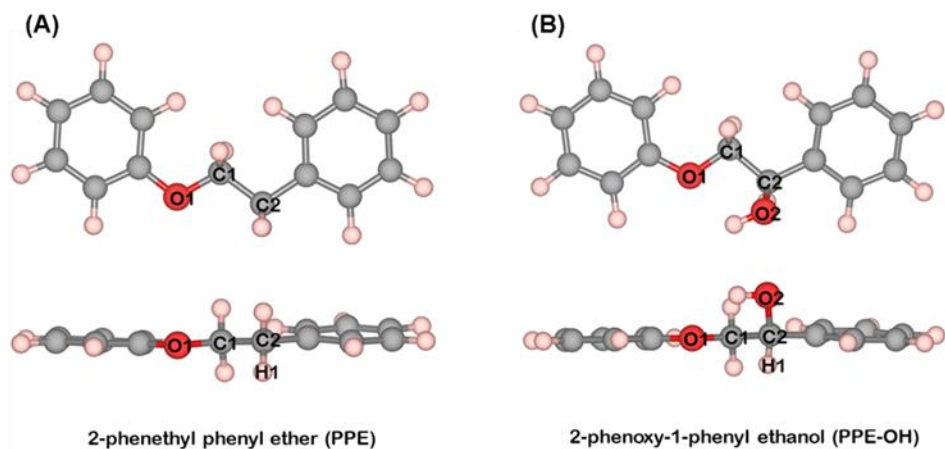


Figure S2. These models were constructed using two benzene rings, which were linked via O1, C1, and C2 atoms. The PPE-OH molecule was constructed by substituting a hydroxyl group (-OH) at the C_α position, which was denoted as C2 in

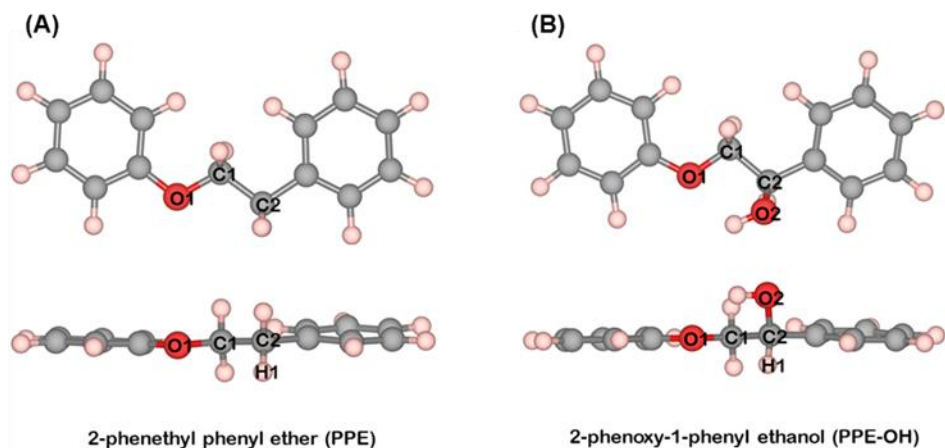


Figure S2B. The important bond distances in this study were O1-C1, C1-C2 and C2-H1, and C2-O2 of PPE and PPE-OH.

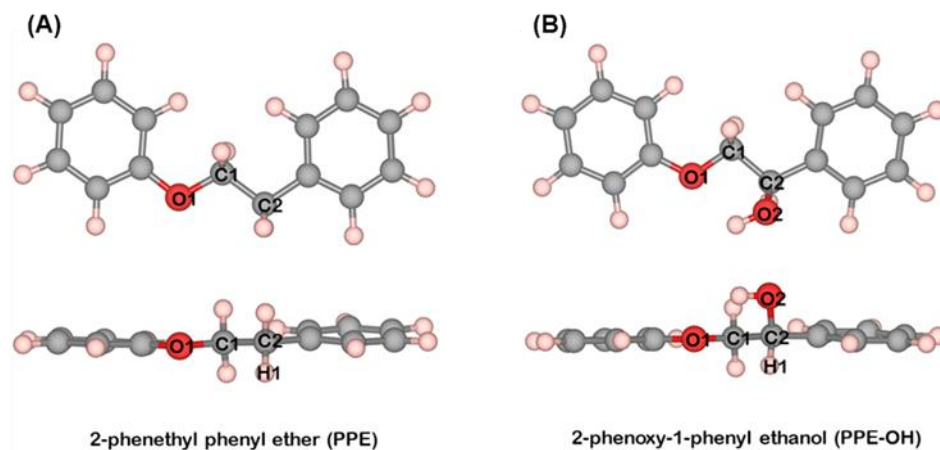


Figure S2. The optimized geometry of the isolated adsorbate molecules, 2-phenethyl phenyl ether (PPE, A) and 2-phenoxy-1-phenyl ethanol (PPE-OH, B)

The 6 x 4 Ru (111) slab model with a dimension of 14.73 x 8.51 x 21.02 Å was built (

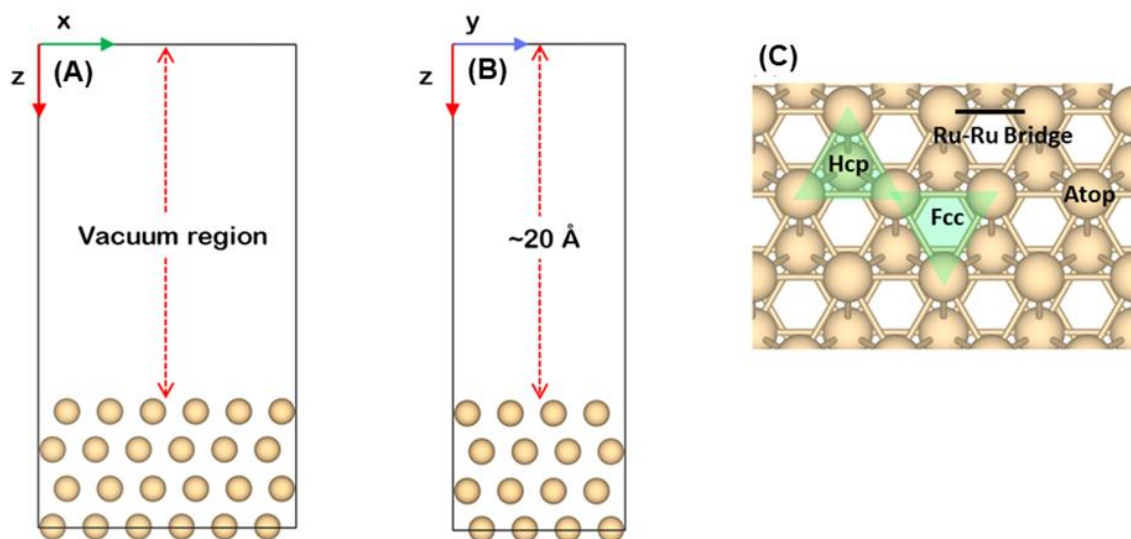


Figure S3). The Ru (111) slab was separated by a 15.00 Å vacuum region along the z-axis to avoid interactions by the periodicity. The most stable adsorption configuration of both PPE and PPE-OH are illustrated in **Fig. S2A and S2B**, respectively. Moreover, the important atomic bond distances of PPE and PPE-OH before and after the adsorption are summarized in **Table S2**. The two bottom layers of the slab were fixed to the bulk lattice parameter. Whereas the two top layers and adsorbed species were allowed to fully relax.

The possible active sites of Ru (111) slab were classified as (1) atop site, (2) bridge site between 2 Ru atoms, (3) three-fold hcp hollow site, and (4) three-fold fcc hollow site (

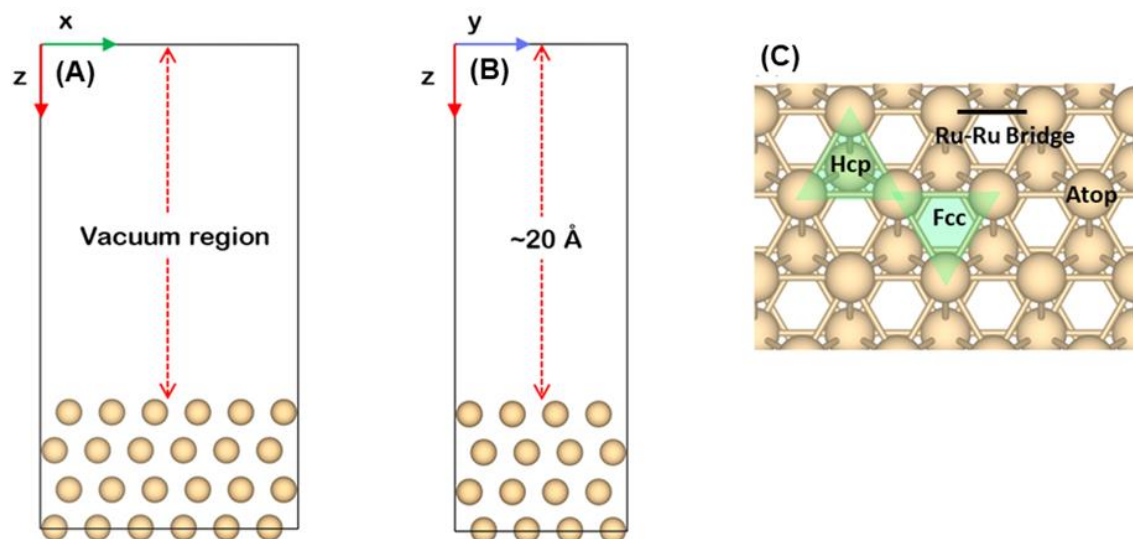


Figure S3C).

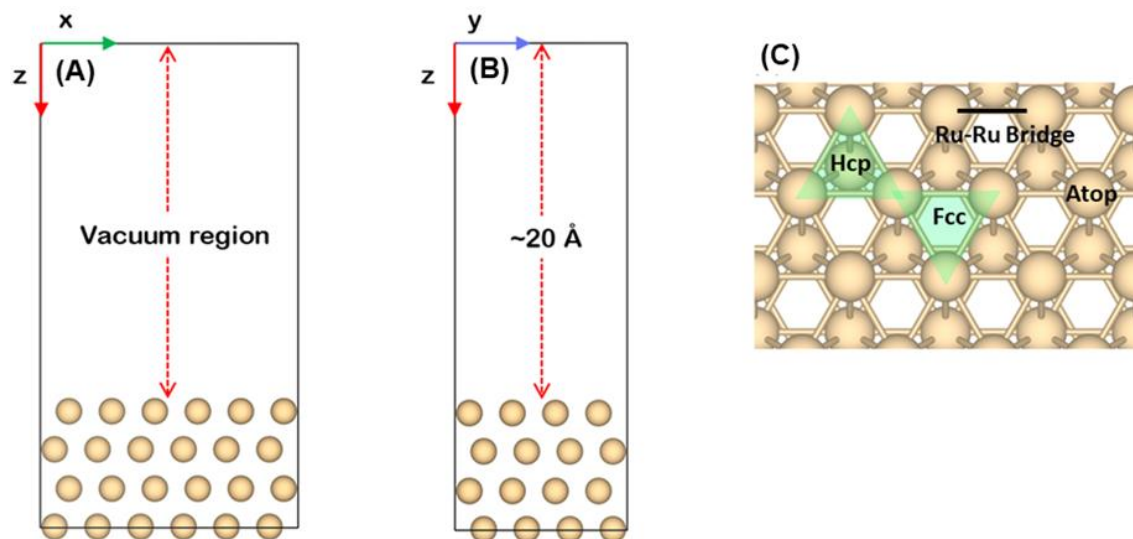


Figure S3. Slab model of Ru(111) surface projected along the (010)-direction (A), (100)-direction (B), and possible active sites on Ru(111) surface (C).

Table S2. Important atomic distances in PPE and PPE-OH molecules before and after adsorption on Ru(111) surface				
Bond	Bond distance (Å)			
	Isolated PPE	Adsorbed PPE	Isolated PPE-OH	Adsorbed PPE-OH
O1-C1	1.43	1.45	1.43	1.44
C1-C2	1.51	1.52	1.52	1.53
C2-H1	1.10	1.10	1.11	1.14
C2-O2	N/A	N/A	1.44	1.44
Nearest adsorption height	N/A	2.18	N/A	2.08

Interactions between reactants and Ru(111) surface

To better understand how the C α -OH facilitated the cleavage of the β -O-4 bond, we performed density functional theory (DFT) calculations to determine the relative stability of the PPE-OH on a model Ru (111) catalyst surface. We used PPE as our control. Our results demonstrated that the PPE and PPE-OH molecules strongly chemisorbed on Ru (111) with an adsorption energy of -4.42 and -4.17 eV, respectively (**Fig. S3**). The PPE and PPE-OH adsorption configuration showed that their two benzene rings are the point of adsorption on the Ru (111) surface. The presence of the C α -OH group in the PPE-OH model increased the steric effect. It weakened the adsorption of PPE-OH on Ru (111) than that of PPE, as evidenced by the extension of the C2-H1 bond in PPE-OH (**Table S2**).

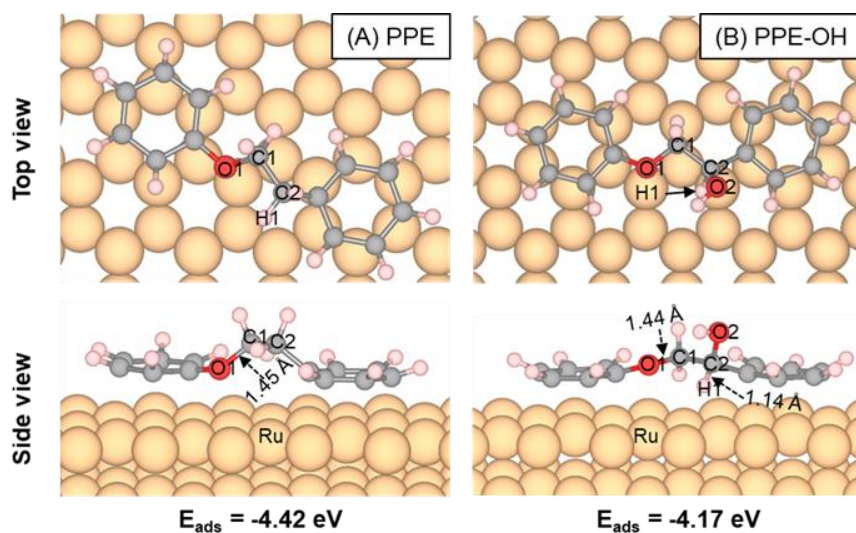


Figure S3. Optimized structures in the top and side view of PPE (A) and PPE-OH (B) adsorbing on the Ru(111) surface with the adsorption energy (E_{ads}).

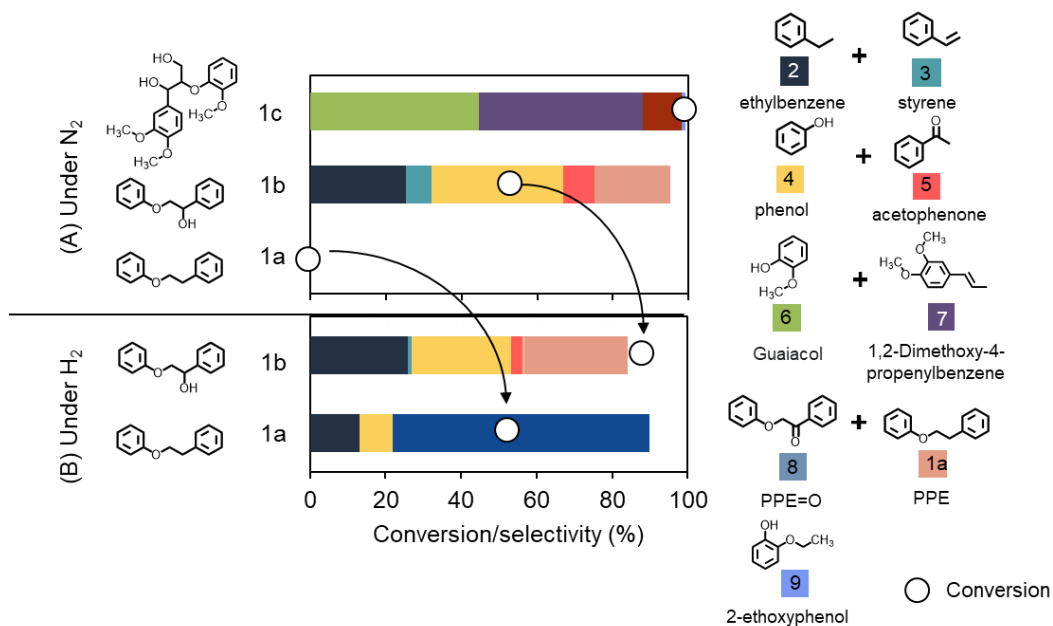


Figure S4. Cleavage of β -O-4 bond of veratrylglycerol- β -guaiacyl ether (1c), 2-phenoxy-1-phenylethanol (1b), and 2-phenyl ethyl phenyl ether (1a) by Ru/RuO_x/C in ethanol under (A) N₂ and (B) H₂. Reaction condition: 280°C, 8 bar H₂ or N₂, 1 wt.% reactant/ethanol, 20 wt.% catalyst loading, 4h.

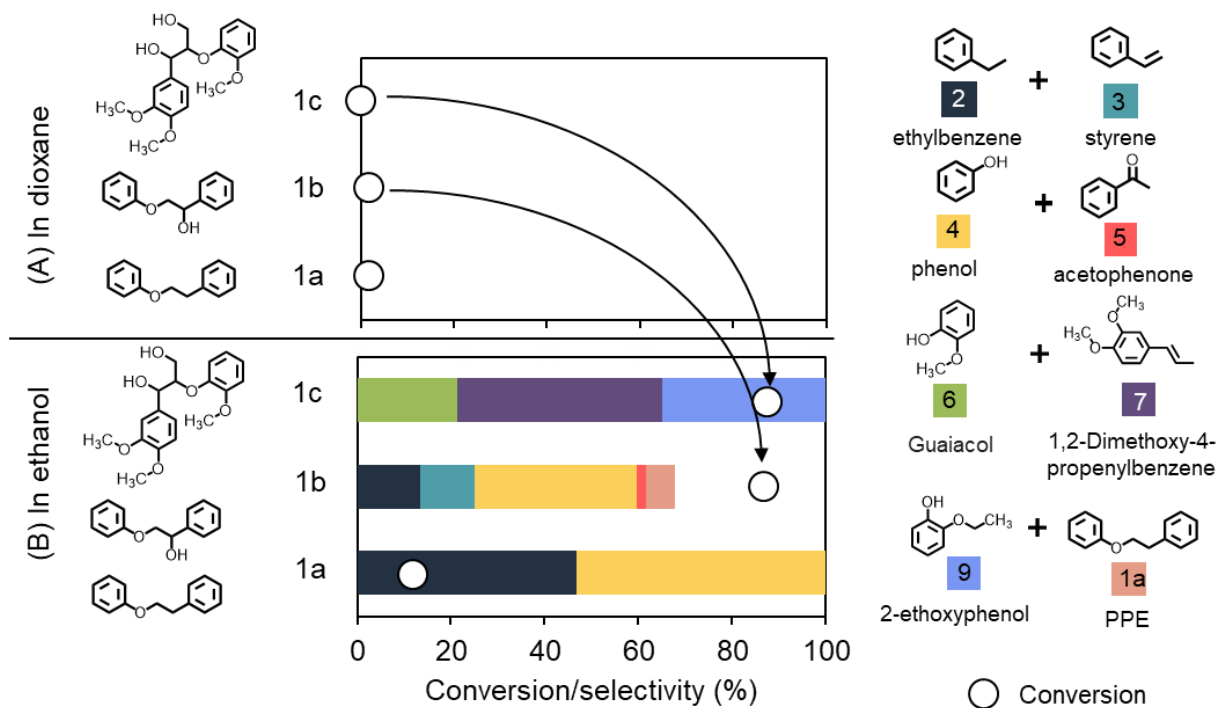


Figure S5. Cleavage of β -O-4 linkages of veratrylglycerol- β -guaiacyl ether (1c), 2-phenoxy-1-phenylethanol (1b), and 2-phenyl ethyl phenyl ether (1a) by bulk RuO_2 in ethanol under N_2 . Reaction condition: 280°C , 8 bar N_2 , 1 wt.% reactant/ethanol, 20 wt.% catalyst loading, 4h.

Bader charge analysis

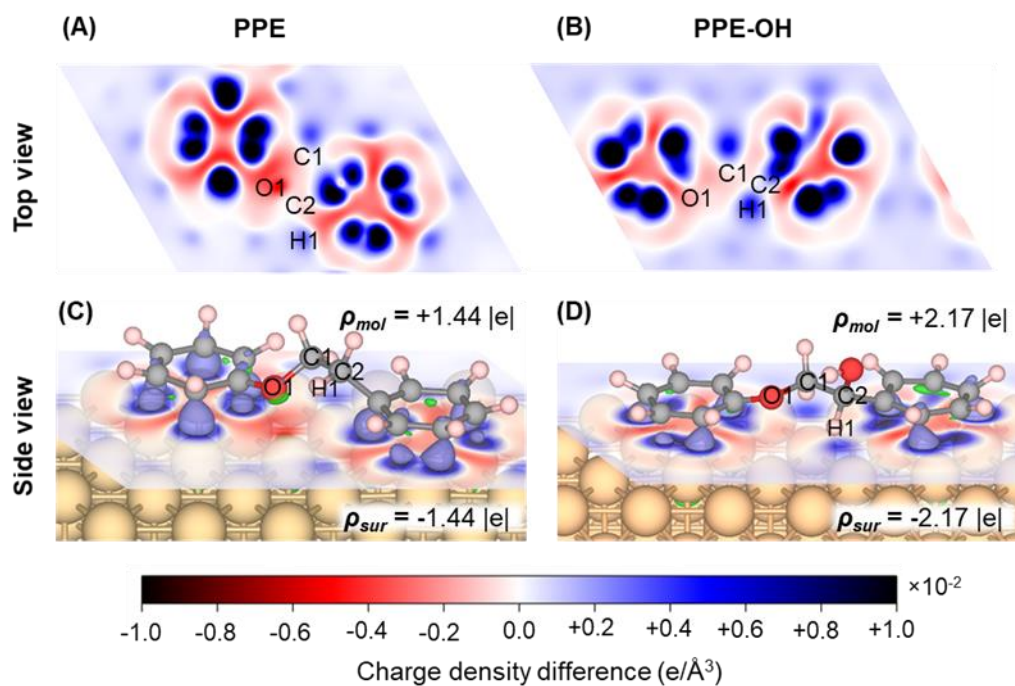


Figure S6. The charge density difference cross-sectional profile at the Ru(111) catalyst surface of (A & C) PPE adsorption in the top and side view and (B & D) PPE-OH adsorption in the top and side view. The iso-value of charge density difference was set to $\pm 0.01|e|$, in which the electron accumulation and depletion are denoted as dark red and dark blue filled contours, respectively. Whereas the neutral zone (no electron transfer) is denoted as a white zone. The ρ_{mol} and ρ_{sur} represent the charge density of the adsorbed molecule and the catalyst surface, respectively. The Bader charge changes values of these atoms are illustrated in **Table S3**.

Table S3. Atomic Bader charge change of essential atoms of adsorbed PPE and PPE-OH on Ru111 surface.

Atom	Bader charge change e	
	Adsorbed PPE	Adsorbed PPE-OH
O1	-0.16	-0.02
C1	-0.12	-0.29
C2	-0.18	-0.14
H1	+0.16	+0.67
O2	N/A	-0.10

Effect of solvents on the hydrogenolysis of PPE-OH.

In aprotic solvents, 1,4-dioxane appeared attractive as a reaction solvent because of the high selectivity of 33% and 21% toward phenol (4) and acetophenone (5), respectively, after 4h (**Fig. 3**). We observed PPE=O (1a) as the reaction product. To evaluate the evolution of PPE-OH, PPE=O, and resulting products, we conducted the hydrogenolysis of PPE-OH in dioxane using Ru/RuO_x/C catalyst at 280°C for 12h. We observed a progressive increase in PPE-OH conversion, which was complete after 12h. The conversion of PPE-OH (1b) and selectivity to β-O-4 cleavage increased over time (**Fig. S7**). PPE=O was rapidly formed as shown by an increase in selectivity of PPE=O and a maximum of 29% at 20% PPE-OH conversion within the first 2h (**Fig. S7**). The selectivity of PPE=O had a volcano-shape, which suggested that PPE=O was an intermediate product. The selectivity of PPE=O dropped with reaction times >2h. This decrease in PPE=O selectivity was accompanied by an increase in HDO selectivity (selectivities of phenol and acetophenone). These results corroborated our computational studies and suggested that PPE=O was the keto intermediate product from dehydrogenation of PPE-OH. Moreover, the selectivity toward the sum of ethylbenzene (2) and styrene (3) was low (i.e., Σ2+3=7%), which suggested that Ru/RuO_x/C in dioxane proceeded with minimal side reactions (hydrodeoxygenation and hydrogenation) compared with protic solvents.

In protic solvents, we did not observe the PPE=O as a product. Moreover, we observed saturated aromatic products in secondary alcohols (2-propanol and 2-butanol). We hypothesized that the absence of PPE=O and the formation of saturated aromatic

products were because protic solvents facilitated the hydrogenolysis and promoted the hydrodeoxygenation and hydrogenation. To test this hypothesis, we selected 2-propanol as our reaction solvent and decreased reaction temperatures (**Fig. S8**). We observed an increase in selectivity of phenol (4) and the sum of ethylbenzene and styrene ($\Sigma 2+3$) with increasing reaction temperature from 230 to 250°C. Whereas the selectivity of PPE=O decreased with increasing reaction temperature. We did not observe PPE=O with a reaction temperature of 280°C. However, we observed the saturated aromatic products. These results suggested that (1) PPE=O was formed in 2-propanol. However, the elevated temperature (>250°C) facilitated the ether cleavage of PPE=O into monomers (**Fig. S8B**). Moreover, an increase in reaction temperature enhanced hydrodeoxygenation and/or hydrogenation of these resulting monomers into saturated phenolic and aromatic products as evidenced by an increase in HDO selectivity (**Fig. S8B**).

Among protic solvents, reactions of PPE-OH with Ru/RuO_x/C in 2-propanol and 2-butanol resulted in a complete conversion of PPE-OH to ethylbenzene (2) and saturated aromatic products, cyclohexane (9), cyclohexene (10), ethyl cyclohexane (11), and cyclohexanol (12). The presence of the saturated aromatic products indicated that hydrogenolysis products underwent hydrodeoxygenation and hydrogenation. The secondary alcohols, 2-propanol and 2-butanol, were more effective hydrogen donors than primary alcohols (ethanol and 1-propanol).[275, 276] Hence, we observed ring saturation products when we used 2-propanol and 2-butanol. To avoid the formation of saturated aromatic products, one should avoid secondary alcohols as reaction solvents.

Together, these results suggested that PPE=O was an intermediate product of the hydrogenolysis of model β -O-4 compounds with the C $_{\alpha}$ -OH group. The results further suggested that the dehydrogenation of PPE-OH (1b) to PPE=O (8) took place under Ru/RuO_x/C in both polar protic and aprotic solvents. Moreover, the cleavage of PPE=O to phenol and acetophenone in dioxane was slower than that in protic solvents.

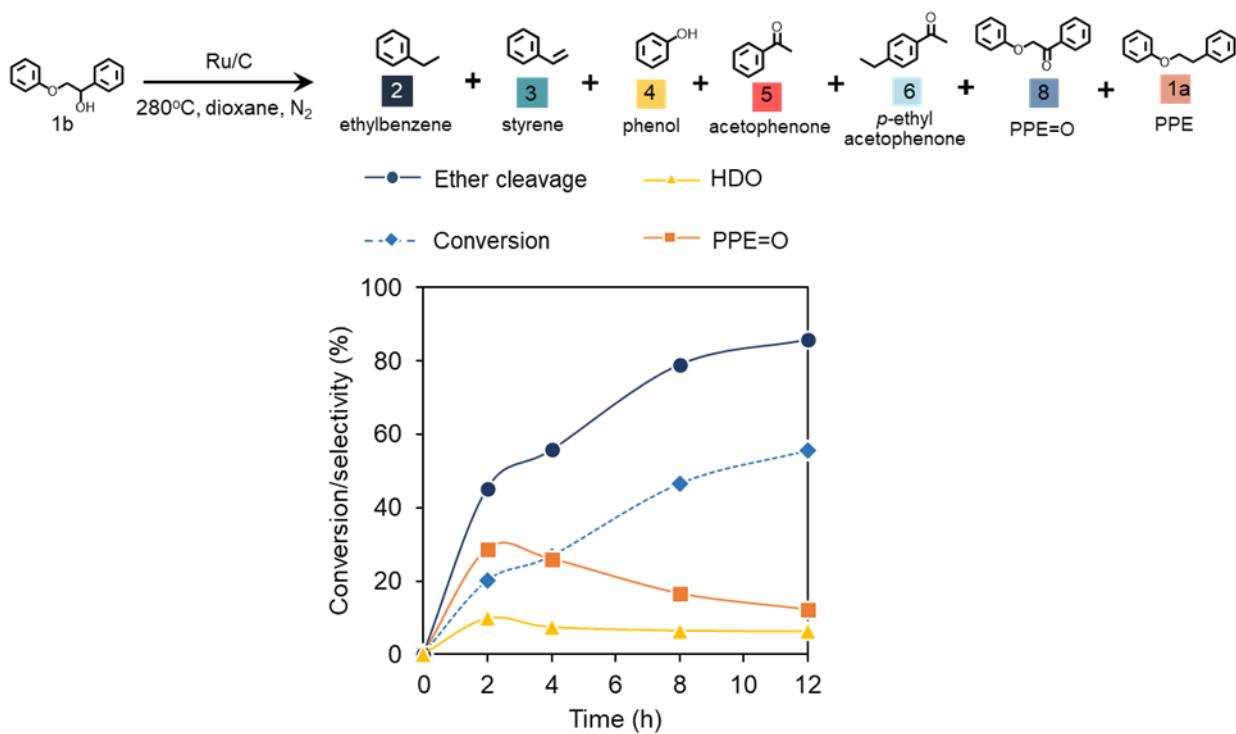


Figure S7. Evolution profiles of reaction products from cleavage of β -O-4 bond of 2-phenoxy-1-phenylethanol (1b) by Ru/RuO_x/C in dioxane. Reaction condition: 280°C, 8 bar N₂, 1 wt.% reactant/dioxane, 20 wt.% catalyst loading, 4 h. HDO selectivity = sum of HDO product (2 and 3) selectivities, Ether cleavage selectivity = sum of ether cleavage product (2, 3, 4, 5, and 6) selectivities.

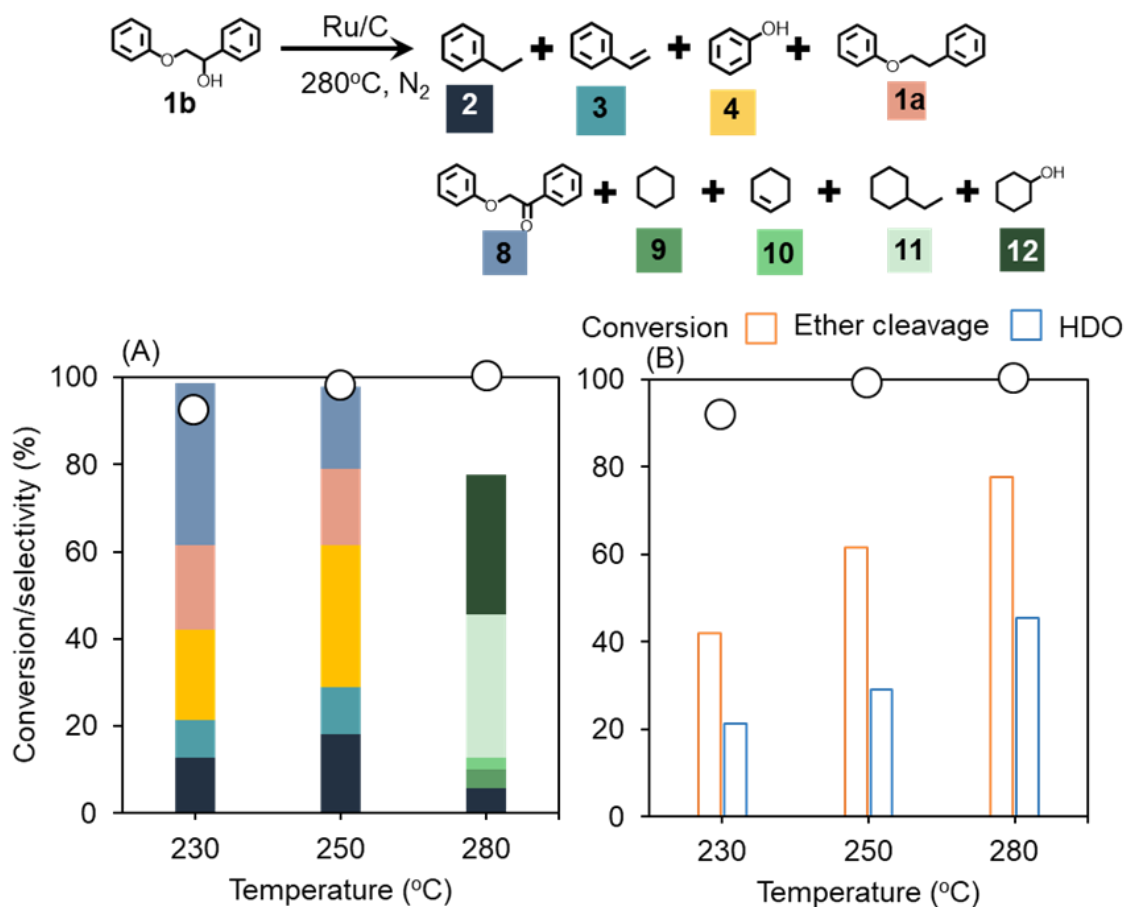


Figure S8. Cleavage of the β -O-4 bond of 2-phenoxy-1-phenylethanol (1b) by Ru/RuO_x/C in 2-propanol (A) and selectivities toward ether cleavage and hydrodeoxygenation products (B). Reaction condition: 8 bar N₂, 1 wt.% 2-phenoxy-1-phenylethanol/2-propanol, 20 wt.% catalyst loading, 2 h. HDO selectivity = sum of HDO product selectivities (2, 3, 9, 10 and 11). Ether cleavage selectivity = sum of ether cleavage product selectivities (2, 3, 4, 9, 10, 11 and 12).

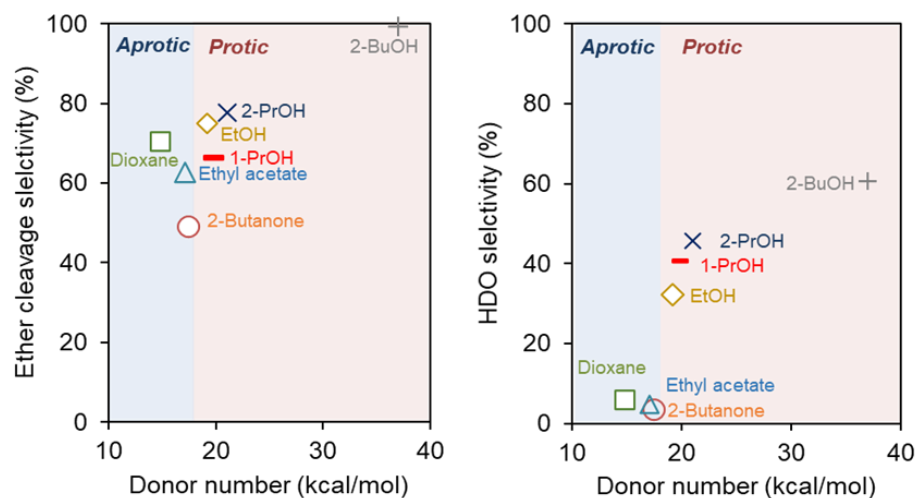
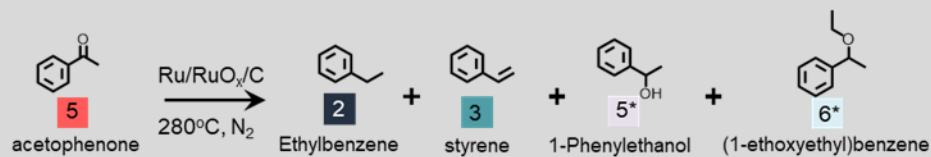


Figure S9. Relationship between donor number and the selectivity toward C-O cleavage and hydrodeoxygenation. HDO selectivity = sum of HDO product selectivities (2, 3, 9, 10, and 11) in **Figure 3**. Ether cleavage selectivity = sum of ether cleavage product selectivities (2, 3, 4, 5, 9, 10, 11 and 12) in **Figure 3**. EtOH = ethanol, 1-PrOH = 1-propanol, 2-PrOH = 2-propanol, 2-BuOH = 2-butanol.

Table S4. Ru and RuO _x content of the used Ru/RuO _x /C catalyst in selected solvents at 280°C for 4h			
Entry	Solvent	Content (wt.%)	
		Ru⁰	RuO_x
1	Fresh (control)	59.0	41.0
2	Dioxane	60.9	39.1
3	Methanol	76.4	23.6
4	Ethanol	78.9	21.1
5	Ethanol (12h)	91.3	8.7
6	2-butanol	84.7	15.3

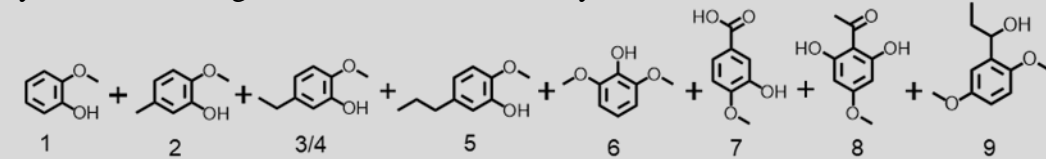
Table S5. Meerwein–Ponndorf–Verley (MPV) reduction of acetophenone and product selectivity over Ru/RuO_x/C catalyst.



Cat	Entry	Time (h)	Conversion (%)	Yield (%)				MPV
				2	3	5*	6*	
Ru/RuO _x /C	Fresh (control)	2	73.1	68.9	3.0	1.2	-	73.2
	Reduced	2	25.5	12.8	1.6	11.1	-	25.5
	Reduced	6	64.3	34.9	0.8	3.9	24.7	39.6

Reaction condition. 280°C, 2 h, 8 bar N₂, 1 wt.% acetophenone/ethanol, 20 wt.% catalyst loading. Catalyst reduction. 0.02g Ru/RuO_x/C catalyst at 12mL ethanol, 280°C under 8 bar N₂, 12h.

Table S6. Hydrogenolysis of the real lignin over Ru/RuO_x/C catalyst

Lignin \longrightarrow 

Time	Entry	Total Yield (wt%)	Yield (wt%)								
			1	2	3	4	5	6	7	8	9
4h	SL	9	1.4	0.6	1.3	2.2	2.8	0.7	-	0.9	1.8
	OL	9.7	1.3	0.6	0.5	0.8	1.7	2.4	1.5	1.6	2.2
	KL	12.2	4.6	2	1.1	2.8	6.8	0.4	-	-	-
	YL	12.5	1.2	0.6	0.1	0.7	2.9	2.1	1.4	1.6	5.3
12h	SL	17.8	3	1.6	2.7	3.8	5.6	1.3	1.6	1.4	3.2
	OL	17.7	2.1	1.3	1.2	1.7	2.9	3.6	2.9	3.1	4.2
	KL	17.7	5.8	3.3	2.2	3.4	7.1	1.4	2.6	-	-
	YL	27.5	2.9	1.7	1.5	0.9	6.2	4.3	3.5	3.5	10.2
24h	SL	18.8	3	2.8	2.8	3.7	5	1.5	1.7	1.8	3.8
	OL	18.4	3.6	2.2	1.6	1.8	3.2	3.4	3.3	2.8	2.9
	KL	24.2	9.5	6.5	2.8	3.5	7.7	2.5	3.5	-	-
	YL	27.9	4.1	3.1	1.3	1.6	6	3.3	3.8	3.6	9.5

Reaction condition: 280°C, 8 bar N₂, 1 wt.% lignin, 20 wt.% catalyst loading. YL =Yellow poplar stem exploded lignin, OL = Organosolv lignin, KL =Kraft lignin, PL= Soda lignin

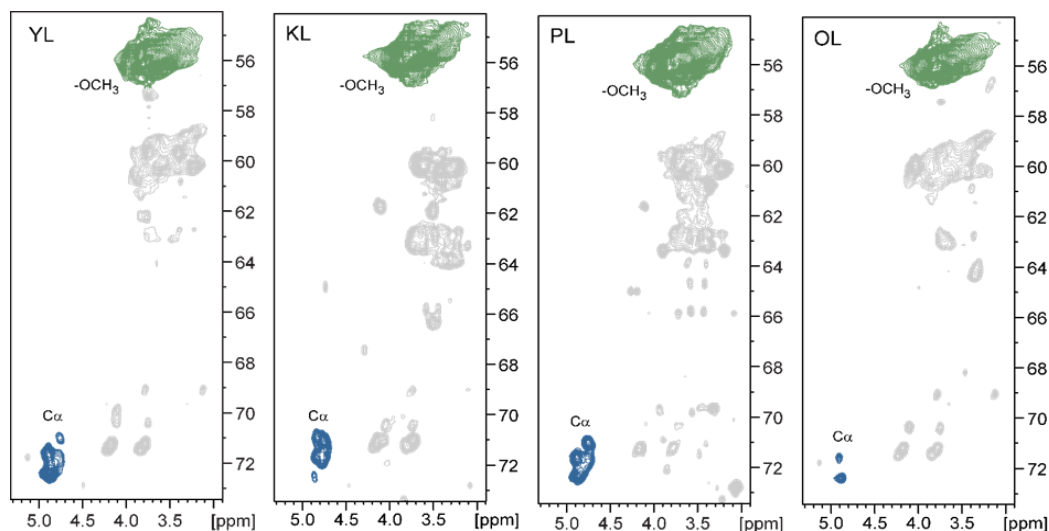


Figure S10. Portions of the HSQC NMR spectra for the technical lignin showed the C_α-OH contours and the C_α=O contours relative to the methoxy (OCH₃) contours. These contours were used to determine the relative integrals in **Table S7**.

Table S7. Relative integrals of the C _α -OH and C _α =O peaks in four technical lignin					
Sample	S (wt.%) ^a	Chemical shift region (ppm)	C _α -OH ^b	C _α =O ^b	Total HSQC integral ^b
Yellow poplar lignin (YL)	<0.2	(¹ H) 5.04-4.64 (¹³ C) 72.9-70.7	0.0302	0.0182	0.0484
Kraft lignin (KL)	0.9	(¹ H) 4.99-4.65 (¹³ C) 72.7-70.5	0.0242	0.0178	0.0420
Soda lignin (SL)	0.3	(¹ H) 4.99-4.67 (¹³ C) 72.7-70.7	0.0197	0.0216	0.0413
Organosolv lignin (OL)	0.2	(¹ H) 5.02-4.73 (¹³ C) 72.7-70.7	0.0038	0.0111	0.0149

^ameasured by combustion techniques for CHNS, ^brelative integral area to the methoxy contour

CHAPTER 5

METAL-ORGANIC FRAMEWORK SEPARATOR AS POLYSELENIDE FILTER FOR HIGH-PERFORMANCE LITHIUM-SELENIUM BATTERIES ³

1. Introduction

The great demand for electric vehicles and power-grid energy storage has stimulated the search for high-capacity rechargeable batteries. For decades, conventional lithium-ion batteries have been used for electronic devices. However, current transition metal oxide cathodes⁴ have low theoretical energy density (~350-450 mAh/g) [277], which prevents their practical application such as in electric vehicles [278]. Thus, chalcogenide-containing cathodes, such as S, Se, and Te, have gained attention [279-282]. Selenium is viewed as potential electrode material in lithium-selenium cells because selenium has a high theoretical capacity (678 mAh/g) [283] and a volumetric capacity comparable to lithium-sulfur batteries (3268 mAh/cm³ for selenium and 3467 mAh/cm³ for sulfur) [284-287]. Moreover, selenium has a high electrical conductivity of 1×10^{-3} S/cm,[288-290] compared with sulfur (5×10^{-28} S/cm) [291]; the high conductivity provides selenium with better electrochemical properties. However, the performance of lithium-selenium batteries is impaired by the shuttling of soluble polyselenide (Se_x^{2-} , $4 \leq x \leq 8$)[289, 292] across the separator; the polyselenides react with the lithium metal electrode, which causes capacity fade.

³ This chapter is published in ACS Applied Energy Materials (Hossain et al., 2021, ACS Appl. Energy Mater., 4, 12, 13450-13460

⁴ During discharge these materials act as a cathode. We refer to the positive electrodes as cathodes.

Moreover, uncontrolled diffusion of electrolyte anions, typically bis(trifluoromethanesulfonyl)imide (TFSI⁻), causes a nonuniform Li⁺ deposition on the Li anode and promotes Li dendrite formation. These issues hinder the development and practical use of lithium-selenium batteries. The ability to prevent the shuttle effect of polyselenides and diffusion of anions will boost the electrochemical performance and life of the lithium-selenium cells.

The separator provides the path for transporting cations, anions, and an electrolyte between electrodes. Porous polypropylene has been used widely as a separator, a key component of lithium-selenium cells. However, the weak interaction between carbon-carbon backbones of the polypropylene separator with polyselenides and TFSI anions results in the diffusion of polyselenides between electrodes, active material loss, self-discharge, and capacity fade.[293-296] Modifying the separator to prevent polyselenides and anion diffusion is expected to tackle this problem.

Metal-organic frameworks (MOFs) are a class of porous solids with uniform pore structure and coordinated unsaturated sites. MOFs have narrow pore widths and interconnected pores that enable the diffusion of Li⁺ and function as a physical barrier to larger ions in an electrolyte. Moreover, MOFs have coordinated unsaturated sites (Lewis acid characteristics) that can capture Lewis bases, such as polyselenides [297] and TFSI anions [298]. Among various MOFs, PCN-250 (also known as MIL-127 and Fe-soc-MOF [299]) is a class of MOFs constructed from trinuclear iron oxo clusters (Fe₃-μ³-oxo clusters) and tetratopic azobenzene-based linkers (3,3',5,5'-azobenzene tetracarboxylate) (**Fig. S1**).[300] PCN-250 has a small pore width of 5.9 Å [301] and high surface area ~1500 m²/g. This MOF is robust and stable in solutions with pH 1 to pH 12 [302, 303]. These characteristics make PCN-250 a good candidate as a separator modifier.

Here, we fabricated a modified separator using PCN-250 and assessed its ability to suppress the diffusion of polyselenides and TFSI anions in lithium-selenium batteries. We constructed the Se cathode by encapsulating the Se in activated carbon. We chose this

cathode system because it has visible selenium cathode dissolution,[304] which enabled our study on the interaction of the PCN separator with polyselenides. We found that the PCN-modified separator inhibited the diffusion of polyselenides and TFSI anions from cathode to anode. As a result, the lithium-selenium cells were cycled at C/5 and 1C for 500 cycles with high-capacity retention.

2. Experimental Section

2.1. Materials

All reagents were used as received. Their manufacturers, purity, and CAS numbers are shown in **Table S1**. PCN-250 metal-organic frameworks (MOFs) were provided by framergy, Inc (College Station, TX, USA) and produced under the commercial name AYRSORB™ F250. The physicochemical properties of PCN-250 are shown in the *Supporting Information*.

2.2. Synthesis of selenium encapsulated activated carbon cathode (Se@AC).

Selenium was loaded into activated carbon by a facial melt diffusion method to form Se@AC.[305] In short, dry activated carbon and selenium at 2:3 by weight were ball-milled at 300 rpm in acetone for 1 h. After ball milling, the selenium and activated carbon mixture was dried at 80°C for 6 h to remove the acetone. The dry selenium-activated carbon mixture was heated under N₂ at 10°C/min and held isothermally to 260°C for 20h. Finally, the sample was heated to 350°C for 3h to remove physisorbed selenium and cooled to ambient temperature. The selenium loading in Se@AC was ~47 wt.%, measured by thermogravimetric analysis (**Fig. S2**).

2.3. Characterization of metal-organic frameworks

Powder X-ray diffraction (pXRD) analysis of MOF samples was performed on a Bruker D8 Discover diffractometer (Billerica, MA, USA) using CuK_α radiation in the 2θ range from 10° to 40° with 0.5 sec/step. The N₂ adsorption/desorption was measured by a

Micromeritics Tristar (Norcross, GA, USA) instrument to calculate MOF surface area and pore volume. Before the measurement, the sample was treated at 150 °C for 4 h with a Micromeritics FlowPrep with sample degasser (Norcross, GA, USA). The surface area, S_{BET} , was determined from N_2 isotherms using the Brunauer–Emmett–Teller equation (BET) based on the MOF overall mass. The pore size distribution of the PCN-250 MOF was calculated from the desorption isotherm by Nonlocal Density Functional Theory (NLDFT) model. Morphology and elemental mapping analyses of the interface between PCN-250 layer and polypropylene were investigated by scanning electron microscopy (Tescan Vega V3 SEM) with energy dispersive X-ray spectrometry (EDS).

Infrared spectra of the PCN-250 MOFs were recorded on a JASCO Fourier transform infrared (FTIR) spectrometer (Easton, MD, USA), equipped with an attenuated total reflection stage (ATR). Samples were scanned in the spectral range between 400 and 4000 cm^{-1} at a 4 cm^{-1} resolution. Diffuse reflectance infrared Fourier transform spectroscopy (DRIFTS) with adsorbed pyridine was performed to characterize acid sites; measurements were made with a JASCO FTIR equipped with high-temperature DiffuseIR™ cell (PIKE Technology, WI, USA). We chose pyridine as an *in-situ* titrant for probing the Lewis acid site density of MOFs because of earlier success in observation of Lewis acid sites in other MOFs [306-308]. The protocol for the DRIFTS experiments with temperature program desorption is described elsewhere with a slight modification.[309, 310] In short, MOF samples (~5 mg) were placed in a cylindrical alumina crucible and treated in nitrogen gas (50 mL/min) at 50-250°C for 30 min unless otherwise noted. After the treatment, the DRIFTS spectra of MOF catalysts were recorded as the background spectra. The MOF materials were then saturated with pyridine vapor. The adsorbed pyridine was removed by flushing with N_2 gas at 50, 100, 150, or 250°C for 30 min before recording the DRIFTS spectra. All spectra were recorded with 256 scans between 4000–400 cm^{-1} at a 4 cm^{-1} resolution.

XPS spectra were measured using a VG Scientific MultiLab 3000 ultra-high vacuum surface analysis system, equipped with a dual-anode Mg/Al x-ray source and a CLAM4 hemispherical electron energy analyzer. The measurements were performed at the

base pressure of 10^{-9} Torr range using a non-monochromatized Al K_{α} x-ray radiation ($h\nu = 1486.6$ eV). The C-C peak of adventitious carbon at 284.8eV was used for the binding energy (BE) calibration.

2.4. Fabrication of PCN-250 coated separators

Throughout this manuscript, we refer to the PCN-250 coated separator as a PCN separator. The PCN-250 particles (average particle size 20.2 μm with SEM imagery; see Supporting Information, **Fig. S4**) were dried at 150°C under 70cc/min N_2 flow overnight to remove moisture before using. The PCN separators were fabricated by layering PCN-250 and PVDF-HFP binder. In short, ~ 0.03 g dry PCN-250 (0.1 wt.%) was dispersed in ethanol and sonicated for one hour to disperse PCN. The PCN solution (10 mL) was filtered through a conventional polypropylene 2400 membrane. Next, the pump was turned off to allow the PCN to distribute on the polypropylene membrane. Then, 0.5 mL PVDF-HFP in acetone (5 wt.%) was filtered on top of the PCN layer to bind the PCN particles. The PCN and PVDF-HFP solutions were filtered alternately three times to ensure even distribution of the PCN-250 particles on the polypropylene membrane. Before use, the resulting PCN separator was dried at 80°C for 12 h in a vacuum oven.

2.5. Lithium-selenium cell (Li/Se cell) assembly

The cathode materials were prepared by making a slurry of Se@AC, PTFE binder, and carbon black (Super P) at 80:10:10 ratio (w/w/w), unless otherwise noted. The Se loading was $\sim 1\text{-}1.5$ mg/cm^2 [305, 311-313], similar to previous studies, to minimize the effect of volume expansion and contraction during charge/discharge that might affect the electrochemical performance. The slurry was coated onto the current collector and dried at 120 °C for 3 h in a vacuum oven to form the working electrode. The CR2032-type coin cells were assembled in an argon-filled glove box with moisture and oxygen content below 1 ppm. In all experiments, ~ 25 μl of 1M LiTFSI in 1:1 dimethoxyethane (DME): 1,3-dioxolane (DOL) (v/v) were used as the electrolyte, unless otherwise noted. In addition, LiNO_3 (1 wt.%) was used as an additive to aid in the formation of the solid electrolyte interface at the lithium-metal anode. The anode was prepared by directly pressing lithium metal foils onto a 15.8 mm diameter stainless steel disc. The PCN separator was cut into

18 mm discs and placed in the cells. The conventional polypropylene separator was used as a control.

2.6. Permeation tests

Permeation tests were conducted in a Li/Se full cell in the H-type cell configuration. Two chambers of the cell were separated by polypropylene or PCN separator. The Se cathode was prepared using 8 mg Se@AC, 1 mg PTFE binder, and 1 mg Super P mixture on a 1x2 cm stainless steel mesh. The selenium loading of the cathode was $\sim 2 \text{ mg/cm}^2$, slightly higher than that in the CR2032 cells to ensure the visible formation of the polyselenides. The 0.2C (based on theoretical capacity) current rate was applied to discharge the cell at 30°C. To investigate the formation of soluble polyselenides and their diffusion through the separator, images were captured during 48h.

2.7. Open circuit voltage (OCV)

The open-circuit voltage of the cell was measured with a Bio-Logic SP-200 potentiostat/galvanostat using a Li/Se cell. The Li metal was used as both reference electrode and anode. The Se cathode consisted of Se@AC, PTFE binder, carbon black (Super P) at 80:10:10 ratio (w/w/w). The OCV of the cell was recorded at 30°C for 12h.

2.8. Cyclic voltammetry

Cyclic voltammetry (CV) was performed by Autolab® using Li/Se cell. The cyclic voltammetry was conducted between 0.5-3.0 V at a scan rate of 0.1mV/s. Then scan rate was varied from 0.1 to 0.2, 0.7, and 1.0 mV/s to determine the lithium-ion diffusion coefficient (D_{Li^+}) by the Randles–Sevcik equation (eq. (1)) [314].

$$I_p = 2.69 \times 10^5 \cdot n^{1.5} A \cdot C_{\text{Li}} \cdot D_{\text{Li}^+}^{0.5} \cdot v^{0.5} \quad (1)$$

where I_p is the peak current (Amps), n is the number of electrons transferred in the redox event, C_{Li} is denoted as concentration (mol/cm^3), A represents the area of the electrode (cm^2), and v represents scan rate (V/s).

2.9. Li-ion transference number (t_{Li^+})

Li^+ transference number is defined as a fraction of the overall charge transferred by species containing Li^+ . [315] CR2032-type coin cells using Li/Li symmetric cell configuration were assembled in an argon-filled glovebox. The cells were left in open-circuit condition for at least 12h to equilibrate prior to measurement. The DC polarization method was applied, and the t_{Li^+} was calculated based on the Bruce-Vincent method by eq. (2) [316]:

$$t_{Li^+} = \frac{I_{ss}(\Delta V - I_0 R_0)}{I_0(\Delta V - I_{ss} R_{ss})} \quad (2)$$

where I_0 and I_{ss} represented the initial and steady-state current, respectively. The values of R_0 and R_{ss} were calculated from EIS measurements before and after perturbation at $\Delta V = 10$ mV.

Li^+ transference numbers close to 1 are indicative of low anion motion and are conducive to cell operation without the development of excessive concentration gradients, a condition that increases the efficiency of the cell.[317]

2.10. Galvanostatic lithium cycling performance

Galvanostatic cycling experiments were conducted using symmetric Li/Li cells with 1M LiTFSI in 1:1 DME:DOL (v/v) to evaluate the lithium plating/stripping behaviors using PCN separator. The experiments were performed at 30°C, 1mA/cm² current density, and 30 min plating/stripping interval. Cells with the polypropylene separator were used as a control.

2.11. Electrochemical performance

Galvanostatic charge/discharge tests were performed at C/10 for 50 cycles and C/5 and 1C for 500 cycles using the Arbin BT2000 battery testing unit (College Station, TX, USA) in a voltage window of 1.0–3.0 V *versus* Li/Li⁺ to determine the cycling stability of the Li/Se cells. The current rate was calculated based on the weight of selenium (1C = ~675 mA/g theoretical capacity). Before electrochemical testing, the cells were treated with 10

cycles of galvanostatic charge/discharge at a low rate of C/5 for activation. Coulombic efficiency and capacity retention of the cell after cycling were calculated as follows (eq (3)-(5)):

$$\text{Coulombic Efficiency (CE)} = \frac{\text{Charge capacity}}{\text{Discharge capacity}} \times 100 \quad (3)$$

$$\text{Capacity retention (\%)} = \frac{\text{Final capacity}}{\text{Initial capacity}} \times 100 \quad (4)$$

$$\text{Capacity decay rate (\%/cycle)} = \frac{\text{Initial capacity} - \text{Final capacity}}{\text{Initial capacity} \times \text{cycle number}} \times 100 \quad (5)$$

3. Results

We first fabricated the PCN-250-modified separator and evaluated its ability to prevent self-discharge from the diffusion of polyselenides. Then we assessed the electrochemical performance and cycle time of lithium-selenium cells with a PCN-250-modified separator (PCN separator).

3.1. Lewis acid characteristics of PCN-250 and morphology of PCN separator

To determine the Lewis acid character of PCN-250, we performed Diffuse Reflectance Infrared Fourier Transform Spectroscopy (DRIFTS) with adsorbed pyridine at 50-250°C (**Fig. 1B**). The blank experiments (without pyridine adsorption) did not show any features between 1000-1100 cm⁻¹. The peaks at 1012, 1043, 1070 cm⁻¹ indicated the presence of Lewis acid sites. Moreover, the presence of these peaks at elevated temperature (250°C) suggested a high strength of the Lewis acid sites of PCN-250. To evaluate the Lewis acid-Lewis base interaction between PCN-250 and TFSI⁻, we performed the FTIR on the PCN-250 soaked with solvent (1:1 DME: DOL (v/v)) and electrolyte (1M LiTFSI in 1:1 DME: DOL (v/v)) (**Fig. 1C**). As a control, the FTIR spectrum of the LiTFSI showed unique characteristic peaks of TFSI⁻ at 570, 750, 1051, 1085, 1150, 1192, 1335, and 1364 cm⁻¹ (**Fig. 1C, Table S2**).^[318] Next, we soaked PCN-250 materials in the electrolyte for 30 min and washed them with 1:1 DME:DOL (v/v) solvent to remove physisorbed species. We still observed the peaks of TFSI⁻ at 750, 1051, and 1192 cm⁻¹ that suggested a strong interaction between Lewis acid-Lewis base.

We then used the resulting PCN-250 to fabricate the MOF separator (**Fig. 1A**). The MOF separator was flexible, and the thickness of the MOF layer was $\sim 30\ \mu\text{m}$. Elemental mapping of the PCN separator showed a uniform dispersion of $\text{Fe}_3\text{-}\mu^3\text{-oxo}$ clusters (**Figs. 1E & 1G**). In addition, the FTIR spectrum of the PCN separator had characteristics of PCN-250 (**Fig. S5**).

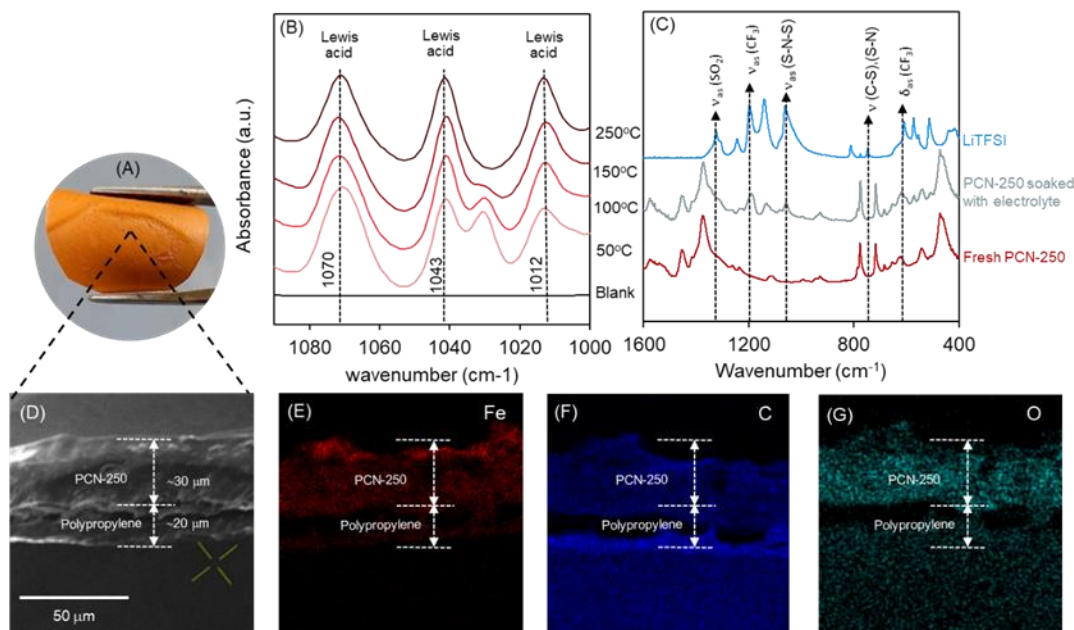


Figure 1. Illustration of flexible MOF separator (A). DRIFT spectra of PCN-250 with pyridine as a probe molecule (B). FTIR spectra of the PCN-250 soaked in electrolytes (C) and SEM micrographs of the cross-sectional area of the MOF separator (D) and their elemental mapping (E-G).

3.2. PCN separator prevented polyselenide permeation

To assess the interaction between PCN separator and polyselenides, we performed *in-situ* permeation measurements in the H-type cell during 48 h at C/5. The H-type cell consisted of a Li/Se cell with the PCN separator (**Fig. 2B**). As a control, both sides of the cell with polypropylene separator were clear initially. After discharge, a light brown color formed on the cathode side (right), indicating the formation of lithium polyselenides. During prolonged discharging, the dissolved polyselenides were concentrated, as shown by the solution's darker color on the cathode side. Moreover, we observed the light brown

color on the anode side, which suggested diffusion of the soluble long-chain polyselenides to the anode side. In the case of the PCN separator, although we observed the formation of soluble polyselenides on the cathode side, they did not diffuse to the anode side. Thus, the PCN separator suppressed the diffusion of the soluble polyselenides.

3.3. PCN separator prevents self-discharge process

One of the major challenges in the practical use of Li-Se batteries is its self-discharge caused by the diffusion of polyselenides. To determine the ability of the PCN separator to prevent self-discharging, we evaluated the open-circuit voltage (OCV) behavior of Li/Se cells with PCN separator during 12h (**Fig. 2C**). When we used polypropylene as a control, the open circuit potential continually decreased and reached 2.72V after 12h. This continual decrease in open-circuit voltage occurred because of the diffusion of soluble polyselenides and reaction with lithium anode. When we used the PCN separator, the open circuit potential dropped slightly and was maintained at 2.91V after 2h. These results suggested the suppression of polyselenides diffusion by PCN separator. These OCV results corroborated the permeation test (**Fig. 2B**).

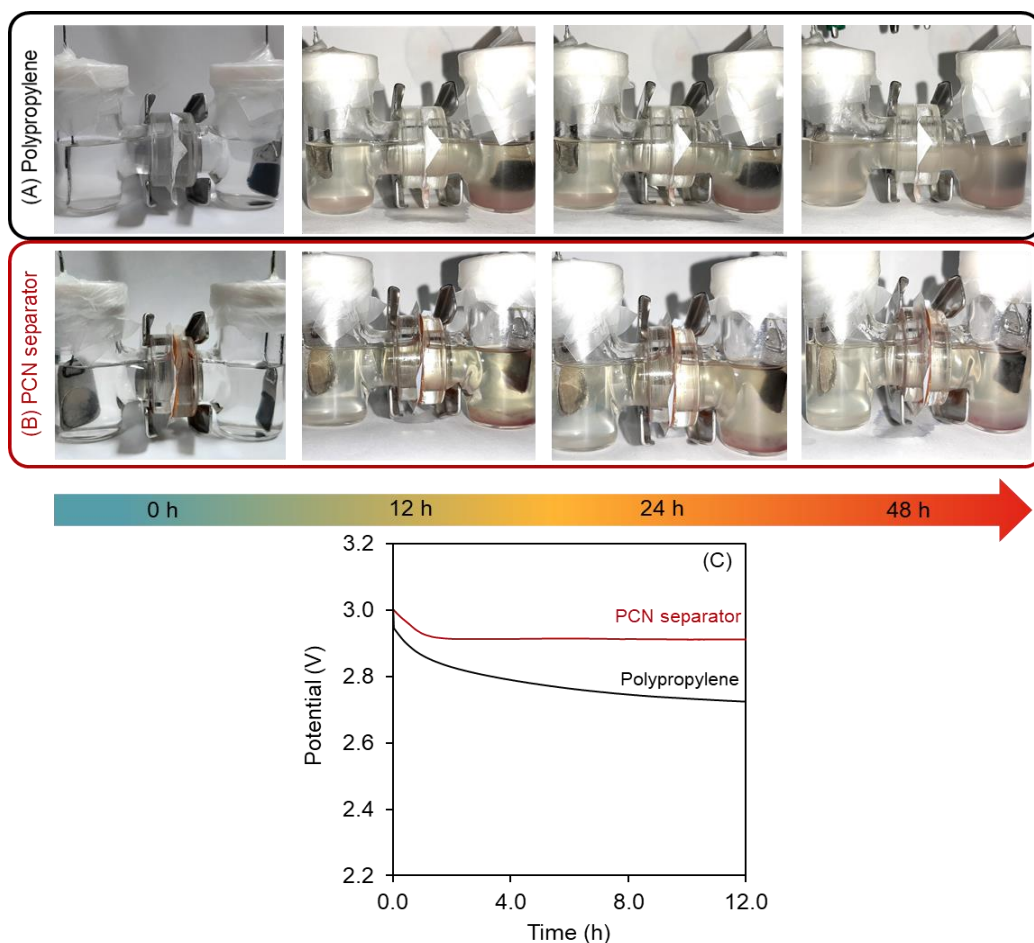


Figure 2. Permeation tests of polypropylene (A), PCN (B) separators over 48h in the H-type cells and Open-circuit voltage (OCV) retention profiles over 12 h relaxation (C).

3.4. PCN separator as an anionic sieve to enhance the Li^+ plating/stripping stability

To assess the relative Li^+ transport in the cell with the PCN separator, we performed Li^+ transference number measurements. As a control, the Li^+ transference number of the cell with the polypropylene separator was 0.38 (Fig. 3A), similar to reported values.[319-321] The cell with the PCN separator yielded a Li^+ transference number of 0.72, much higher than that of the cell with the polypropylene separator. This substantial increase in Li^+ transference number indicated the facile and selective transit of Li^+ through the PCN separator. Moreover, these results also implied that the PCN separator prevented the diffusion of TFSI anions to the anode side, in contrast to the property of the polypropylene

separator. These results further explained the presence of TFSI⁻ peaks after soaking PCN-250 with the electrolyte (**Fig. 1C**).

Figure 3B shows the Nyquist plots of the impedance experiment before and after polarization. We fitted the Nyquist plots with the equivalent circuit and obtained the charge transfer resistance (R_2) and Warburg resistance (W_2 , **Table S3**). The R_2 of the fresh cell (initial) with the polypropylene separator was 332 Ω , which agreed with reported values [322, 323]. The R_2 of the PCN separator was lower than the R_2 with the polypropylene separator, which suggested that the PCN layer improved the electrochemical reaction kinetics [323, 324]. After polarization, we observed an increase in the R_2 of the cell with both separators, which indicated the decomposition of the Li-metal [322, 325]. Another significant finding from the impedance spectra was the W_2 , which explained the formation of the solid electrolyte interface due to the decomposition of solvent and TFSI anion on the Li surface [322, 325, 326]. For the cell with the PCN separator, the W_2 was much lower than the W_2 with the polypropylene separator (**Fig. 3B**). One reason for this difference was that the PCN separator restricted the diffusion of the TFSI anion to the Li-metal. As a result, the formed solid electrolyte interface layer in the cell with PCN separator was thinner than the polypropylene separator.

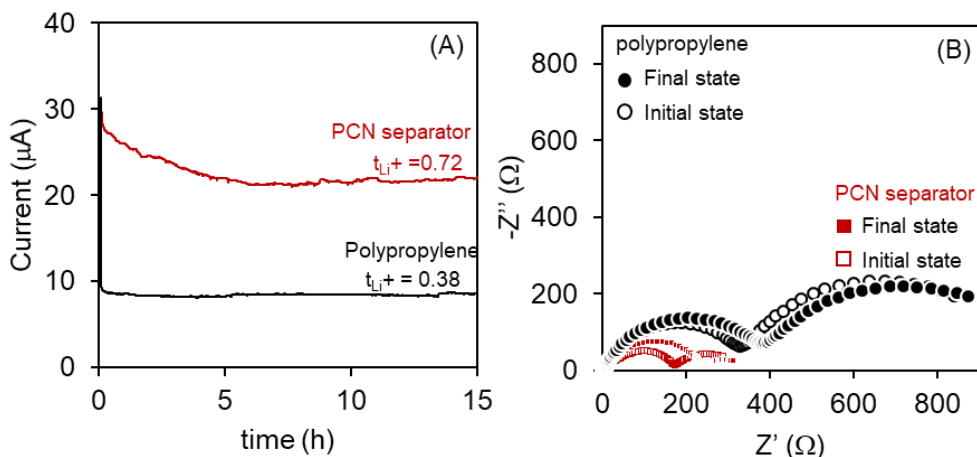


Figure 3. Changes of current with time during polarization of a Li/Li symmetric cell with PCN and polypropylene separators in the fresh electrolyte during 15h at 30 $^{\circ}\text{C}$ under 10mV potential (A) and Nyquist plots of the impedance spectra before and after polarization (B).

To determine whether the PCN separator enhanced lithium cycling stability, we performed galvanostatic cycling experiments using symmetric Li/Li cells containing 1M LiTFSI in 1:1 DME: DOL (v/v) with PCN separator. The voltage profile of the lithium metal working electrode (WE) during constant current lithium plating and stripping at 1 mA/cm² for 500h is presented in **Fig. 4A**. The positive potentials of the lithium WE against the Li/Li⁺ reference electrode (RE) represent the overpotentials that appear during lithium stripping, whereas the negative potentials represent the overpotentials during lithium plating on the WE. The voltage polarization of the cell with a PCN separator was stable over 500 h. As a control, we performed the cycling experiment using the symmetric cell with a polypropylene separator. The voltage polarization of the polypropylene separator cell was stable up to 290 h and then gradually decreased in voltage because of the short-circuit.[327-331] After 290 h, we observed the overpotential (circled, Fig. 4C and D) in the polypropylene separator due to the growth of lithium dendrite[332-335] from the uneven plating behavior of lithium [336, 337], which penetrated the polypropylene separator [338]. The short circuit of the cell with polypropylene separator further explained the low lithium transference number. This low lithium transference number of the polypropylene separator cell indicated the presence of free anions that hinders the fast lithium-ion diffusion and results in the uneven lithium plating and dendrite growth [339, 340]. The stable Li plating/stripping profiles over 500 h without any short circuit of the cell with PCN separator suggested uniform lithium plating and corroborated the high lithium-ion transference number. These results suggested that the PCN separator was a cation-selective membrane that restricted anion mobility, promoted a uniform Li deposition, and suppressed the growth of the dendrite.

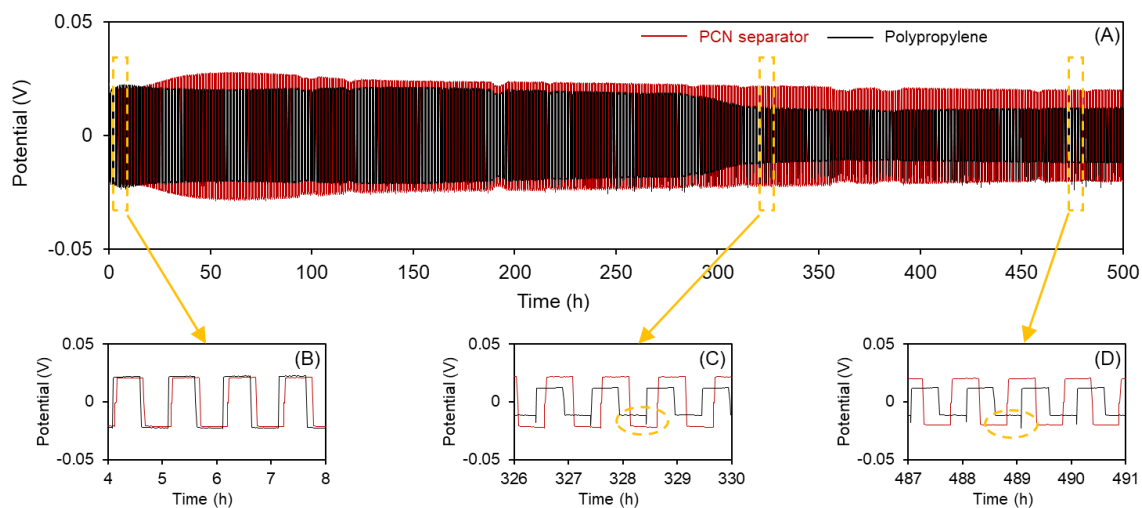


Figure 4. Galvanostatic cycling voltage profiles of a Li/Li symmetric cell cycled at 1 mA/cm² (0.5 mAh/cm²) for 500 h with PCN and polypropylene separators, voltage profiles from 4-8 h (B), 326-330 h (C), and 487-491 h (D). Yellow circles indicated overpotentials from the cell with polypropylene separator.

3.5. Cyclic voltammetry

To investigate the redox behavior of selenium in the electrolyte, we performed cyclic voltammetry on the cell with the PCN separator (**Fig. 5**). As a control, the cell with the polypropylene separator showed two reduction peaks (2.2 and 1.9 V) and one oxidation peak (2.4 V). Initially, the cell with the PCN separator exhibited two reduction peaks and one oxidation peak. The two reduction peaks at 1.9 and 2.2 V revealed multiple reduction transformations of selenium into long-chain polyselenides (Li_2Se_x , $4 \leq x \leq 8$) and subsequent reduction of these long-chain lithium polyselenides to short-chain lithium selenides (Li_2Se_2 and Li_2Se) during the discharging (delithiation) process [288]. Interestingly, cells with both separators showed decreasing peak currents over 15 cycles, which suggested Se cathode dissolution into the electrolyte [341, 342]. We also observed the evolution of a small peak at 1.4 V after five cycles, which we assigned to reduction of LiNO_3 [343, 344]. The one oxidation peak at 2.4 V started to acquire a shoulder after 3 cycles; this shoulder corresponded to conversion of lithium selenides to polyselenides and eventually solid

$\text{Li}_2\text{Se}_2/\text{Li}_2\text{Se}$ [345-348] and suggested intensive polarization and poor stability of the polyselenides in the cathode side. Although the cyclic voltammograms of the cell with either separator showed similar cathodic and anodic features, the peaks were broader for the cell with polypropylene. The cell with the PCN separator showed higher cathodic and anodic peak currents compared with the cell with the polypropylene separator, which suggested that the PCN separator enabled rapid redox kinetics [349].

Next, we determined the diffusion coefficients using the cyclic voltammograms at different scan rates (**Fig. S6**). The calculated diffusion coefficients for the cell with polypropylene separator were $\sim 10^{-13}$ - 10^{-12} cm^2/s (**Table S4**). These values agreed with the reported values [350]. For PCN separator, the calculated diffusion coefficients were 10^{-12} - 10^{-11} cm^2/s . A higher diffusion coefficient of the cell with the PCN separator, compared with the polypropylene separator, suggested that the PCN separator had better electrochemical performance [350] and corroborated the lower charge transfer resistance measured by impedance spectroscopy (**Fig. 3B**).

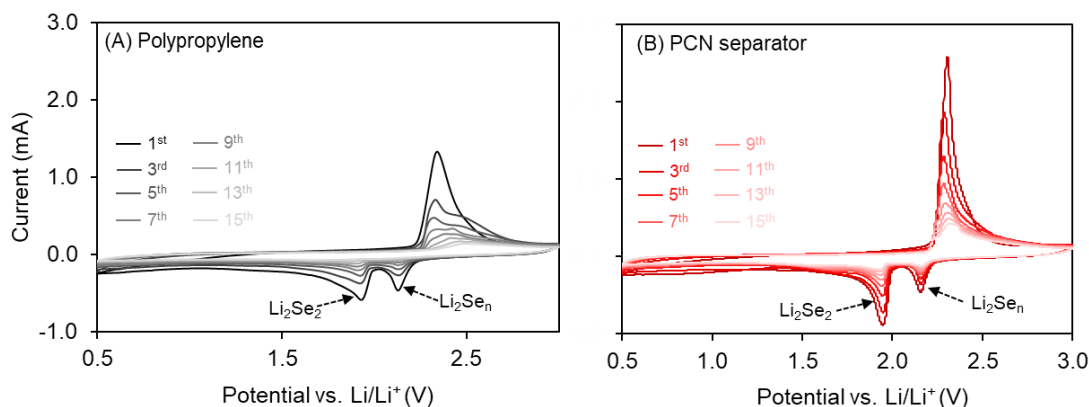


Figure 5. Cyclic voltammetry of cells with polypropylene (A) and PCN (B) separators at a scan rate of 0.1 mV/s at 30°C.

3.6. Electrochemical performance of the cell with PCN separator

To better understand the cell redox behavior, we measured the electrochemical performance of Li/Se cells with the PCN separator at different charge/discharge rates (C-

rates). The cell with a PCN separator had better performance than the cell with the polypropylene separator (**Fig. 6A**). When cycling at different C-rates, the capacities of the cell with PCN separator remained relatively constant at 510 mAh/g for C/5, 360mAh/g for C/2, 190 mAh/g for 2C, and 71 mAh/g for 4C. Then the capacity returned to 482 mAh/g at C/5.

Coulombic efficiency is a key indicator for cycling capability in a commercial cell. To evaluate the capacity of the cell, we initially performed galvanostatic charge-discharge of the cell with both separators at a C/10 rate for 50 cycles (**Fig. 6B**). The Li-Se cell with polypropylene separator lost significant capacity and ended with 228 mAh/g after 50 cycles. Conversely, the cell with PCN separator maintained a reversible capacity of 522 mAh/g after 50 cycles. These results demonstrated that the PCN separator improved electrochemical performance and capacity retention compared with the polypropylene separator.

Next, we investigated the long-term cycle stability of the cell with the PCN separator. The cells were cycled at C/5 and 1C for 500 cycles (**Fig. 6C and D**). The cell with PCN separator had a stable reversible capacity from an initial capacity of 661 mAh/g that became relatively stable (423 mAh/g) at C/5 after 100th cycle. This initial process of ~100 cycles was attributed to activation of the Li-Se cells leading to a highly reversible and stable electrochemical performance, consistent with the observation in Li-S cells.[351] The capacity retention rate of ~64% with a decay rate as low as 0.07% per cycle for 500 cycles suggested stable kinetics of the cells with the PCN separator. These results demonstrated reversible efficiency and kinetics of the cell using a PCN separator compared with the cell with a polypropylene separator, consistent with the stable electrochemical performance of the CV measurement.

As a control, the cell with polypropylene separator had lower capacity than the PCN separator cell at both C/5 and 1C. Moreover, the cell with polypropylene separator required an initial activation as shown in a progressive increase in CE at both C/5 and 1C. When cycled at C/5, the cell with polypropylene separator demonstrated an initial discharge capacity of 350 mAh/g, followed by a progressive decrease in capacity to 102 mAh/g after

500 cycles. Thus, the capacity retention of the cell with polypropylene was 29% with an average decay rate of 0.14% per cycle for 500 cycles. Next, we cycled the cell at 1C. As expected, the discharge capacity of the cell with polypropylene separator dropped rapidly to 107 mAh/g after 500 cycles, whereas the discharge capacity of the cell with PCN separator remained relatively constant at 292 mAh/g with >98% CE for 500 cycles. We did not observe any change in the morphology of the PCN separator after 500 cycles at 1C (**Fig. S7**).

3.7. Characterization of the spent PCN separator

To identify the function of the PCN separator, we performed XPS on the spent PCN separator at C/5 after 50 cycles. The peak deconvolution of the Se 3d region produces two doublet peaks (**Fig. 7A**). The first, strong peak, located at about 54.9 eV, could be attributed to the Se-Se bonds of the backbone structure of chain-like Se_n ($2 < n < 8$) molecules [305, 348, 352, 353]. The other, much weaker doublet peak at 57.9 eV, originated from the terminal Se atoms (most likely forming Se-C or Se-O bonds) of such chain-like molecules. The peak deconvolution of the C1s spectrum yielded four main components at 284.4, 286.3, 288.1, and 290.5 eV, which were identified as sp^2 -hybridized carbon (C=C), hydroxyl or epoxy group (C-O), carbonyl group (C=O), and carboxyl group (O-C=O) or C-Se group, respectively (**Fig. 7B**). There were also two weak peaks at 283.3 and 293.3 eV, but the origins of these peaks were unclear.

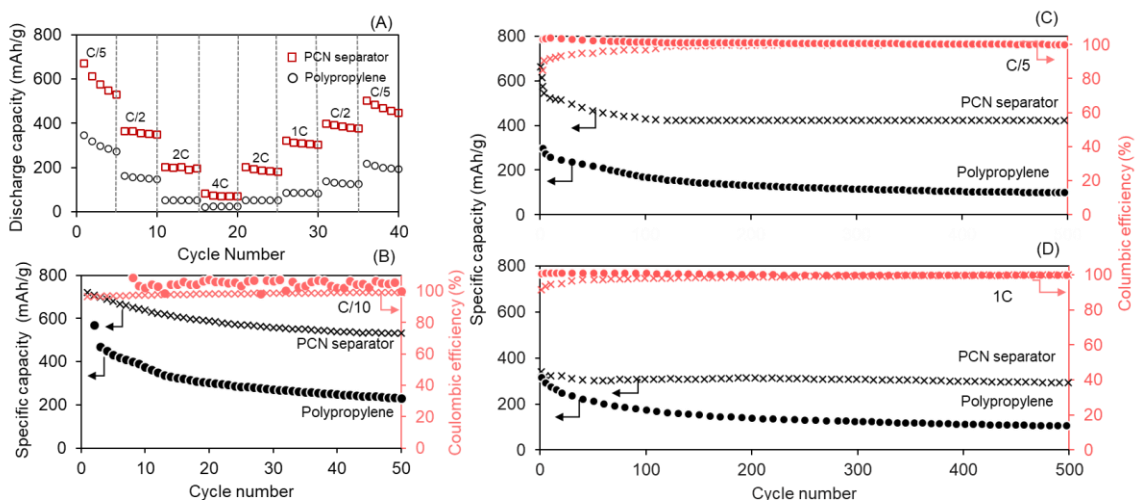


Figure 6. Rate performance with PCN and polypropylene separators at various C-rates from C/5 to 4C (A). Long-term cycling performance of the cells with PCN separator at a rate of C/10 over 50 cycles (B), C/5 (C) and 1C (D) over 500 cycles at 30°C.

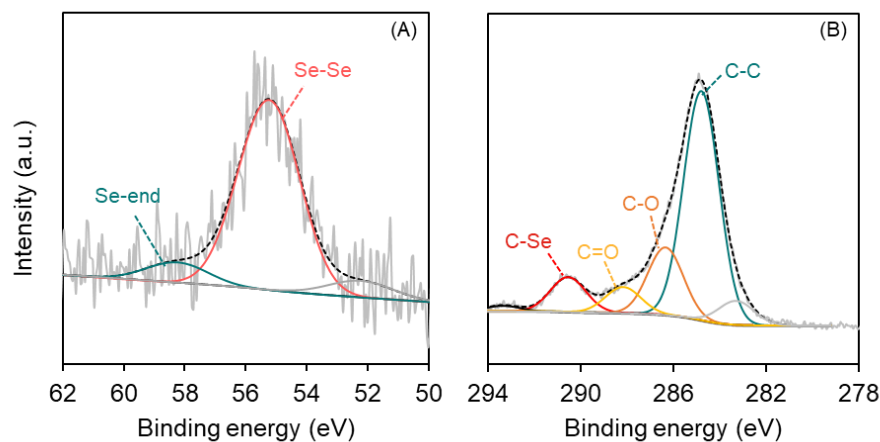


Figure 7. X-Ray Photoelectron spectra of the Se 3d (A) and C 1s (B) of the spent PCN separator on the cathode side.

These results suggested that the PCN separator immobilized the polyselenides, corroborating the self-discharging and permeation tests. We postulated that the immobilization of polyselenides occurred by the interaction between the Lewis base

polyselenides and Lewis acid sites of PCN-250, as shown in the DRIFT spectrum of PCN-250.

5. Discussion

We evaluated the efficacy of PCN separators to suppress the polyselenides shuttling between electrodes. The shuttling of polyselenides leads to severe self-discharge, capacity fade, low Coulombic efficiency, and cycling instability. The PCN separator eliminated these issues by blocking the diffusion of polyselenides. This blocking function enhanced Li^+ transport, long-term cycling stability, and capacity retention as evidenced by a discharge capacity of 423 mAh/g at C/5 and 292 mAh/g with >98% Coulombic efficiency at 1C over 500 cycles.

One of our most significant findings is that the PCN separator acted as a cation-selective membrane, which simultaneously blocked the shuttling of polyselenides and TFSI anions. Most current work on modified separators for Li-Se cells is aimed at suppressing only the shuttling of polyselenides (**Table S5**). The immobilization of TFSI anions, a major contributor to the nonuniform Li deposition, has not been investigated widely. Our permeation and cycling tests demonstrated the ability of the PCN separator to suppress the diffusion of polyselenides and promote uniform lithium nucleation and growth, which prolonged the cell life and prevented Li dendrite growth. A possible reason for the PCN separator blocking of polyselenides and promoting stable lithium deposition is that the Lewis acid sites of PCN-250 anchored the Lewis bases, namely, polyselenides [297] and TFSI [298]. The chemical barriers to polyselenides and TFSI afforded by the PCN separator slowed the loss of active materials (Li and Se) and improved Li^+ transport (high Li^+ transference number), enhancing the capacity retention and long-term cycling stability.

The use of modified separators is a key strategy for suppressing the shuttling of polysulfides. MOFs have been used as separator modifiers to prevent the diffusion of the polysulfides for Li-S batteries (**Table S6**). The combination of porous structure and uniform Lewis acid sites of MOFs allowed transport of lithium ions and suppressed

shuttling of polysulfides (Lewis base) of Li-S systems. Chen et al.[354] synthesized a $\text{Ni}_3(\text{HITP})_2$ -modified separator for Li-S cells and showed that the cell reached ~ 585 mAh/g after 300 cycles at C/2. Although they observed that the cell with $\text{Ni}_3(\text{HITP})_2$ -modified separator delivered a better performance at C/2 over 300 cycles, the capacity progressively decayed. Qi et al.[355] used MIL-125(Ti)-modified separator for Li-S battery. They found that MIL-125(Ti) separator retained the capacity and reached 726 mAh/g at C/5 after 200 cycles. Suriyakumar et al.[356] applied Mn-BTC MOF-modified separator in Li-S battery at C/10 over 80 cycles. They found that the cell with Mn-MOF separator showed superior capacity retention than that with polypropylene separator. These prior results suggested that different MOFs interacted differently with polysulfides.

The application of MOF-modified separator in lithium-selenium batteries has not been assessed. A lack of this knowledge limits our ability to speed the commercialization of the Li-Se batteries. Thus, we compared the PCN separator with other reported multilayer modified separators for Li-Se batteries, such as graphene, MXene, and carbon nanotubes (**Table S5**) [357, 358]. The electrochemical performance of the PCN separator was comparable and even superior to other modified separators in terms of capacity retention, long-term stability (500 cycles), Li^+ transference number, and stability at a high current rate. This information will help design yet more effective separators for Li-Se batteries. We discovered that the PCN separator restricted diffusion of polyselenides and TFSI, which prevented the **uncontrollable growth of lithium dendrite and extended cell life**.

In theory, the Lewis acid characteristics of PCN-250 can interact with TFSI anions (Lewis base). Although our high Li^+ transference number (0.72) and stable voltage profile using the Li/Li symmetric cell with PCN separator implied that the ion-conducting performance in the electrolyte was mainly accomplished by Li^+ , further studies should provide direct evidence of the interaction between TFSI and PCN separator. Moreover, additional studies should decouple the individual contributions of MOF pore size and Lewis acid sites to the blockade of polyselenides and TFSI anion diffusion.

6. Conclusion

Shuttling of polyselenides limits the practical use of lithium-selenium batteries. We fabricated PCN separators that mitigated the shuttle effect of polyselenides. The cells demonstrated a high discharge capacity of 423 mAh/g at a C/5 current rate and 292 mAh/g at 1C with Coulombic efficiency > 98% after 500 cycles. The PCN separator acted as a chemical sieve to suppress the shuttling of polyselenides and promote the uniform Li⁺ transport. As a result, the cells could cycle at C/5 and 1C for 500 cycles with high-capacity retention and Coulombic efficiency. Our findings offer a promising perspective on using PCN-250 as a cation-selective membrane to solve two serious problems in lithium-selenium batteries, the shuttle effect of polyselenides and the uncontrollable growth of lithium dendrite. We expect this PCN separator to be a candidate for high energy density lithium-selenium batteries and to be used with other alkali-metal chalcogenide battery systems.

Supporting Information Chapter 5

Metal-organic framework separator as polyselenide filter for high-performance lithium-selenium batteries

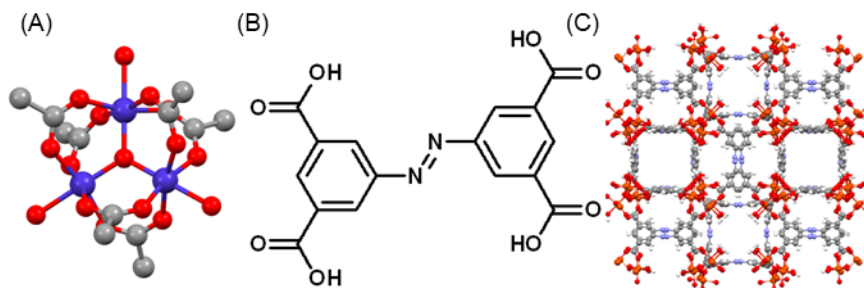


Figure S1. Iron oxo cluster (A), linker (B), and crystal structure (C) of PCN-250.

Table S1. Chemicals and supplies used in this work.

No	Description	Purity	CAS no.	Manufacturer
1	Selenium powder	99+%	7782-49-2	Acro Organics (Waltham, MS, USA)
2	Activated carbon (AC)		7440-44-0	BeanTown Chemical (Hudson, NH, USA)
3	PCN-250(Fe), produced under the commercial name AYRSORB™ F250			framergy, Inc (College Station, TX, USA).
4	Celgard 2400 (Polypropylene)			Celgard, LLC (Charlotte, NC, USA)
5	Poly(vinylidene fluoride-co-hexafluoropropylene (PVDF-HFP, MW 455 kDa)		9011-17-0	Sigma Aldrich (St. Louis, MO USA)
6	Carbon black (Super P)	99+%	1333-86-4	Alfa Aesar (Tewksbury, MA, USA)
7	Lithium chip			MTI Corp (Richmond, CA, USA)

8	Polytetrafluoroethylene (PTFE) condensed liquid binder (PTFE binder)			MTI Corp (Richmond, CA, USA)
9	Lithium bis(trifluoromethylsulfonyl)imide (LiTFSI)	>99%	90076-65-6	VWR (Radnor, PA, USA)
10	1,2-dimethoxyethane (DME)	>99%	110-71-4	VWR (Radnor, PA, USA)
11	1,3- dioxolane (DOL)	>99%	646-06-0	VWR (Radnor, PA, USA)

2.1. Physicochemical properties of PCN-250

To examine the physicochemical properties of the MOF, we characterized PCN-250 by X-ray diffraction (XRD), N₂-adsorption/desorption, scanning electron microscopy (SEM), and Fourier-transform Infrared spectroscopy (FTIR). The N₂-adsorption/desorption isotherm exhibited a Type I isotherm [359, 360], which suggested that PCN-250 was microporous (Fig. S2A). The microporous PCN-250 material had 1542 m²/g surface area, 0.6 cc/g pore volume, and 5.6 Å average pore width (Fig. S2B), similar to reported values [301, 361, 362]. The x-ray diffraction pattern of the PCN-250 matched reported spectra (Fig. S2C) [301, 363]. Our FTIR spectrum of the PCN-250 exhibited the Fe-O stretching peak at 624 cm⁻¹, rocking vibration of CH at 1374 cm⁻¹, vibration of C=C at ~1600 cm⁻¹ and vibration of N=N at ~1400 cm⁻¹ of azo-phenyl group (Fig. S2D), similar to reported spectra [363-367]. The SEM images showed that the average particle size of PCN-250 is ~10 μm (Fig. S4). In sum, the foregoing physical properties confirmed the formation of the PCN-250 material.

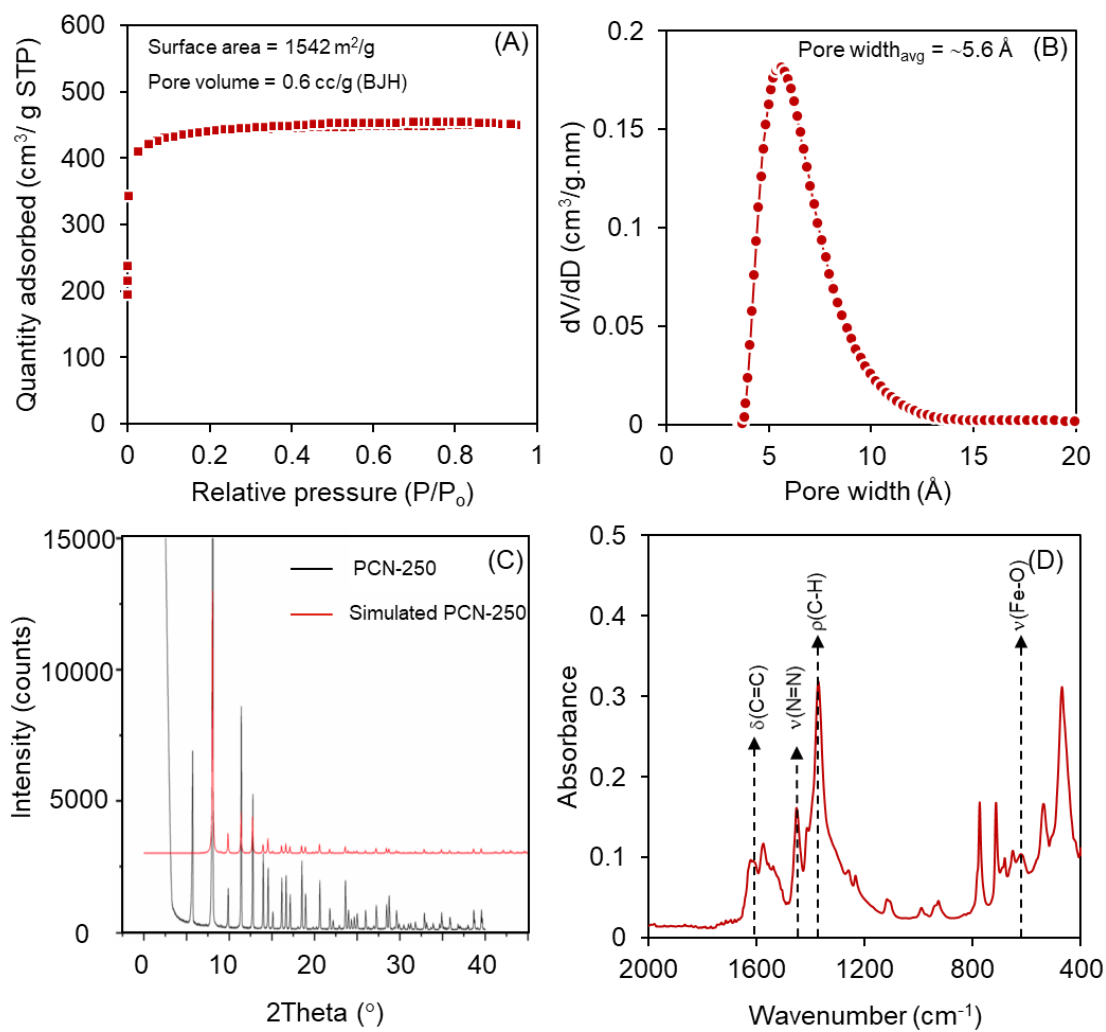


Figure S2. N_2 adsorption/desorption isotherm (A), pore size distribution determined by a Nonlocal Density Functional Theory (NLDFT) model (B), x-ray diffraction spectra (C), Fourier-transform Infrared spectrum of PCN-250 (D).

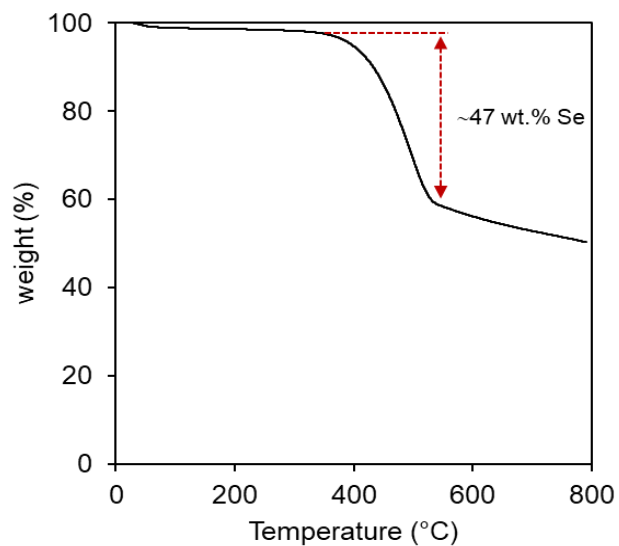


Figure S3. Thermogravimetric analysis of the selenium encapsulated activated carbon cathode.

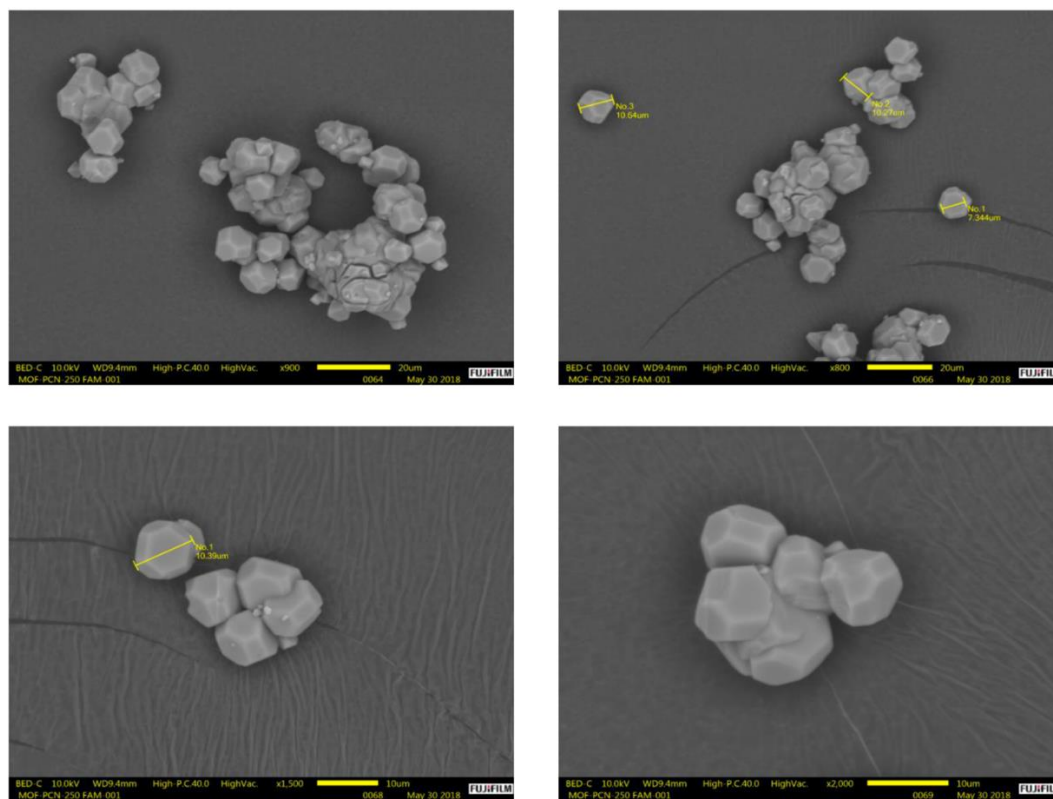


Figure S4. SEM Images of PCN-250 with particle size measurements

Table S2. FTIR peak assignments.

No.	Description of Vibration modes	Wavenumber (cm ⁻¹)
1	CF ₃ asymmetric bending mode, δ_{as} of free triflate anion of LiTFSI	570
2	Overlapping of symmetric bending mode of CF ₃ , δ_s (CF ₃) and combination of C-S and S-N stretching of LiTFSI	750
3	Asymmetric S-N-S stretching, ν_{as} of LiTFSI	1051
4	S=O bonding mode, μ of LiTFSI	1085
5	C-SO ₂ -N bonding mode, η of LiTFSI	1150
6	Asymmetric stretching mode of CF ₃ , ν_{as} of LiTFSI	1193
7	C-SO ₂ -N bonding mode, η of LiTFSI	1335
8	Overlapping of CH ₂ twisting mode of MOF and asymmetric SO ₂ stretching mode, ν_{as} of LiTFSI	1364

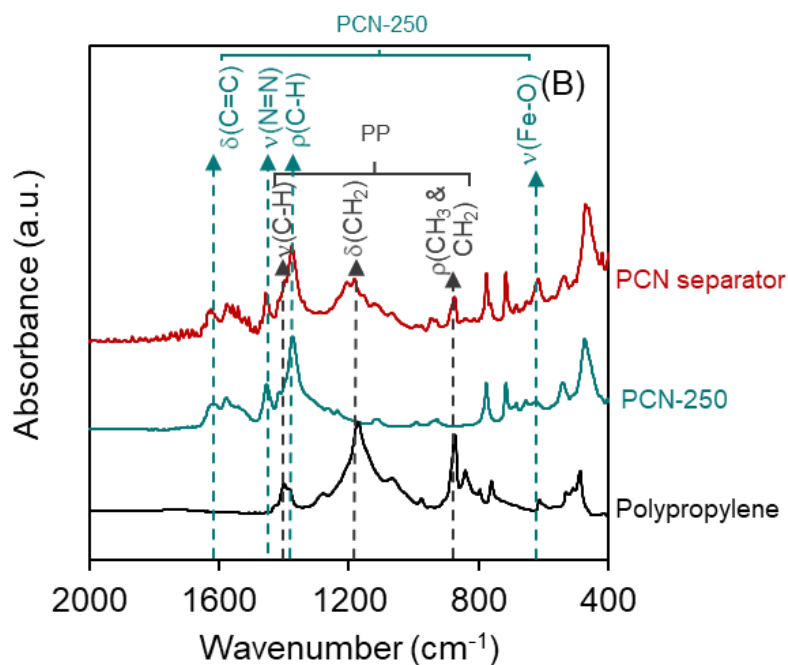
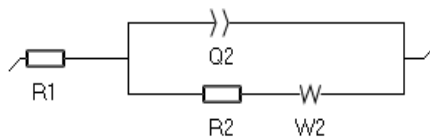


Figure S5. FTIR spectra of polypropylene (PP), PCN-250 particles, and PCN-coated separator

Table S3. Charge transfer resistance (R_2) and Warburg resistance (W_2) obtained by fitting the equivalent circuit with the Nyquist plots



Separator	Initial resistance (Ω)		Final resistance (Ω)	
	R_2	W_2	R_2	W_2
Polypropylene	332	319	381	333
PCN	178	44	232	70

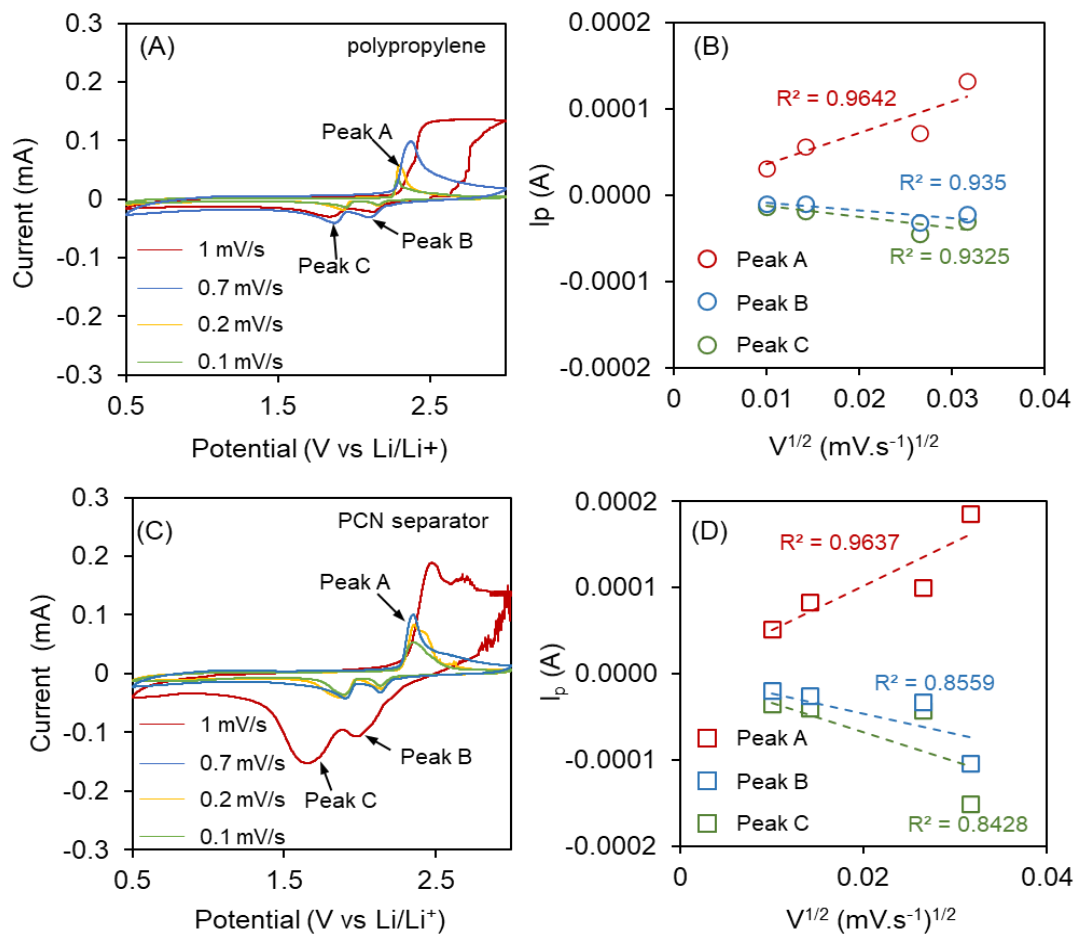


Figure S6. Cyclic voltammetry of the Li/Se cell with/without coated polypropylene separator at different scan rate (a) PCN separator (b) polypropylene separator.

Table S4. Diffusion coefficient of lithium ion (D_{Li^+}) for cells with polypropylene and PCN separators

Peak (mV)\ D_{Li^+} (cm^2/s)	Polypropylene separator	PCN separator
Peak A (2.4V)	8.4×10^{-12}	1.7×10^{-11}
Peak B (2.2V)	5.3×10^{-13}	3.5×10^{-12}
Peak C (1.9 V)	1.1×10^{-12}	7.5×10^{-12}

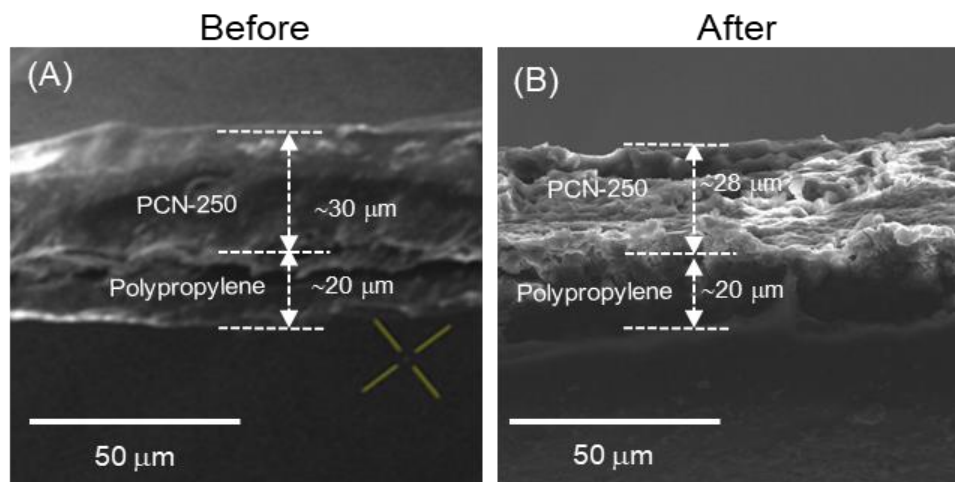


Figure S7. SEM images of PCN separator before (A) and after cell cycle at 1C for 500 cycles (B).

Table S5. Selected separators used in lithium-selenium batteries.

Separator	Host	Active material loading (mg/cm ²)	Average specific capacity (mAh/g) @ different C-rate	Number of cycles	Li ⁺ transference number	Ref.
PCN-250/polypropylene (Celgard 2400)	AC ^a	1.00-1.50	423 @ C/5 292 @ 1C	500 500	0.72	This work
WO ₃ /glass fiber	AAC ^b	1.13-1.77	510 @ C/10	100	-	[368]
Polypropylene (Celgard-2400)	rGO ^c	2.00	341 @ C/5	200	-	[369]
Graphene/polypolypropylene (Celgard-2400)	Super-P	4.00	331 @ C/2	1000	-	[357]
CCNT/MXene/polypropylene (Celgard 3501)	Carbon Black	1.80	478 @ 1C	500	0.61	[358]
Polypropylene (Celgard-2400)	HPCA ^d	1.50-2.00	184 @ 1C	300	-	[346]
Polypropylene (Celgard-2400)	NMPC S ^e	2.00	570 @ C/2	350	-	[370]

Polypropylene (Celgard-2400)	NCS ^f	0.80-1.00	301 @ 1C	500	-	[371]
Polypropylene (Celgard-2400)	NCHP C ^g	0.70-1.00	119 @ 1C	60	-	[347]
Polyethylene/ fish-scale based porous carbon composite/ Celgard-2400	Acetylene/ Black	1.50	638 @ 1C	400	-	[372]
poly-m-phenyleneisophthalamide	Carbon Black	-	458.3 @ C/2	800	-	[373]

^aactivated carbon; ^balkali activated carbon (rice husk); ^creduced graphene oxide; ^dhierarchical porous carbon aerogels; ^eN-methylene phosphonic chitosan; ^fmesoporous nitrogen-doped carbon scaffolds; ^gnitrogen-containing hierarchical porous carbon.

Table S6. Selected metal-organic framework-based separators for battery systems.

Separator	Host	Active material	Active material loading (mg/cm ²)	Average specific capacity (mAh/g) @ different C-rate	Number of cycles	Li ⁺ transference number	Ref.
PCN-250 (Fe)	AC	Se	1-1.50	423 @ C/5 292 @ 1C	500	0.72	This work
Ni ₃ (HITP) ₂	Super P	S	3.50	585 @ C/2	300	-	[354]
UiO-66 (Zr)	Super P	S	1.50	720 @ C/2	500	-	[374]
Zn-HKUST-1	CMK-3	S	-	700 @ 1C	1000	-	[375]
Uio-66-NH ₂ (Zr)@SiO ₂	Graphene	S	0.50	~600 @ C/4	100	0.70	[376]
ZIF-7	Super P	S	1.00	452 @ C/4	300	-	[377]
ZIF-8	Super P	S	1.00	403 @ C/4	300	-	[377]
Y-FTZB ^a	Super P	S	1.00	557 @ C/4	300	-	[377]
HKUST-1 (Cu)	Super P	S	1.00	197 @ C/4	300	-	[377]
HKUST-1 (Cu)	CMK-3 ^b	S	0.60-0.80	855 @ 1C	1500	-	[351]
HKUST-1 (Cu)	RGO	S	1.00-1.50	802 @ C/2	600	0.76	[378]
Cu ₂ (CuTCPP)	Carbon black	S	2.0	604 @ 1C	900	-	[379]

MOF-derived Co ₉ S ₈	Carbon@F e ₃ O ₄	S	2.0	820 @ 1C	1500	-	[380]
Mn-BTC MOF	Graphene	S	-	1450 @ C/10	80	0.45	[356]
MIL-125(Ti)	Ketjen Black	S	2.0	726 @ C/5	200	-	[355]
Ce-MOF	Ketjen Black	S	6.0	839 @ 1C	800	-	[381]
Cu-BTC	Ketjen Black	S	-	1128 @ C/2	500	0.82	[382]
COF ^b (TpPa- SO ₃ Li)	CNT ^c	S	5.4	639 @ C/5	100	0.88	[383]
^a Y-FTZB fcu MOF of H ₂ FTZB and Y- Yttrium; ^b Covalent organic framework; ^c Carbon Nanotube							

CHAPTER 6

CONCLUSION

We have demonstrated Lewis acidic materials as catalysts for lignin upgrading and anion immobilizers for lithium metal batteries. The use of oxophilic metal catalysts, such as Ru and Mo, enabled the formation of oxygen vacancies. The choice of solvents controlled the amount of oxygen vacancies and affected the hydrogenolysis efficiency, product yield, and product distribution from lignin model compounds and technical lignin. These results provide a guide for designing effective catalysts for hydrogenolysis of technical lignin and maximizing the phenolic yields for additional revenues in biorefineries and pulp and paper manufacturers.

Additionally, we applied the Lewis acid interaction concept to control the reactivity and enhance the cell performance of Li-Se batteries. We demonstrated that Lewis acidic MOFs coordinated with Lewis basic anions (TFSI⁻) and polyselenides. As a result, both TFSI⁻ and polyselenides were captured by Lewis acid sites of MOFs and suppressed the polyselenides and anion movement. Furthermore, the immobilization of polyselenides and anions through the grafting of these MOFs onto the separator prevented hazardous dendrite growth and maintained the Li-Se cell capacity over 200 cycles. These findings can be applied to enhance the cell performance of other alkali metal chalcogenide battery systems, such as sodium, magnesium, and aluminum with S, Se, and Te.

Future works will focus on generating bifunctional catalysts using the oxophilic transition metal oxide catalysts for cascade conversions of technical lignin. Moreover, the effect of metal nodes of MOFs on the coordination strength with the anions in the electrolyte will be explored to aid in designing the ion-selective separator for alkali-metal batteries.

REFERENCES

- [1] R. Ahorsu, F. Medina, M. Constantí, Significance and challenges of biomass as a suitable feedstock for bioenergy and biochemical production: A review, *Energies*, 11 (2018) 3366.
- [2] H. Hashim, W.S. Ho, Renewable energy policies and initiatives for a sustainable energy future in Malaysia, *Renew. Sustain. Energy Rev.*, 15 (2011) 4780-4787.
- [3] Y. Ou, N. Kittner, S. Babae, S.J. Smith, C.G. Nolte, D.H. Loughlin, Evaluating long-term emission impacts of large-scale electric vehicle deployment in the US using a human-Earth systems model, *Appl. Energy*, 300 (2021) 117364.
- [4] S.I. Ehrenberger, J.B. Dunn, G. Jungmeier, H. Wang, An international dialogue about electric vehicle deployment to bring energy and greenhouse gas benefits through 2030 on a well-to-wheels basis, *Transportation Research Part D: Transport and Environment*, 74 (2019) 245-254.
- [5] W. Jin, L. Pastor-Pérez, D. Shen, A. Sepúlveda-Escribano, S. Gu, T. Ramirez Reina, Catalytic upgrading of biomass model compounds: novel approaches and lessons learnt from traditional hydrodeoxygenation—a review, *ChemCatChem*, 11 (2019) 924-960.
- [6] X. Li, W. Dong, J. Zhang, S. Shao, Y. Cai, Preparation of bio-oil derived from catalytic upgrading of biomass vacuum pyrolysis vapor over metal-loaded HZSM-5 zeolites, *Journal of the Energy Institute*, 93 (2020) 605-613.
- [7] F. Deng, A.S. Amarasekara, Catalytic upgrading of biomass derived furans, *Ind. Crops Prod.*, 159 (2021) 113055.
- [8] J.C. Védrine, Heterogeneous catalysis on metal oxides, *Catalysts*, 7 (2017) 341.
- [9] J. Pang, J. Sun, M. Zheng, H. Li, Y. Wang, T. Zhang, Transition metal carbide catalysts for biomass conversion: A review, *Appl. Catal. B: Environ.*, 254 (2019) 510-522.
- [10] E. Taarning, C.M. Osmundsen, X. Yang, B. Voss, S.I. Andersen, C.H. Christensen, Zeolite-catalyzed biomass conversion to fuels and chemicals, *Energy Environ. Sci.*, 4 (2011) 793-804.
- [11] A. Herbst, C. Janiak, MOF catalysts in biomass upgrading towards value-added fine chemicals, *CrystEngComm*, 19 (2017) 4092-4117.
- [12] Y.-T. Liao, B.M. Matsagar, K.C.-W. Wu, Metal-organic framework (MOF)-derived effective solid catalysts for valorization of lignocellulosic biomass, *ACS Sustain. Chem. Eng.*, 6 (2018) 13628-13643.
- [13] H. Zhang, X. Liu, Y. Wu, C. Guan, A.K. Cheetham, J. Wang, MOF-derived nanohybrids for electrocatalysis and energy storage: current status and perspectives, *Chem. Commun.*, 54 (2018) 5268-5288.
- [14] J. Ren, Y. Huang, H. Zhu, B. Zhang, H. Zhu, S. Shen, G. Tan, F. Wu, H. He, S. Lan, Recent progress on MOF-derived carbon materials for energy storage, *Carbon Energy*, 2 (2020) 176-202.
- [15] X. Zhang, A. Chen, M. Zhong, Z. Zhang, X. Zhang, Z. Zhou, X.-H. Bu, Metal-organic frameworks (MOFs) and MOF-derived materials for energy storage and conversion, *Electrochemical Energy Reviews*, 2 (2019) 29-104.
- [16] H.B. Wu, X.W. Lou, Metal-organic frameworks and their derived materials for electrochemical energy storage and conversion: Promises and challenges, *Sci. Adv.*, 3 (2017) eaap9252.
- [17] B.Y. Guan, X.Y. Yu, H.B. Wu, X.W. Lou, Complex nanostructures from materials based on metal-organic frameworks for electrochemical energy storage and conversion, *Adv. Mater.*, 29 (2017) 1703614.
- [18] W. Xia, A. Mahmood, R. Zou, Q. Xu, Metal-organic frameworks and their derived nanostructures for electrochemical energy storage and conversion, *Energy Environ. Sci.*, 8 (2015) 1837-1866.
- [19] A. Agarwal, M. Rana, J.-H. Park, Advancement in technologies for the depolymerization of lignin, *Fuel Process. Technol.*, 181 (2018) 115-132.

- [20] C. Chio, M. Sain, W. Qin, Lignin utilization: a review of lignin depolymerization from various aspects, *Renew. Sustain. Energy Rev.*, 107 (2019) 232-249.
- [21] Y. Zhu, Z. Han, L. Fu, C. Liu, D. Zhang, Cleavage of the β -O-4 bond in a lignin model compound using the acidic ionic liquid 1-H-3-methylimidazolium chloride as catalyst: a DFT mechanistic study, *J. Mol. Model.*, 24 (2018) 1-8.
- [22] J. Gierer, Chemical aspects of kraft pulping, *Wood Sci. Technol.*, 14 (1980) 241-266.
- [23] S. Qi, G. Wang, H. Sun, L. Wang, Q. Liu, G. Ma, A.M. Parvez, C. Si, Using lignin monomer as a novel capping agent for efficient acid-catalyzed depolymerization of high molecular weight lignin to improve its antioxidant activity, *ACS Sustain. Chem. Eng.*, 8 (2020) 9104-9114.
- [24] X. Ouyang, X. Huang, B.M. Hendriks, M.D. Boot, E.J. Hensen, Coupling organosolv fractionation and reductive depolymerization of woody biomass in a two-step catalytic process, *Green Chem.*, 20 (2018) 2308-2319.
- [25] Z. Sun, B. Fridrich, A. de Santi, S. Elangovan, K. Barta, Bright side of lignin depolymerization: toward new platform chemicals, *Chem. Rev.*, 118 (2018) 614-678.
- [26] A. Deepa, P.L. Dhepe, Solid acid catalyzed depolymerization of lignin into value added aromatic monomers, *RSC Adv.*, 4 (2014) 12625-12629.
- [27] A.K. Deepa, P.L. Dhepe, Lignin depolymerization into aromatic monomers over solid acid catalysts, *ACS Catal.*, 5 (2015) 365-379.
- [28] Z. Ma, E. Troussard, J.A. Van Bokhoven, Controlling the selectivity to chemicals from lignin via catalytic fast pyrolysis, *Appl. Catal. A-Gen.*, 423 (2012) 130-136.
- [29] C. Li, X. Zhao, A. Wang, G.W. Huber, T. Zhang, Catalytic transformation of lignin for the production of chemicals and fuels, *Chem. Rev.*, 115 (2015) 11559-11624.
- [30] X. Zhang, Q. Zhang, J. Long, Y. Xu, T. Wang, L. Ma, Y. Li, Phenolics production through catalytic depolymerization of alkali lignin with metal chlorides, *BioResources*, 9 (2014) 3347-3360.
- [31] L.-P. Xiao, S. Wang, H. Li, Z. Li, Z.-J. Shi, L. Xiao, R.-C. Sun, Y. Fang, G. Song, Catalytic hydrogenolysis of lignins into phenolic compounds over carbon nanotube supported molybdenum oxide, *ACS Catal.*, 7 (2017) 7535-7542.
- [32] P.J. Deuss, K. Barta, From models to lignin: Transition metal catalysis for selective bond cleavage reactions, *Coord. Chem. Rev.*, 306 (2016) 510-532.
- [33] T. Prasomsri, T. Nimmanwudipong, Y. Román-Leshkov, Effective hydrodeoxygenation of biomass-derived oxygenates into unsaturated hydrocarbons by MoO₃ using low H₂ pressures, *Energy Environ. Sci.*, 6 (2013) 1732-1738.
- [34] G. Xu, P. Nie, H. Dou, B. Ding, L. Li, X. Zhang, Exploring metal organic frameworks for energy storage in batteries and supercapacitors, *Mater. Today*, 20 (2017) 191-209.
- [35] X.-C. Xie, K.-J. Huang, X. Wu, Metal-organic framework derived hollow materials for electrochemical energy storage, *J. Mater. Chem. A*, 6 (2018) 6754-6771.
- [36] C. Wang, Y.V. Kaneti, Y. Bando, J. Lin, C. Liu, J. Li, Y. Yamauchi, Metal-organic framework-derived one-dimensional porous or hollow carbon-based nanofibers for energy storage and conversion, *Mater. Horiz.*, 5 (2018) 394-407.
- [37] A.E. Baumann, D.A. Burns, B. Liu, V.S. Thoi, Metal-organic framework functionalization and design strategies for advanced electrochemical energy storage devices, *Communications Chemistry*, 2 (2019) 1-14.
- [38] Y. Cao, H. Wu, G. Li, C. Liu, L. Cao, Y. Zhang, W. Bao, H. Wang, Y. Yao, S. Liu, Ion selective covalent organic framework enabling enhanced electrochemical performance of lithium-sulfur batteries, *Nano Lett.*, 21 (2021) 2997-3006.
- [39] J. Zheng, J. Tian, D. Wu, M. Gu, W. Xu, C. Wang, F. Gao, M.H. Engelhard, J.-G. Zhang, J. Liu, Lewis acid-base interactions between polysulfides and metal organic framework in lithium sulfur batteries, *Nano Lett.*, 14 (2014) 2345-2352.
- [40] R. Zhao, Y. Wu, Z. Liang, L. Gao, W. Xia, Y. Zhao, R. Zou, Metal-organic frameworks for solid-state electrolytes, *Energy Environ. Sci.*, 13 (2020) 2386-2403.

- [41] E.M. Erickson, E. Markevich, G. Salitra, D. Sharon, D. Hirshberg, E. de la Llave, I. Shterenberg, A. Rosenman, A. Frimer, D. Aurbach, Development of advanced rechargeable batteries: a continuous challenge in the choice of suitable electrolyte solutions, *J. Electrochem. Soc.*, 162 (2015) A2424.
- [42] D. Deng, Li-ion batteries: basics, progress, and challenges, *Energy Science & Engineering*, 3 (2015) 385-418.
- [43] X. Wang, Y. Hou, Y. Zhu, Y. Wu, R. Holze, An aqueous rechargeable lithium battery using coated Li metal as anode, *Sci. Rep.*, 3 (2013) 1-5.
- [44] Q. Zhang, J. Chang, T. Wang, Y. Xu, Review of biomass pyrolysis oil properties and upgrading research, *Energy Convers. Manag.*, 48 (2007) 87-92.
- [45] S.N. Naik, V.V. Goud, P.K. Rout, A.K. Dalai, Production of first and second generation biofuels: a comprehensive review, *Renewable and sustainable energy reviews*, 14 (2010) 578-597.
- [46] R. Datta, M. Henry, Lactic acid: recent advances in products, processes and technologies — a review, *J. Chem. Technol. Biotechnol.*, 81 (2006) 1119-1129.
- [47] O. Martin, L. Avérous, Poly (lactic acid): plasticization and properties of biodegradable multiphase systems, *Polymer*, 42 (2001) 6209-6219.
- [48] A. Repa, C. Grangette, C. Daniel, R. Hochreiter, K. Hoffmann-Sommergruber, J. Thalhamer, D. Kraft, H. Breiteneder, A. Mercenier, U. Wiedermann, Mucosal co-application of lactic acid bacteria and allergen induces counter-regulatory immune responses in a murine model of birch pollen allergy, *Vaccine*, 22 (2003) 87-95.
- [49] E. Zannini, D.M. Waters, A. Coffey, E.K. Arendt, Production, properties, and industrial food application of lactic acid bacteria-derived exopolysaccharides, *Appl. Microbiol. Biotechnol.*, 100 (2016) 1121-1135.
- [50] E. Vink, D. Glassner, J. Kolstad, R. Wooley, R. O'Connor, The eco-profiles for current and near-future NatureWorks® polylactide (PLA) production, *Ind. Biotechnol.*, 3 (2007) 58-81.
- [51] C. Pereira, V. Silva, A. Rodrigues, Ethyl lactate as a solvent: Properties, applications and production processes – a review, *Green Chem*, 13 (2011) 2658-2671.
- [52] K. Sakai, Y. Murata, H. Yamazumi, Y. Tau, M. Mori, M. Moriguchi, Y. Shirai, Selective proliferation of lactic acid bacteria and accumulation of lactic acid during open fermentation of kitchen refuse with intermittent pH adjustment, *Food Sci. Technol. Res.*, 6 (2007) 140-145.
- [53] E. Papamanoli, N. Tzanetakis, E. Litopoulou-Tzanetaki, P. Kotzekidou, Characterization of lactic acid bacteria isolated from a Greek dry-fermented sausage in respect of their technological and probiotic properties, *Meat Sci.*, 65 (2003) 859-867.
- [54] Y. Koito, K. Nakajima, M. Kitano, M. Hara, Efficient conversion of pyruvic aldehyde into lactic acid by lewis acid catalyst in water, *Chem. Lett.*, 42 (2013) 873-875.
- [55] S. Lux, M. Siebenhofer, Catalytic conversion of dihydroxyacetone to lactic acid with Brønsted acids and multivalent metal ions, *Chemical and biochemical engineering quarterly*, 29 (2015) 575-585.
- [56] C.B. Rasrendra, B.A. Fachri, I.G.B. Makertihartha, S. Adisasmito, H.J. Heeres, Catalytic conversion of dihydroxyacetone to lactic acid using metal salts in water, *ChemSusChem*, 4 (2011) 768-777.
- [57] J. Cejka, A. Corma, S. Zones, *Zeolites and catalysis: synthesis, reactions and applications*, John Wiley & Sons 2010.
- [58] A. Martínez, G. Prieto, The application of zeolites and periodic mesoporous silicas in the catalytic conversion of synthesis gas, *Topics in Catalysis*, 52 (2009) 75.
- [59] A. Corma, *Application of Zeolites in Fluid Catalytic Cracking and Related Processes*, *Studies in surface science and catalysis*, Elsevier 1989, pp. 49-67.
- [60] G. Caeiro, R. Carvalho, X. Wang, M. Lemos, F. Lemos, M. Guisnet, F.R. Ribeiro, Activation of C2–C4 alkanes over acid and bifunctional zeolite catalysts, *J. Mol. Catal. A Chem.*, 255 (2006) 131-158.

- [61] M.N. Akhtar, N. Al-Yassir, S. Al-Khattaf, J. Čejka, Aromatization of alkanes over Pt promoted conventional and mesoporous gallosilicates of MEL zeolite, *Catal. Today*, 179 (2012) 61-72.
- [62] A. Smiešková, E. Rojasová, P. Hudec, L. Šabo, Aromatization of light alkanes over ZSM-5 catalysts: Influence of the particle properties of the zeolite, *Appl. Catal. A-Gen.*, 268 (2004) 235-240.
- [63] M.S. Rahaman, T.K. Phung, M.A. Hossain, E. Chowdhury, S. Tulaphol, S.B. Lalvani, M. O'Toole, G.A. Willing, J.B. Jasinski, M. Crocker, Hydrophobic functionalization of HY zeolites for efficient conversion of glycerol to solketal, *Appl. Catal. A-Gen.*, (2020) 117369.
- [64] C. Patil, P. Niphadkar, V. Bokade, P. Joshi, Esterification of levulinic acid to ethyl levulinate over bimodal micro-mesoporous H/BEA zeolite derivatives, *Catal. Commun.*, 43 (2014) 188-191.
- [65] P. Ferreira, I. Fonseca, A. Ramos, J. Vital, J. Castanheiro, Esterification of glycerol with acetic acid over dodecamolybdophosphoric acid engaged in USY zeolite, *Catal. Commun.*, 10 (2009) 481-484.
- [66] S.R. Kirumakki, N. Nagaraju, K.V. Chary, S. Narayanan, Kinetics of esterification of aromatic carboxylic acids over zeolites H β and HZSM5 using dimethyl carbonate, *Appl. Catal. A-Gen.*, 248 (2003) 161-167.
- [67] S.R. Kirumakki, N. Nagaraju, S. Narayanan, A comparative esterification of benzyl alcohol with acetic acid over zeolites H β , HY and HZSM5, *Appl. Catal. A-Gen.*, 273 (2004) 1-9.
- [68] S.R. Kirumakki, N. Nagaraju, K.V. Chary, Esterification of alcohols with acetic acid over zeolites H β , HY and HZSM5, *Appl. Catal. A-Gen.*, 299 (2006) 185-192.
- [69] L. Young, S. Butter, W. Kaeding, Shape selective reactions with zeolite catalysts: III. Selectivity in xylene isomerization, toluene-methanol alkylation, and toluene disproportionation over ZSM-5 zeolite catalysts, *Journal of Catalysis*, 76 (1982) 418-432.
- [70] V.R. Choudhary, S.K. Jana, B. Kiran, Alkylation of benzene by benzyl chloride over H-ZSM-5 zeolite with its framework Al completely or partially substituted by Fe or Ga, *Catal. Lett.*, 59 (1999) 217-219.
- [71] A. Palomares, G. Eder-Mirth, J. Lercher, Selective alkylation of toluene over basic zeolites: an in situ infrared spectroscopic investigation, *J. Catal.*, 168 (1997) 442-449.
- [72] M. Moliner, Y. Román-Leshkov, M.E. Davis, Tin-containing zeolites are highly active catalysts for the isomerization of glucose in water, *Proceedings of the National Academy of Sciences*, 107 (2010) 6164-6168.
- [73] R. Bermejo-Deval, R.S. Assary, E. Nikolla, M. Moliner, Y. Román-Leshkov, S.-J. Hwang, A. Palsdottir, D. Silverman, R.F. Lobo, L.A. Curtiss, Metalloenzyme-like catalyzed isomerizations of sugars by Lewis acid zeolites, *PNAS*, 109 (2012) 9727-9732.
- [74] T. Isoda, S. Nagao, X. Ma, Y. Korai, I. Mochida, Hydrodesulfurization pathway of 4, 6-dimethyldibenzothiophene through isomerization over Y-zeolite containing CoMo/Al₂O₃ catalyst, *Energy Fuels*, 10 (1996) 1078-1082.
- [75] X. Wang, F. Liang, C. Huang, Y. Li, B. Chen, Highly active tin (IV) phosphate phase transfer catalysts for the production of lactic acid from triose sugars, *Catal. Sci. Technol.*, 5 (2015) 4410-4421.
- [76] J. Wang, Y. Masui, M. Onaka, Conversion of triose sugars with alcohols to alkyl lactates catalyzed by Brønsted acid tin ion-exchanged montmorillonite, *Appl. Catal. B: Environ.*, 107 (2011) 135-139.
- [77] Q. Guo, F. Fan, E.A. Pidko, W.N. Van Der Graaff, Z. Feng, C. Li, E.J. Hensen, Highly Active and Recyclable Sn-MWW Zeolite Catalyst for Sugar Conversion to Methyl Lactate and Lactic Acid, *ChemSusChem*, 6 (2013) 1352-1356.
- [78] P.Y. Dapsens, C. Mondelli, J. Pérez-Ramírez, Highly selective Lewis acid sites in desilicated MFI zeolites for dihydroxyacetone isomerization to lactic acid, *ChemSusChem*, 6 (2013) 831-839.

- [79] J. van Bokhoven, M. Tromp, D. Koningsberger, J. Miller, J. Pieterse, J. Lercher, B. Williams, H. Kung, An explanation for the enhanced activity for light alkane conversion in mildly steam dealuminated mordenite: The dominant role of adsorption, *J. Catal.*, 202 (2001) 129-140.
- [80] A. To, R. Jentoft, W. Alvarez, S. Crossley, D. Resasco, Generation of synergistic sites by thermal treatment of HY zeolite. Evidence from the reaction of hexane isomers, *J. Catal.*, 317 (2014) 11-21.
- [81] T. Hoff, R. Thilakaratne, D. Gardner, R. Brown, J.-P. Tessonier, Thermal stability of aluminum-rich ZSM-5 zeolites and consequences on aromatization reactions, *J. Phys. Chem. C*, 120 (2016) 20103-20113.
- [82] P.P. Pescarmona, K.P.F. Janssen, C. Delaet, C. Stroobants, K. Houthoofd, A. Philippaerts, C. De Jonghe, J.S. Paul, P.A. Jacobs, B.F. Sels, Zeolite-catalysed conversion of C3 sugars to alkyl lactates, *Green Chem.*, 12 (2010) 1083-1089.
- [83] Y. Chu, X. Yi, C. Li, X. Sun, A. Zheng, Brønsted/Lewis acid sites synergistically promote the initial C–C bond formation in the MTO reaction, *Chem. Sci.*, 9 (2018) 6470-6479.
- [84] T.C. Hoff, R. Thilakaratne, D.W. Gardner, R.C. Brown, J. Tessonier, Thermal stability of aluminum-rich ZSM-5 zeolites and consequences on aromatization reactions, *The Journal of Physical Chemistry C*, 120 (2016) 20103-20113.
- [85] S. Brunauer, P. Emmett, E. Teller, Adsorption of gases in multimolecular layers, *J. Am. Chem. Soc.*, 60 (1938) 309-319.
- [86] E. Barrett, L. Joyner, P. Halenda, The determination of pore volume and area distributions in porous substances. I. Computations from nitrogen isotherms, *J. Am. Chem. Soc.*, 73 (1951) 373-380.
- [87] Y. Ji, A. Lawal, A. Nyholm, R. Gorte, O. Abdelrahman, Dehydro-decyclization of Tetrahydrofurans to Diene Monomers over Metal Oxides, *Catal. Sci. Technol.*, (2020).
- [88] F. Jin, Y. Li, A FTIR and TPD examination of the distributive properties of acid sites on ZSM-5 zeolite with pyridine as a probe molecule, *Catal. Today*, 145 (2009) 101-107.
- [89] J. Rorrer, Y. He, F.D. Toste, A.T. Bell, Mechanism and kinetics of 1-dodecanol etherification over tungstated zirconia, *J. Catal.*, 354 (2017) 13-23.
- [90] A. Starace, B. Black, D. Lee, E. Palmiotti, K. Orton, W. Michener, J. ten Dam, M. Watson, G. Beckham, K. Magrini, C. Mukarakate, Characterization and Catalytic Upgrading of Aqueous Stream Carbon from Catalytic Fast Pyrolysis of Biomass, *ACS Sustainable Chem. Eng.*, 5 (2017) 11761-11769.
- [91] M. Rutkowska, D. Macina, Z. Piwowarska, M. Gajewska, U. Díaz, L. Chmielarz, Hierarchically structured ZSM-5 obtained by optimized mesotemplate-free method as active catalyst for methanol to DME conversion, *Catal. Sci. Technol.*, 6 (2016) 4849-4862.
- [92] H. Van Koningsveld, J. Jansen, H. Van Bekkum, The monoclinic framework structure of zeolite H-ZSM-5. Comparison with the orthorhombic framework of as-synthesized ZSM-5, *Zeolites*, 10 (1990) 235-242.
- [93] C. Triantafyllidis, A. Vlessidis, L. Nalbandian, N. Evmiridis, Effect of the degree and type of the dealumination method on the structural, compositional and acidic characteristics of H-ZSM-5 zeolites, *Microporous Mesoporous Mater.*, 47 (2001) 369-388.
- [94] K.S. Triantafyllidis, L. Nalbandian, P.N. Trikalitis, A.K. Ladavos, T. Mavromoustakos, C.P. Nicolaides, Structural, compositional and acidic characteristics of nanosized amorphous or partially crystalline ZSM-5 zeolite-based materials, *Microporous Mesoporous Mater.*, 75 (2004) 89-100.
- [95] S. Li, A. Zheng, Y. Su, H. Zhang, L. Chen, J. Yang, C. Ye, F. Deng, Brønsted/Lewis Acid Synergy in Dealuminated HY Zeolite: A Combined Solid-State NMR and Theoretical Calculation Study, *J. Am. Chem. Soc.*, 129 (2007) 11161-11171.

- [96] R. Shannon, K. Gardner, R. Staley, G. Bergeret, P. Gallezot, A. Auroux, The nature of the nonframework aluminum species formed during the dehydroxylation of HY, *J. Phys. Chem.*, 89 (1985) 4778-4788.
- [97] A. Takagaki, H. Goto, R. Kikuchi, S. Oyama, Silica-supported chromia-titania catalysts for selective formation of lactic acid from a triose in water, *Appl. Catal., A*, 570 (2019) 200-208.
- [98] E. Jolimaitre, D. Delcroix, N. Essayem, C. Pinel, M. Besson, Dihydroxyacetone conversion into lactic acid in an aqueous medium in the presence of metal salts: influence of the ionic thermodynamic equilibrium on the reaction performance, *Catal. Sci. Technol.*, 8 (2018) 1349-1356.
- [99] X. Wang, F. Liang, C. Huang, Y. Li, B. Chen, Siliceous tin phosphates as effective bifunctional catalysts for selective conversion of dihydroxyacetone to lactic acid, *Catal. Sci. Technol.*, 6 (2016) 6551-6560.
- [100] R.M. West, M.S. Holm, S. Saravanamurugan, J. Xiong, Z. Beversdorf, E. Taarning, C.H. Christensen, Zeolite H-USY for the production of lactic acid and methyl lactate from C3-sugars, *J. Catal.*, 269 (2010) 122-130.
- [101] K. Nakajima, J. Hirata, M. Kim, N. Gupta, T. Murayama, A. Yoshida, N. Hiyoshi, A. Fukuoka, W. Ueda, Facile formation of lactic acid from a triose sugar in water over niobium oxide with a deformed orthorhombic phase, *ACS Catal.*, 8 (2018) 283-290.
- [102] K. Santos, E. Albuquerque, L. Borges, M. Fraga, Discussing Lewis and Brønsted acidity on continuous pyruvaldehyde Cannizzaro reaction to lactic acid over solid catalysts, *Mol. Catal.*, 458 (2018) 198-205.
- [103] D. Verboekend, A. Chabaneix, K. Thomas, J.-P. Gilson, J. Pérez-Ramírez, Mesoporous ZSM-22 zeolite obtained by desilication: peculiarities associated with crystal morphology and aluminium distribution, *CrystEngComm*, 13 (2011) 3408-3416.
- [104] A. Feliczak-Guzik, M. Sprynskyy, I. Nowak, B. Buszewski, Catalytic isomerization of dihydroxyacetone to lactic acid and alkyl lactates over hierarchical zeolites containing tin, *Catalysts*, 8 (2018) 31.
- [105] E. Taarning, S. Saravanamurugan, M. Holm, J. Xiong, R. West, C. Christensen, Zeolite-catalyzed isomerization of triose sugars, *ChemSusChem*, 2 (2009) 625-627.
- [106] X. Wang, F. Liang, C. Huang, Y. Li, B. Chen, Siliceous tin phosphates as effective bifunctional catalysts for selective conversion of dihydroxyacetone to lactic acid, *Catal. Sci. Technol.*, 6 (2016) 6551-6560.
- [107] P. Smith, *Chemistry of tin*, Springer Science & Business Media 2012.
- [108] K.A. Tarach, J. Tekla, U. Filek, A. Szymocha, I. Tarach, K. Góra-Marek, Alkaline-acid treated zeolite L as catalyst in ethanol dehydration process, *Microporous Mesoporous Mater.*, 241 (2017) 132-144.
- [109] D.M. Dal Pozzo, J.A. Azevedo dos Santos, E.S. Júnior, R.F. Santos, A. Feiden, S.N. Melegari de Souza, I. Burgardt, Free fatty acids esterification catalyzed by acid Faujasite type zeolite, *RSC Advances*, 9 (2019) 4900-4907.
- [110] A.P. Bolton, M.A. Lanewala, A mechanism for the isomerization of the hexanes using zeolite catalysts, *J. Catal.*, 18 (1970) 1-11.
- [111] P.M. Veiga, A.C.L. Gomes, C.O. Veloso, C.A. Henriques, Acid zeolites for glycerol etherification with ethyl alcohol: Catalytic activity and catalyst properties, *Appl. Catal., A*, 548 (2017) 2-15.
- [112] F. Yang, J. Fu, J. Mo, X. Lu, Synergy of Lewis and Brønsted Acids on Catalytic Hydrothermal Decomposition of Hexose to Levulinic Acid, *Energy Fuels*, 27 (2013) 6973-6978.
- [113] S. Tulaphol, M.A. Hossain, M.S. Rahaman, L.Y. Liu, T.K. Phung, S. Rennecker, N. Grisdanurak, N. Sathitsuksanoh, Direct Production of Levulinic Acid in One Pot from Hemp Hurd by Dilute Acid in Ionic Liquids, *Energy Fuels*, 34 (2020) 1764-1772.

- [114] N. Xue, A. Vjunov, S. Schallmoser, J. Fulton, M. Sanchez-Sanchez, J. Hu, D. Mei, J. Lercher, Hydrolysis of zeolite framework aluminum and its impact on acid catalyzed alkane reactions, *J. Catal.*, 365 (2018) 359-366.
- [115] R. Gounder, A. Jones, R. Carr, E. Iglesia, Solvation and acid strength effects on catalysis by faujasite zeolites, *J. Catal.*, 286 (2012) 214-223.
- [116] T. Le, A. Chawla, J. Rimer, Impact of Acid Site Speciation and Spatial Gradients on Zeolite Catalysis, *J. Catal.*, (2020).
- [117] X. Yi, K. Liu, W. Chen, J. Li, S. Xu, C. Li, Y. Xiao, H. Liu, X. Guo, S.-B. Liu, A. Zheng, Origin and Structural Characteristics of Tri-coordinated Extra-framework Aluminum Species in Dealuminated Zeolites, *JACS*, 140 (2018) 10764-10774.
- [118] A. Zheng, S. Li, S.-B. Liu, F. Deng, Acidic Properties and Structure–Activity Correlations of Solid Acid Catalysts Revealed by Solid-State NMR Spectroscopy, *Acc. Chem. Res.*, 49 (2016) 655-663.
- [119] R.M. West, M.S. Holm, S. Saravanamurugan, J. Xiong, Z. Beversdorf, E. Taarning, C.H. Christensen, Zeolite H-USY for the production of lactic acid and methyl lactate from C3-sugars, *J. Catal.*, 269 (2010) 122-130.
- [120] M. Xia, W. Dong, M. Gu, C. Chang, Z. Shen, Y. Zhang, Synergetic effects of bimetals in modified beta zeolite for lactic acid synthesis from biomass-derived carbohydrates, *RSC Adv.*, 8 (2018) 8965-8975.
- [121] E. Taarning, S. Saravanamurugan, M. Spangsborg Holm, J. Xiong, R.M. West, C.H. Christensen, Zeolite-catalyzed isomerization of triose sugars, *ChemSusChem*, 2 (2009) 625-627.
- [122] G. Innocenti, E. Papadopoulos, G. Fornasari, F. Cavani, A.J. Medford, C. Sievers, Continuous liquid-phase upgrading of dihydroxyacetone to lactic acid over metal phosphate catalysts, *ACS Catal.*, 10 (2020) 11936-11950.
- [123] X. Wang, F. Liang, C. Huang, Y. Li, B. Chen, Siliceous tin phosphates as effective bifunctional catalysts for selective conversion of dihydroxyacetone to lactic acid, *Catal. Sci. Technol.*, 6 (2016) 6551-6560.
- [124] A. Takagaki, H. Goto, R. Kikuchi, S.T. Oyama, Silica-supported chromia-titania catalysts for selective formation of lactic acid from a triose in water, *Appl. Catal. A-Gen.*, 570 (2019) 200-208.
- [125] S. Dutta, K.C.-W. Wu, B. Saha, Emerging strategies for breaking the 3D amorphous network of lignin, *Catal. Sci. Technol.*, 4 (2014) 3785-3799.
- [126] J. Zakzeski, P.C. Bruijninx, A.L. Jongerius, B.M. Weckhuysen, The catalytic valorization of lignin for the production of renewable chemicals, *Chem. Rev.*, 110 (2010) 3552-3599.
- [127] E.M. Anderson, R. Katahira, M. Reed, M.G. Resch, E.M. Karp, G.T. Beckham, Y. Román-Leshkov, Reductive catalytic fractionation of corn stover lignin, *ACS Sustain. Chem. Eng.*, 4 (2016) 6940-6950.
- [128] K.L. Deutsch, B.H. Shanks, Hydrodeoxygenation of lignin model compounds over a copper chromite catalyst, *Appl. Catal. A-Gen.*, 447 (2012) 144-150.
- [129] X. Huang, T.I. Korányi, M.D. Boot, E.J. Hensen, Ethanol as capping agent and formaldehyde scavenger for efficient depolymerization of lignin to aromatics, *Green Chem.*, 17 (2015) 4941-4950.
- [130] X. Huang, O.M.M. Gonzalez, J. Zhu, T.I. Korányi, M.D. Boot, E.J. Hensen, Reductive fractionation of woody biomass into lignin monomers and cellulose by tandem metal triflate and Pd/C catalysis, *Green Chem.*, 19 (2017) 175-187.
- [131] K.H. Kim, B.A. Simmons, S. Singh, Catalytic transfer hydrogenolysis of ionic liquid processed biorefinery lignin to phenolic compounds, *Green Chem.*, 19 (2017) 215-224.
- [132] S. Van den Bosch, W. Schutyser, S.-F. Koelewijn, T. Renders, C. Courtin, B. Sels, Tuning the lignin oil OH-content with Ru and Pd catalysts during lignin hydrogenolysis on birch wood, *Chem. Commun.*, 51 (2015) 13158-13161.

- [133] J. Zhang, J. Teo, X. Chen, H. Asakura, T. Tanaka, K. Teramura, N. Yan, A series of NiM (M= Ru, Rh, and Pd) bimetallic catalysts for effective lignin hydrogenolysis in water, *ACS Catal.*, 4 (2014) 1574-1583.
- [134] J.M. Nichols, L.M. Bishop, R.G. Bergman, J.A. Ellman, Catalytic C–O bond cleavage of 2-aryloxy-1-arylethanol and its application to the depolymerization of lignin-related polymers, *J. Am. Chem. Soc.*, 132 (2010) 12554-12555.
- [135] T. Nimmanwudipong, R.C. Runnebaum, D.E. Block, B.C. Gates, Catalytic conversion of guaiacol catalyzed by platinum supported on alumina: Reaction network including hydrodeoxygenation reactions, *Energy Fuels*, 25 (2011) 3417-3427.
- [136] T. Nimmanwudipong, C. Aydin, J. Lu, R.C. Runnebaum, K.C. Brodwater, N.D. Browning, D.E. Block, B.C. Gates, Selective hydrodeoxygenation of guaiacol catalyzed by platinum supported on magnesium oxide, *Catal. Lett.*, 142 (2012) 1190-1196.
- [137] L. Ai, J. Su, M. Wang, J. Jiang, Bamboo-structured nitrogen-doped carbon nanotube coencapsulating cobalt and molybdenum carbide nanoparticles: an efficient bifunctional electrocatalyst for overall water splitting, *ACS Sustain. Chem. Eng.*, 6 (2018) 9912-9920.
- [138] S. Qi, C. Jiaying, J. ZHANG, Y. Weiqiang, W. Feng, X. Jie, Hydrogenation and cleavage of the CO bonds in the lignin model compound phenethyl phenyl ether over a nickel-based catalyst, *Chinese J. Catal.*, 34 (2013) 651-658.
- [139] C. Zhang, J. Lu, X. Zhang, K. MacArthur, M. Heggen, H. Li, F. Wang, Cleavage of the lignin β -O-4 ether bond via a dehydroxylation–hydrogenation strategy over a NiMo sulfide catalyst, *Green Chem.*, 18 (2016) 6545-6555.
- [140] A. Wang, H. Song, Maximizing the production of aromatic hydrocarbons from lignin conversion by coupling methane activation, *Bioresour. Technol.*, 268 (2018) 505-513.
- [141] A. Wang, D. Austin, H. Song, Investigations of thermochemical upgrading of biomass and its model compounds: Opportunities for methane utilization, *Fuel*, 246 (2019) 443-453.
- [142] H. Liu, E. Iglesia, Selective oxidation of methanol and ethanol on supported ruthenium oxide clusters at low temperatures, *J. Phys. Chem. B*, 109 (2005) 2155-2163.
- [143] S. Iqbal, S.A. Kondrat, D.R. Jones, D.C. Schoenmakers, J.K. Edwards, L. Lu, B.R. Yeo, P.P. Wells, E.K. Gibson, D.J. Morgan, Ruthenium nanoparticles supported on carbon: an active catalyst for the hydrogenation of lactic acid to 1, 2-propanediol, *ACS Catal.*, 5 (2015) 5047-5059.
- [144] N.N. Duong, D. Aruho, B. Wang, D.E. Resasco, Hydrodeoxygenation of anisole over different Rh surfaces, *Chinese J. Catal.*, 40 (2019) 1721-1730.
- [145] M.J. Gilkey, P. Panagiotopoulou, A.V. Mironenko, G.R. Jenness, D.G. Vlachos, B. Xu, Mechanistic insights into metal lewis acid-mediated catalytic transfer hydrogenation of furfural to 2-methylfuran, *ACS Catal.*, 5 (2015) 3988-3994.
- [146] A.V. Mironenko, D.G. Vlachos, Conjugation-driven “reverse Mars–van Krevelen”-type radical mechanism for low-temperature C–O bond activation, *J. Am. Chem. Soc.*, 138 (2016) 8104-8113.
- [147] M. Verziu, A. Tirsoaga, B. Cojocaru, C. Bucur, B. Tudora, A. Richel, M. Aguedo, A. Samikannu, J.P. Mikkola, Hydrogenolysis of lignin over Ru-based catalysts: The role of the ruthenium in a lignin fragmentation process, *Mol. Catal.*, 450 (2018) 65-76.
- [148] H. Li, G. Song, Ru-catalyzed hydrogenolysis of lignin: base-dependent tunability of monomeric phenols and mechanistic study, *ACS Catal.*, 9 (2019) 4054-4064.
- [149] S. Aouad, E. Saab, E. Abi-Aad, A. Aboukaïs, Study of the Ru/Ce system in the oxidation of carbon black and volatile organic compounds, *Kinetics and Catalysis*, 48 (2007) 835-840.
- [150] W. Li, H. Liu, E. Iglesia, Structures and properties of zirconia-supported ruthenium oxide catalysts for the selective oxidation of methanol to methyl formate, *J. Phys. Chem. B*, 110 (2006) 23337-23342.
- [151] S. Hosokawa, H. Kanai, K. Utani, Y.-i. Taniguchi, Y. Saito, S. Imamura, State of Ru on CeO₂ and its catalytic activity in the wet oxidation of acetic acid, *Appl. Catal. B: Environ.*, 45 (2003) 181-187.

- [152] P. Betancourt, A. Rives, R. Hubaut, C. Scott, J. Goldwasser, A study of the ruthenium–alumina system, *Appl. Catal. A-Gen.*, 170 (1998) 307-314.
- [153] G. Tauszik, G. Leofanti, S. Galvagno, A TPR and TPO study of bimetallic Ru-Au catalysts, *Journal of molecular catalysis*, 25 (1984) 357-366.
- [154] J. Zheng, S. Meyer, K. Köhler, Abatement of nitrous oxide by ruthenium catalysts: Influence of the support, *Appl. Catal. A-Gen.*, 505 (2015) 44-51.
- [155] T.L. Stuchinskaya, M. Musawir, E.F. Kozhevnikova, I.V. Kozhevnikov, Liquid-phase oxidation of alcohols by oxygen and nitrous oxide catalysed by Ru–Co oxide, *J. Catal.*, 231 (2005) 41-47.
- [156] C. Wang, C. Tian, Y. Guo, Z. Zhang, W. Hua, W. Zhan, Y. Guo, L. Wang, G. Lu, Ruthenium oxides supported on heterostructured CoPO-MCF materials for catalytic oxidation of vinyl chloride emissions, *Journal of hazardous materials*, 342 (2018) 290-296.
- [157] X. Huo, D.J. Van Hoomissen, J. Liu, S. Vyas, T.J. Strathmann, Hydrogenation of aqueous nitrate and nitrite with ruthenium catalysts, *Appl. Catal. B: Environ.*, 211 (2017) 188-198.
- [158] Ž. Petrović, M. Ristić, M. Marciuš, B. Sepiol, H. Peterlik, M. Ivanda, S. Musić, Formation of RuO₂ nanoparticles by thermal decomposition of Ru (NO)(NO₃)₃, *Ceramics International*, 41 (2015) 7811-7815.
- [159] M. Hiratani, Y. Matsui, K. Imagawa, S. Kimura, Growth of RuO₂ thin films by pulsed-laser deposition, *Thin Solid Films*, 366 (2000) 102-106.
- [160] M. Wang, W. Weng, H. Zheng, X. Yi, C. Huang, H. Wan, Oscillations during partial oxidation of methane to synthesis gas over Ru/Al₂O₃ catalyst, *J. Nat. Gas Chem.*, 18 (2009) 300-305.
- [161] J. Chen, J. Li, Y. Zhao, Y. Zhang, J. Hong, Effects of Ru nanoparticle sizes confined in cavities of SBA-16 on the catalytic performance of Fischer-Tropsch synthesis reaction, *J. Nat. Gas Chem.*, 21 (2012) 673-679.
- [162] J. Kang, S. Zhang, Q. Zhang, Y. Wang, Ruthenium nanoparticles supported on carbon nanotubes as efficient catalysts for selective conversion of synthesis gas to diesel fuel, *Angew. Chem. Int. Ed.*, 48 (2009) 2565-2568.
- [163] L. Dong, L.-L. Yin, Q. Xia, X. Liu, X.-Q. Gong, Y. Wang, Size-dependent catalytic performance of ruthenium nanoparticles in the hydrogenolysis of a β-O-4 lignin model compound, *Catal. Sci. Technol.*, 8 (2018) 735-745.
- [164] S. Ren, F. Huang, J. Zheng, S. Chen, H. Zhang, Ruthenium supported on nitrogen-doped ordered mesoporous carbon as highly active catalyst for NH₃ decomposition to H₂, *International Journal of Hydrogen Energy*, 42 (2017) 5105-5113.
- [165] B.D. Cullity, *Elements of X-ray Diffraction*, Addison-Wesley Publishing 1956.
- [166] R. Barton, M. Carrier, C. Segura, J.G. Fierro, S. Park, H. Lamb, N. Escalona, S. Peretti, Ni/HZSM-5 catalyst preparation by deposition-precipitation. Part 2. Catalytic hydrodeoxygenation reactions of lignin model compounds in organic and aqueous systems, *Appl. Catal. A-Gen.*, 562 (2018) 294-309.
- [167] Y. Cao, R. Ma, N. Wang, M.-Y. Wang, X.-D. Li, L.-N. He, Selective hydrodeoxygenation of lignin β-O-4 model compounds and aromatic ketones promoted by palladium chloride with acidic CO₂/MeOH system, *J. CO₂ Util.*, 24 (2018) 328-333.
- [168] S. Wendt, M. Knapp, H. Over, The role of weakly bound on-top oxygen in the catalytic CO oxidation reaction over RuO₂ (110), *J. Am. Chem. Soc.*, 126 (2004) 1537-1541.
- [169] A. Bjelić, M. Grilc, M. Huš, B. Likozar, Hydrogenation and hydrodeoxygenation of aromatic lignin monomers over Cu/C, Ni/C, Pd/C, Pt/C, Rh/C and Ru/C catalysts: Mechanisms, reaction micro-kinetic modelling and quantitative structure-activity relationships, *Chem. Eng. J.*, 359 (2019) 305-320.
- [170] D. Liu, Y.M. López-De Jesús, J.R. Monnier, C.T. Williams, Preparation, characterization, and kinetic evaluation of dendrimer-derived bimetallic Pt–Ru/SiO₂ catalysts, *J. Catal.*, 269 (2010) 376-387.

- [171] J.K. Nørskov, J. Rossmeisl, A. Logadottir, L. Lindqvist, J.R. Kitchin, T. Bligaard, H. Jonsson, Origin of the overpotential for oxygen reduction at a fuel-cell cathode, *J. Phys. Chem. B*, 108 (2004) 17886-17892.
- [172] J. Jae, W. Zheng, A.M. Karim, W. Guo, R.F. Lobo, D.G. Vlachos, The Role of Ru and RuO₂ in the Catalytic Transfer Hydrogenation of 5-Hydroxymethylfurfural for the Production of 2, 5-Dimethylfuran, *ChemCatChem*, 6 (2014) 848-856.
- [173] Y. Zhang, J. Yu, H. Niu, H. Liu, Synthesis of PVP-stabilized ruthenium colloids with low boiling point alcohols, *J. Colloid Interface Sci.*, 313 (2007) 503-510.
- [174] C. Cheng, D. Shen, S. Gu, K.H. Luo, State-of-the-art catalytic hydrogenolysis of lignin for the production of aromatic chemicals, *Catal. Sci. Technol.*, 8 (2018) 6275-6296.
- [175] J. Garcia, H. Gomes, P. Serp, P. Kalck, J. Figueiredo, J. Faria, Carbon nanotube supported ruthenium catalysts for the treatment of high strength wastewater with aniline using wet air oxidation, *Carbon*, 44 (2006) 2384-2391.
- [176] F. Michalek, D. Mädege, J. Rühe, W. Bannwarth, The activity of covalently immobilized Grubbs–Hoveyda type catalyst is highly dependent on the nature of the support material, *Journal of organometallic chemistry*, 691 (2006) 5172-5180.
- [177] M. Besson, P. Gallezot, Deactivation of metal catalysts in liquid phase organic reactions, *Catal. Today*, 81 (2003) 547-559.
- [178] N. Grosjean, C. Descorme, M. Besson, Catalytic wet air oxidation of N, N-dimethylformamide aqueous solutions: deactivation of TiO₂ and ZrO₂-supported noble metal catalysts, *Appl. Catal. B: Environ.*, 97 (2010) 276-283.
- [179] L. Hu, H. Pan, Y. Zhou, M. Zhang, Methods to Improve Lignin's Reactivity as a Phenol Substitute and as Replacement for Other Phenolic Compounds: A Brief Review, *Bioresour.*, 6 (2011) 3515–3525.
- [180] R. Gosselink, E. De Jong, B. Guran, A. Abächerli, Co-ordination network for lignin—standardisation, production and applications adapted to market requirements (EUROLIGNIN), *Ind. Crops Prod.*, 20 (2004) 121-129.
- [181] J.H. Lora, W.G. Glasser, Recent Industrial Applications of Lignin: A Sustainable Alternative to Nonrenewable Materials, *J. Polym. Environ.*, 10 (2002) 39-48.
- [182] S.-H. Lee, Y. Teramoto, N. Shiraishi, Resol-type phenolic resin from liquefied phenolated wood and its application to phenolic foam, *J. Appl. Polym. Sci.*, 84 (2002) 468-472.
- [183] P.K. Mishra, R. Wimmer, Aerosol assisted self-assembly as a route to synthesize solid and hollow spherical lignin colloids and its utilization in layer by layer deposition, *Ultrason. Sonochem.*, 35 (2017) 45-50.
- [184] M.N. Collins, M. Nechifor, F. Tanasă, M. Zănoagă, A. McLoughlin, M.A. Strózyk, M. Culebras, C.-A. Teacă, Valorization of lignin in polymer and composite systems for advanced engineering applications – A review, *Int. J. Biol. Macromol.*, 131 (2019) 828-849.
- [185] S.R. Yearla, K. Padmasree, Preparation and characterisation of lignin nanoparticles: evaluation of their potential as antioxidants and UV protectants, *J. Exp. Nanosci.*, 11 (2016) 289-302.
- [186] Y. Qian, X. Qiu, X. Zhong, D. Zhang, Y. Deng, D. Yang, S. Zhu, Lignin Reverse Micelles for UV-Absorbing and High Mechanical Performance Thermoplastics, *Ind. Eng. Chem. Res.*, 54 (2015) 12025-12030.
- [187] Y. Zhu, Z. Han, L. Fu, C. Liu, D. Zhang, Cleavage of the β -O-4 bond in a lignin model compound using the acidic ionic liquid 1-H-3-methylimidazolium chloride as catalyst: a DFT mechanistic study, *J. Mol. Model.*, 24 (2018) 322.
- [188] J. Zakzeski, P.C.A. Bruijninx, A.L. Jongorius, B.M. Weckhuysen, The Catalytic Valorization of Lignin for the Production of Renewable Chemicals, *Chem. Rev.*, 110 (2010) 3552-3599.
- [189] J. Zhang, X. Jiang, X. Ye, L. Chen, Q. Lu, X. Wang, C. Dong, Pyrolysis mechanism of a β -O-4 type lignin dimer model compound, *J. Therm. Anal. Calorim.*, 123 (2016) 501-510.

- [190] J. Lu, M. Wang, X. Zhang, A. Heyden, F. Wang, β -O-4 bond cleavage mechanism for lignin model compounds over Pd catalysts identified by combination of first-principles calculations and experiments, *ACS Catal.*, 6 (2016) 5589-5598.
- [191] C. Zhang, J. Lu, X. Zhang, K. MacArthur, M. Heggen, H. Li, F. Wang, Cleavage of the lignin β -O-4 ether bond via a dehydroxylation-hydrogenation strategy over a NiMo sulfide catalyst, *Green Chem.*, 18 (2016) 6545-6555.
- [192] W. Deng, H. Zhang, L. Xue, Q. Zhang, Y. Wang, Selective activation of the C–O bonds in lignocellulosic biomass for the efficient production of chemicals, *Chinese J. Catal.*, 36 (2015) 1440-1460.
- [193] M. Zaheer, R. Kempe, Catalytic Hydrogenolysis of Aryl Ethers: A Key Step in Lignin Valorization to Valuable Chemicals, *ACS Catal.*, 5 (2015) 1675-1684.
- [194] Z. Luo, C. Zhao, Mechanistic insights into selective hydrodeoxygenation of lignin-derived β -O-4 linkage to aromatic hydrocarbons in water, *Catal. Sci. Technol.*, 6 (2016) 3476-3484.
- [195] Z. Luo, Y. Wang, M. He, C. Zhao, Precise oxygen scission of lignin derived aryl ethers to quantitatively produce aromatic hydrocarbons in water, *Green Chem.*, 18 (2016) 433-441.
- [196] C.S. Lancefield, O.S. Ojo, F. Tran, N.J. Westwood, Isolation of functionalized phenolic monomers through selective oxidation and C-O bond cleavage of the beta-O-4 linkages in lignin, *Angew Chem Int Ed Engl*, 54 (2015) 258-262.
- [197] B. Gómez-Monedero, M.P. Ruiz, F. Bimbela, J. Faria, Selective hydrogenolysis of α -O-4, β -O-4, 4-O-5 C-O bonds of lignin-model compounds and lignin-containing stillage derived from cellulosic bioethanol processing, *Appl. Catal. A*, 541 (2017) 60-76.
- [198] A.L. Jongerius, R. Jastrzebski, P.C.A. Bruijninx, B.M. Weckhuysen, CoMo sulfide-catalyzed hydrodeoxygenation of lignin model compounds: An extended reaction network for the conversion of monomeric and dimeric substrates, *J. Catal.*, 285 (2012) 315-323.
- [199] J. Zhang, G. Lu, C. Cai, Self-hydrogen transfer hydrogenolysis of β -O-4 linkages in lignin catalyzed by MIL-100(Fe) supported Pd-Ni BMNPs, *Green Chem.*, 19 (2017) 4538-4543.
- [200] J. Zhang, J. Teo, X. Chen, H. Asakura, T. Tanaka, K. Teramura, N. Yan, A Series of NiM (M = Ru, Rh, and Pd) Bimetallic Catalysts for Effective Lignin Hydrogenolysis in Water, *ACS Catal.*, 4 (2014) 1574-1583.
- [201] H. Wang, Y. Pu, A. Ragauskas, B. Yang, From lignin to valuable products—strategies, challenges, and prospects, *Bioresour. Technol.*, 271 (2019) 449-461.
- [202] M.A. Hossain, T.K. Phung, M.S. Rahaman, S. Tulaphol, J.B. Jasinski, N. Sathitsuksanoh, Catalytic cleavage of the β -O-4 aryl ether bonds of lignin model compounds by Ru/C catalyst, *Appl. Catal. A*, 582 (2019) 117100.
- [203] J. Hicks, Advances in C–O bond transformations in lignin-derived compounds for biofuels production, *J. Phys. Chem. Lett.*, 2 (2011) 2280-2287.
- [204] A.L. Marshall, P. Alaimo, Useful products from complex starting materials: common chemicals from biomass feedstocks, *Chem. Eur. J.*, 16 (2010) 4970-4980.
- [205] D.-P. Phan, E. Lee, Controlled hydrogenolysis over heterogeneous catalysts for lignin valorization, *Catal. Rev.*, 62 (2020) 607-630.
- [206] J. Zakzeski, P. Bruijninx, A. Jongerius, B. Weckhuysen, The catalytic valorization of lignin for the production of renewable chemicals, *Chem. Rev.*, 110 (2010) 3552-3599.
- [207] M.A. Dasari, P.-P. Kiatsimkul, W.R. Sutterlin, G.J. Suppes, Low-pressure hydrogenolysis of glycerol to propylene glycol, *Appl. Catal., A*, 281 (2005) 225-231.
- [208] I. Gandarias, P. Arias, J. Requies, M. El Doukkali, M. Güemez, Liquid-phase glycerol hydrogenolysis to 1, 2-propanediol under nitrogen pressure using 2-propanol as hydrogen source, *J. Catal.*, 282 (2011) 237-247.
- [209] Y. Wu, Z. Lin, X. Zhu, X. Hu, M. Gholizadeh, H. Sun, Y. Huang, S. Zhang, H. Zhang, Hydrogenolysis of lignin to phenolic monomers over Ru based catalysts with different metal-support interactions: Effect of partial hydrogenation of C (sp²)-O/C, *Fuel*, 302 (2021) 121184.

- [210] J.-P. Cao, T. Xie, X.-Y. Zhao, C. Zhu, W. Jiang, M. Zhao, Y.-P. Zhao, X.-Y. Wei, Selective cleavage of ether CO bond in lignin-derived compounds over Ru system under different H-sources, *Fuel*, 284 (2021) 119027.
- [211] S. Van den Bosch, W. Schutyser, S.-F. Koelewijn, T. Renders, C. Courtin, B. Sels, Tuning the lignin oil OH-content with Ru and Pd catalysts during lignin hydrogenolysis on birch wood, *Chem. Commun.*, 51 (2015) 13158-13161.
- [212] J. Luterbacher, A. Azarpira, A. Motagamwala, F. Lu, J. Ralph, J. Dumesic, Lignin monomer production integrated into the γ -valerolactone sugar platform, *Energy Environ. Sci.*, 8 (2015) 2657-2663.
- [213] L.-P. Xiao, S. Wang, H. Li, Z. Li, Z.-J. Shi, L. Xiao, R.-C. Sun, Y. Fang, G. Song, Catalytic hydrogenolysis of lignins into phenolic compounds over carbon nanotube supported molybdenum oxide, *ACS Catal.*, 7 (2017) 7535-7542.
- [214] H. Wu, J. Song, C. Xie, C. Wu, C. Chen, B. Han, Efficient and mild transfer hydrogenolytic cleavage of aromatic ether bonds in lignin-derived compounds over Ru/C, *ACS Sustain. Chem. Eng.*, 6 (2018) 2872-2877.
- [215] H. Li, G. Song, Ru-catalyzed hydrogenolysis of lignin: base-dependent tunability of monomeric phenols and mechanistic study, *ACS Catal.*, 9 (2019) 4054-4064.
- [216] Y. Liu, N. Deak, Z. Wang, H. Yu, L. Hameleers, E. Jurak, P. Deuss, K. Barta, Tunable and functional deep eutectic solvents for lignocellulose valorization, *Nat. Commun.*, 12 (2021) 1-15.
- [217] W. Deng, H. Zhang, X. Wu, R. Li, Q. Zhang, Y. Wang, Oxidative conversion of lignin and lignin model compounds catalyzed by CeO₂-supported Pd nanoparticles, *Green Chem.*, 17 (2015) 5009-5018.
- [218] J. Zhang, H. Asakura, J. van Rijn, J. Yang, P. Duchesne, B. Zhang, X. Chen, P. Zhang, M. Saeys, N. Yan, Highly efficient, NiAu-catalyzed hydrogenolysis of lignin into phenolic chemicals, *Green Chem.*, 16 (2014) 2432-2437.
- [219] W. Guan, X. Chen, H. Hu, C.-W. Tsang, J. Zhang, C. Lin, C. Liang, Catalytic hydrogenolysis of lignin β -O-4 aryl ether compound and lignin to aromatics over Rh/Nb₂O₅ under low H₂ pressure, *Fuel Process. Technol.*, 203 (2020) 106392.
- [220] L. Jiang, H. Guo, C. Li, P. Zhou, Z. Zhang, Selective cleavage of lignin and lignin model compounds without external hydrogen, catalyzed by heterogeneous nickel catalysts, *Chem. Sci.*, 10 (2019) 4458-4468.
- [221] M. Klein, P. Virk, Model pathways in lignin thermolysis. 1. Phenethyl phenyl ether, *Ind. Eng. Chem. Fundam.*, 22 (1983) 35-45.
- [222] A. Enoki, G. Goldsby, M. Gold, Metabolism of the lignin model compounds veratrylglycerol- β -guaiacyl ether and 4-ethoxy-3-methoxyphenylglycerol- β -guaiacyl ether by *Phanerochaete chrysosporium*, *Arch. Microbiol.*, 125 (1980) 227-231.
- [223] B. Cox, J. Ekerdt, Depolymerization of oak wood lignin under mild conditions using the acidic ionic liquid 1-H-3-methylimidazolium chloride as both solvent and catalyst, *Biores. Technol.*, 118 (2012) 584-588.
- [224] S. Jia, B. Cox, X. Guo, Z. Zhang, J. Ekerdt, Hydrolytic cleavage of β -O-4 ether bonds of lignin model compounds in an ionic liquid with metal chlorides, *Ind. Eng. Chem. Res.*, 50 (2011) 849-855.
- [225] D.J. Yelle, J. Ralph, C.R. Frihart, Characterization of nonderivatized plant cell walls using high-resolution solution-state NMR spectroscopy, *Magn. Reson. Chem.*, 46 (2008) 508-517.
- [226] G. Kresse, J. Hafner, Ab initio molecular-dynamics simulation of the liquid-metal–amorphous-semiconductor transition in germanium, *Phys. Rev. B: Condens. Matter*, 49 (1994) 14251.
- [227] G. Kresse, J. Furthmüller, Efficient iterative schemes for ab initio total-energy calculations using a plane-wave basis set, *Phys. Rev. B: Condens. Matter*, 54 (1996) 11169.
- [228] G. Kresse, J. Hafner, Ab initio molecular dynamics for liquid metals, *Phys. Rev. B: Condens. Matter*, 47 (1993) 558.

- [229] J. Hafner, Materials simulations using VASP—a quantum perspective to materials science, *Comput. Phys. Commun.*, 177 (2007) 6-13.
- [230] Y.-R. Luo, *Comprehensive Handbook of Chemical Bond Energies*, 1st Edition ed.2007.
- [231] G. Zhu, X. Ouyang, L. Jiang, Y. Zhu, D. Jin, Y. Pang, X. Qiu, Effect of functional groups on hydrogenolysis of lignin model compounds, *Fuel Process. Technol.*, 154 (2016) 132-138.
- [232] C. Zhang, J. Lu, X. Zhang, K. MacArthur, M. Heggen, H. Li, F. Wang, Cleavage of the lignin β -O-4 ether bond via a dehydroxylation–hydrogenation strategy over a NiMo sulfide catalyst, *Green Chem*, 18 (2016) 6545-6555.
- [233] B. Shumeiko, D. Kubička, Semi-Batch Hydrotreatment of Lignin-Derived Phenolic Compounds over Raney-Ni with a Continuous Regeneration of the H-Donor Solvent, *ChemSusChem*, 15 (2022) e202102099.
- [234] L. Jiang, H. Guo, C. Li, P. Zhou, Z. Zhang, Selective cleavage of lignin and lignin model compounds without external hydrogen, catalyzed by heterogeneous nickel catalysts, *Chem. Sci.*, 10 (2019) 4458-4468.
- [235] K. Cui, X. Zhao, Q. Peng, H. Gong, X. Wei, J. Wang, M. Chen, Z. Hou, Catalytic transfer hydrogenolysis of C–O bonds in lignin model compounds without arene hydrogenation, *Green Chemical Engineering*, 3 (2022) 25-33.
- [236] X. Wang, R. Rinaldi, Solvent effects on the hydrogenolysis of diphenyl ether with Raney nickel and their implications for the conversion of lignin, *ChemSusChem*, 5 (2012) 1455-1466.
- [237] E. Adler, Structural elements of lignin, *Ind. Eng. Chem.*, 49 (1957) 1377-1383.
- [238] S. Guadix-Montero, M. Sankar, Review on catalytic cleavage of C–C inter-unit linkages in lignin model compounds: towards lignin depolymerisation, *Top. Catal.*, 61 (2018) 183-198.
- [239] J. Fernández-Rodríguez, X. Erdocia, C. Sánchez, M.G. Alriols, J. Labidi, Lignin depolymerization for phenolic monomers production by sustainable processes, *J. Energy Chem.*, 26 (2017) 622-631.
- [240] Q. Wang, T. Su, Y. Wang, Y. Chen, X. Lu, R. Ma, Y. Fu, W. Zhu, Metal–Organic Framework-Mediated Synthesis of One-Dimensional Nitrogen-Doped Molybdenum Carbide for the Cleavage of Lignin and Dimeric Lignin Model Compounds, *ACS Sustain. Chem. Eng.*, 8 (2020) 17008-17015.
- [241] C.G. Visconti, L. Lietti, P. Forzatti, R. Zennaro, Fischer–Tropsch synthesis on sulphur poisoned Co/Al₂O₃ catalyst, *Appl. Catal. A-Gen.*, 330 (2007) 49-56.
- [242] J. Jones, V. Dupont, R. Brydson, D. Fullerton, N. Nasri, A. Ross, A. Westwood, Sulphur poisoning and regeneration of precious metal catalysed methane combustion, *Catal. Today.*, 81 (2003) 589-601.
- [243] J. Hepola, P. Simell, Sulphur poisoning of nickel-based hot gas cleaning catalysts in synthetic gasification gas: I. Effect of different process parameters, *Appl. Catal. B: Environ.*, 14 (1997) 287-303.
- [244] A. Shivhare, D. Jampaiah, S. Bhargava, A. Lee, R. Srivastava, K. Wilson, Hydrogenolysis of Lignin-Derived Aromatic Ethers over Heterogeneous Catalysts, *ACS Sustain. Chem. Eng.*, 9 (2021) 3379-3407.
- [245] M.J. Gilkey, P. Panagiotopoulou, A.V. Mironenko, G.R. Jenness, D.G. Vlachos, B. Xu, Mechanistic Insights into Metal Lewis Acid-Mediated Catalytic Transfer Hydrogenation of Furfural to 2-Methylfuran, *ACS Catal.*, 5 (2015) 3988-3994.
- [246] M.A. Hossain, T.K. Phung, M.S. Rahaman, S. Tulaphol, J.B. Jasinski, N. Sathitsuksanoh, Catalytic cleavage of the β -O-4 aryl ether bonds of lignin model compounds by Ru/C catalyst, *Appl. Catal., A*, DOI: 10.1016/j.apcata.2019.05.034 (2019).
- [247] P. Panagiotopoulou, N. Martin, D.G. Vlachos, Effect of hydrogen donor on liquid phase catalytic transfer hydrogenation of furfural over a Ru/RuO₂/C catalyst, *J. Mol. Catal. A: Chem.*, 392 (2014) 223-228.
- [248] A.V. Mironenko, D.G. Vlachos, Conjugation-Driven “Reverse Mars–van Krevelen”-Type Radical Mechanism for Low-Temperature C–O Bond Activation, *JACS*, 138 (2016) 8104-8113.

- [249] G. Jenness, D. Vlachos, DFT study of the conversion of furfuryl alcohol to 2-methylfuran on RuO₂ (110), *J. Phys. Chem. C*, 119 (2015) 5938-5945.
- [250] Y. Zeng, Z. Wang, W. Lin, W. Song, In situ hydrodeoxygenation of phenol with liquid hydrogen donor over three supported noble-metal catalysts, *Chem. Eng. J.*, 320 (2017) 55-62.
- [251] T. Walker, A. Motagamwala, J. Dumesic, G. Huber, Fundamental catalytic challenges to design improved biomass conversion technologies, *J. Catal.*, 369 (2018).
- [252] N. Luo, M. Wang, H. Li, J. Zhang, T. Hou, H. Chen, X. Zhang, J. Lu, F. Wang, Visible-light-driven self-hydrogen transfer hydrogenolysis of lignin models and extracts into phenolic products, *ACS Catal.*, 7 (2017) 4571-4580.
- [253] M.A. Hossain, T.K. Phung, M.S. Rahaman, S. Tulaphol, J.B. Jasinski, N. Sathitsuksanoh, Catalytic cleavage of the β -O-4 aryl ether bonds of lignin model compounds by Ru/C catalyst, *Appl. Catal. A-Gen.*, 582 (2019) 117100.
- [254] X. Zhou, J. Mitra, T.B. Rauchfuss, Lignol Cleavage by Pd/C Under Mild Conditions and Without Hydrogen: A Role for Benzylic C-H Activation?, *ChemSusChem*, 7 (2014) 1623-1626.
- [255] A. de Andrade, P. Srifa, P. Broqvist, K. Hermansson, Lignin Intermediates on Palladium: Insights into Keto-Enol Tautomerization from Theoretical Modelling, *ChemSusChem*, 13 (2020) 6574-6581.
- [256] A. Rahimi, A. Ulbrich, J. Coon, S. Stahl, Formic-acid-induced depolymerization of oxidized lignin to aromatics, *Nature*, 515 (2014) 249-252.
- [257] J. Nguyen, B. Matsuura, C. Stephenson, A photochemical strategy for lignin degradation at room temperature, *JACS*, 136 (2014) 1218-1221.
- [258] W. Kohn, L.J. Sham, Self-Consistent Equations Including Exchange and Correlation Effects, *Phys. Rev.*, 140 (1965) A1133-A1138.
- [259] G. Kresse, J. Furthmüller, Efficient iterative schemes for ab initio total-energy calculations using a plane-wave basis set, *Phys. Rev. B.*, 54 (1996) 11169.
- [260] G. Kresse, J. Hafner, Ab initio molecular dynamics for liquid metals, *Phys. Rev. B.*, 47 (1993) 558.
- [261] P.E. Blöchl, Projector augmented-wave method, *Phys. Rev. B.*, 50 (1994) 17953-17979.
- [262] G. Kresse, D. Joubert, From ultrasoft pseudopotentials to the projector augmented-wave method, *Phys. Rev. B.*, 59 (1999) 1758-1775.
- [263] J.P. Perdew, K. Burke, M. Ernzerhof, Generalized Gradient Approximation Made Simple, *Phys. Rev. Lett.*, 77 (1996) 3865-3868.
- [264] H.J. Monkhorst, J.D. Pack, Special points for Brillouin-zone integrations, *Phys. Rev. B.*, 13 (1976) 5188.
- [265] M.P. Teter, M.C. Payne, D.C. Allan, Solution of Schrödinger's equation for large systems, *Phys. Rev. B.*, 40 (1989) 12255.
- [266] M. Methfessel, A.T. Paxton, High-precision sampling for Brillouin-zone integration in metals, *Phys. Rev. B.*, 40 (1989) 3616-3621.
- [267] S. Grimme, J. Antony, S. Ehrlich, H. Krieg, A consistent and accurate ab initio parametrization of density functional dispersion correction (DFT-D) for the 94 elements H-Pu, *J. Chem. Phys.*, 132 (2010) 154104.
- [268] Y. Nanba, T. Ishimoto, M. Koyama, Structural Stability of Ruthenium Nanoparticles: A Density Functional Theory Study, *J. Phys. Chem. C*, 121 (2017) 27445-27452.
- [269] M. Boulbazine, A.-G. Boudjahem, S. Chaguetmi, A. Karaman, Stability and electronic properties of Rh-doped ruthenium clusters and their interaction with NH₃ molecule, *Mol. Phys.*, 118 (2020) e1643511.
- [270] S. Shetty, A.P.J. Jansen, R.A. van Santen, Methane Formation on Corrugated Ru Surfaces, *J. Phys. Chem. C*, 114 (2010) 22630-22635.
- [271] G. Henkelman, A. Arnaldsson, H. Jónsson, A fast and robust algorithm for Bader decomposition of charge density, *Comput. Mater. Sci.*, 36 (2006) 354-360.

- [272] W. Tang, E. Sanville, G. Henkelman, A grid-based Bader analysis algorithm without lattice bias, *J. Phys. Condens. Matter.*, 21 (2009) 084204.
- [273] S. Edward, K.S. D., S. Roger, H. Graeme, Improved grid-based algorithm for Bader charge allocation, *J. Comput. Chem.*, 28 (2007) 899-908.
- [274] M. Yu, D.R. Trinkle, Accurate and efficient algorithm for Bader charge integration, *J. Chem. Phys.*, 134 (2011) 064111.
- [275] K.-i. Fujita, T. Yoshida, Y. Imori, R. Yamaguchi, Dehydrogenative oxidation of primary and secondary alcohols catalyzed by a Cp* Ir complex having a functional C, N-chelate ligand, *Org. Lett.*, 13 (2011) 2278-2281.
- [276] Y. Ukisu, T. Miyadera, Dehydrogenation of 2-propanol with suspended noble metal catalysts: activity enhancement by the addition of sodium hydroxide, *React. Kinet. Catal. Lett.*, 81 (2004) 305-311.
- [277] J. Desilvestro, O. Haas, Metal oxide cathode materials for electrochemical energy storage: a review, *J. Electrochem. Soc.*, 137 (1990) 5C.
- [278] Y. Liang, C.Z. Zhao, H. Yuan, Y. Chen, W. Zhang, J.Q. Huang, D. Yu, Y. Liu, M.M. Titirici, Y.L. Chueh, H. Yu, Q. Zhang, A review of rechargeable batteries for portable electronic devices, *InfoMat*, 1 (2019) 6-32.
- [279] J. Xu, J. Ma, Q. Fan, S. Guo, S. Dou, Recent progress in the design of advanced cathode materials and battery models for high-performance lithium-X (X= O₂, S, Se, Te, I₂, Br₂) batteries, *Adv. Mater.*, 29 (2017) 1606454.
- [280] Y.X. Yao, X.Q. Zhang, B.Q. Li, C. Yan, P.Y. Chen, J.Q. Huang, Q. Zhang, A compact inorganic layer for robust anode protection in lithium-sulfur batteries, *InfoMat*, 2 (2020) 379-388.
- [281] Z. Wei, Y. Ren, J. Sokolowski, X. Zhu, G. Wu, Mechanistic understanding of the role separators playing in advanced lithium-sulfur batteries, *InfoMat*, 2 (2020) 483-508.
- [282] Y. Zhang, P. Zhang, S. Zhang, Z. Wang, N. Li, S.R.P. Silva, G. Shao, A flexible metallic TiC nanofiber/vertical graphene 1D/2D heterostructured as active electrocatalyst for advanced Li-S batteries, *InfoMat*, 3 (2021) 790-803.
- [283] C. Luo, Y. Xu, Y. Zhu, Y. Liu, S. Zheng, Y. Liu, A. Langrock, C. Wang, Selenium@mesoporous carbon composite with superior lithium and sodium storage capacity, *ACS nano*, 7 (2013) 8003-8010.
- [284] D. Peramunage, S. Licht, A solid sulfur cathode for aqueous batteries, *Science*, 261 (1993) 1029-1032.
- [285] J. Nelson, S. Misra, Y. Yang, A. Jackson, Y. Liu, H. Wang, H. Dai, J.C. Andrews, Y. Cui, M.F. Toney, In operando X-ray diffraction and transmission X-ray microscopy of lithium sulfur batteries, *J. Am. Chem. Soc.*, 134 (2012) 6337-6343.
- [286] X. Ji, K.T. Lee, L.F. Nazar, A highly ordered nanostructured carbon-sulphur cathode for lithium-sulphur batteries, *Nat. Mater.*, 8 (2009) 500-506.
- [287] S.S. Zhang, Liquid electrolyte lithium/sulfur battery: Fundamental chemistry, problems, and solutions, *J. Power Sources*, 231 (2013) 153-162.
- [288] A. Abouimrane, D. Dambournet, K.W. Chapman, P.J. Chupas, W. Weng, K. Amine, A new class of lithium and sodium rechargeable batteries based on selenium and selenium-sulfur as a positive electrode, *J. Am. Chem. Soc.*, 134 (2012) 4505-4508.
- [289] Y. Cui, A. Abouimrane, J. Lu, T. Bolin, Y. Ren, W. Weng, C. Sun, V. Maroni, S. Heald, K. Amine, (De) Lithiation mechanism of Li/SeS_x (x= 0-7) batteries determined by in situ synchrotron X-ray diffraction and X-ray absorption spectroscopy, *J. Am. Chem. Soc.*, 135 (2013) 8047-8056.
- [290] C.P. Yang, S. Xin, Y.X. Yin, H. Ye, J. Zhang, Y.G. Guo, An advanced selenium-carbon cathode for rechargeable lithium-selenium batteries, *Angew. Chem. Int. Ed.*, 52 (2013) 8363-8367.
- [291] A. Eftekhari, The rise of lithium-selenium batteries, *Sustain. Energy Fuels*, 1 (2017) 14-29.

- [292] H. Tian, H. Tian, S. Wang, S. Chen, F. Zhang, L. Song, H. Liu, J. Liu, G. Wang, High-power lithium–selenium batteries enabled by atomic cobalt electrocatalyst in hollow carbon cathode, *Nat. Commun.*, 11 (2020) 1-12.
- [293] C. Fang, S. Yang, X. Zhao, P. Du, J. Xiong, Electrospun montmorillonite modified poly (vinylidene fluoride) nanocomposite separators for lithium-ion batteries, *Mater. Res. Bull.*, 79 (2016) 1-7.
- [294] H. Xu, D. Li, Y. Liu, Y. Jiang, F. Li, B. Xue, Preparation of halloysite/polyvinylidene fluoride composite membrane by phase inversion method for lithium ion battery, *J. Alloys Compd.*, 790 (2019) 305-315.
- [295] W. Fan, L. Zhang, T. Liu, Multifunctional second barrier layers for lithium–sulfur batteries, *Mater. Chem. Front.*, 2 (2018) 235-252.
- [296] Y. Pan, S. Chou, H.K. Liu, S.X. Dou, Functional membrane separators for next-generation high-energy rechargeable batteries, *Natl. Sci. Rev.*, 4 (2017) 917-933.
- [297] F. Zhang, X. Guo, P. Xiong, J. Zhang, J. Song, K. Yan, X. Gao, H. Liu, G. Wang, Interface Engineering of MXene Composite Separator for High-Performance Li–Se and Na–Se Batteries, *Adv. Energy Mater.*, 10 (2020) 2000446.
- [298] C.Z. Zhao, X.Q. Zhang, X.B. Cheng, R. Zhang, R. Xu, P.Y. Chen, H.J. Peng, J.Q. Huang, Q. Zhang, An anion-immobilized composite electrolyte for dendrite-free lithium metal anodes, *PNAS*, 114 (2017) 11069-11074.
- [299] A.J. Cairns, J. Eckert, L. Wojtas, M. Thommes, D. Wallacher, P.A. Georgiev, P.M. Forster, Y. Belmabkhout, J. Ollivier, M. Eddaoudi, Gaining Insights on the H₂–Sorbent Interactions: Robust soc-MOF Platform as a Case Study, *Chem. Mater.*, 28 (2016) 7353-7361.
- [300] A. Kirchon, J. Li, F. Xia, G.S. Day, B. Becker, W. Chen, H.J. Sue, Y. Fang, H.C. Zhou, Modulation versus Templating: Fine-Tuning of Hierarchally Porous PCN-250 Using Fatty Acids To Engineer Guest Adsorption, *Angew. Chem. Int. Ed.*, 58 (2019) 12425-12430.
- [301] Y. Chen, Z. Qiao, H. Wu, D. Lv, R. Shi, Q. Xia, J. Zhou, Z. Li, An ethane-trapping MOF PCN-250 for highly selective adsorption of ethane over ethylene, *Chem. Eng. Sci.*, 175 (2018) 110-117.
- [302] A. Kirchon, G.S. Day, Y. Fang, S. Banerjee, O.K. Ozdemir, H.C. Zhou, Suspension processing of microporous metal-organic frameworks: a scalable route to high-quality adsorbents, *iScience*, 5 (2018) 30-37.
- [303] S. Yuan, X. Sun, J. Pang, C. Lollar, J.S. Qin, Z. Perry, E. Joseph, X. Wang, Y. Fang, M. Bosch, PCN-250 under pressure: sequential phase transformation and the implications for MOF densification, *Joule*, 1 (2017) 806-815.
- [304] J.T. Lee, Y. Zhao, H. Kim, W.I. Cho, G. Yushin, Sulfur infiltrated activated carbon cathodes for lithium sulfur cells: the combined effects of pore size distribution and electrolyte molarity, *J. Power Sources*, 248 (2014) 752-761.
- [305] Z. Li, L. Yuan, Z. Yi, Y. Liu, Y. Huang, Confined selenium within porous carbon nanospheres as cathode for advanced Li–Se batteries, *Nano Energy*, 9 (2014) 229-236.
- [306] J.N. Hall, P. Bollini, Metal–Organic Framework MIL-100 Catalyzed Acetalization of Benzaldehyde with Methanol: Lewis or Brønsted Acid Catalysis?, *ACS Catal.*, 10 (2020) 3750-3763.
- [307] X.X. Zheng, Z.P. Fang, Z.J. Dai, J.M. Cai, L.J. Shen, Y.F. Zhang, C.T. Au, L.L. Jiang, Iron-Based Metal–Organic Frameworks as Platform for H₂S Selective Conversion: Structure-Dependent Desulfurization Activity, *Inorg. Chem.*, 59 (2020) 4483-4492.
- [308] C. Volkringer, H. Leclerc, J.C. Lavalley, T. Loiseau, G. Ferey, M. Daturi, A. Vimont, Infrared spectroscopy investigation of the acid sites in the metal–organic framework aluminum trimesate MIL-100 (Al), *J. Phys. Chem. C*, 116 (2012) 5710-5719.
- [309] A.I. Osman, J.K. Abu-Dahrieh, D.W. Rooney, S.A. Halawy, M.A. Mohamed, A. Abdelkader, Effect of precursor on the performance of alumina for the dehydration of methanol to dimethyl ether, *Appl. Catal., B*, 127 (2012) 307-315.

- [310] K.M.A. Santos, E.M. Albuquerque, G. Innocenti, L.E.P. Borges, C. Sievers, M.A. Fraga, The role of Brønsted and water-tolerant Lewis acid sites in the cascade aqueous-phase reaction of triose to lactic acid, *ChemCatChem*, 11 (2019) 3054-3063.
- [311] C.P. Yang, S. Xin, Y.X. Yin, H. Ye, J. Zhang, Y.G. Guo, An advanced selenium–carbon cathode for rechargeable lithium–selenium batteries, *Angew. Chem. Int. Ed.*, 52 (2013) 8363-8367.
- [312] K. Han, Z. Liu, J. Shen, Y. Lin, F. Dai, H. Ye, A free-standing and ultralong-life lithium-selenium battery cathode enabled by 3D mesoporous carbon/graphene hierarchical architecture, *Adv. Funct. Mater.*, 25 (2015) 455-463.
- [313] Y. Jiang, X. Ma, J. Feng, S. Xiong, Selenium in nitrogen-doped microporous carbon spheres for high-performance lithium–selenium batteries, *J. Mater. Chem. A*, 3 (2015) 4539-4546.
- [314] D.E. Mathew, S. Gopi, M. Kathiresan, G.J. Rani, S. Thomas, A.M. Stephan, A porous organic polymer-coated permselective separator mitigating self-discharge of lithium–sulfur batteries, *Mater. Adv.*, 1 (2020) 648-657.
- [315] J. Newman, N.P. Balsara, *Electrochemical systems*, 4th ed.; John Wiley & Sons: Hoboken, NJ, 2021.
- [316] P.G. Bruce, C.A. Vincent, Steady state current flow in solid binary electrolyte cells, *J. Electroanal. Chem. Interfacial Electrochem.*, 225 (1987) 1-17.
- [317] W. Xu, J. Wang, F. Ding, X. Chen, E. Nasybulin, Y. Zhang, J.G. Zhang, Lithium metal anodes for rechargeable batteries, *Energy Environ. Sci.*, 7 (2014) 513-537.
- [318] S. Ramesh, C.W. Liew, Dielectric and FTIR studies on blending of [xPMMA–(1– x) PVC] with LiTFSI, *Measurement*, 46 (2013) 1650-1656.
- [319] J. Zhao, L. Wang, X. He, C. Wan, C. Jiang, Determination of lithium-ion transference numbers in LiPF₆–PC solutions based on electrochemical polarization and NMR measurements, *J. Electrochem. Soc.*, 155 (2008) A292.
- [320] C. Li, B. Qin, Y. Zhang, A. Varzi, S. Passerini, J. Wang, J. Dong, D. Zeng, Z. Liu, H. Cheng, Single-Ion Conducting Electrolyte Based on Electrospun Nanofibers for High-Performance Lithium Batteries, *Adv. Energy Mater.*, 9 (2019) 1803422.
- [321] J. Evans, C.A. Vincent, P.G. Bruce, Electrochemical measurement of transference numbers in polymer electrolytes, *Polymer*, 28 (1987) 2324-2328.
- [322] B. Boz, H.O. Ford, A. Salvadori, J.L. Schaefer, Porous Polymer Gel Electrolytes Influence Lithium Transference Number and Cycling in Lithium-Ion Batteries, *J. Electron. Mater.*, 2 (2021) 154-173.
- [323] D. Huang, C. Liang, L. Chen, M. Tang, Z. Zheng, Z. Wang, MOF composite fibrous separators for high-rate lithium-ion batteries, *J. Mater. Sci.*, 56 (2021) 5868-5877.
- [324] Q. Xu, G. Hu, H. Bi, H. Xiang, A trilayer carbon nanotube/Al₂O₃/polypropylene separator for lithium-sulfur batteries, *Ionics*, 21 (2015) 981-986.
- [325] L.C. Merrill, H.O. Ford, J.L. Schaefer, Application of single-ion conducting gel polymer electrolytes in magnesium batteries, *ACS Appl. Energy Mater.*, 2 (2019) 6355-6363.
- [326] H.S. Dhatarwal, Y.-W. Chen, J.-L. Kuo, H.K. Kashyap, Mechanistic Insight on the Formation of a Solid Electrolyte Interphase (SEI) by an Acetonitrile-Based Superconcentrated [Li][TFSI] Electrolyte near Lithium Metal, *J. Phys. Chem. C*, 124 (2020) 27495-27502.
- [327] B. Wu, J. Lochala, T. Taverne, J. Xiao, The interplay between solid electrolyte interface (SEI) and dendritic lithium growth, *Nano Energy*, 40 (2017) 34-41.
- [328] X.-Y. Yue, W.-W. Wang, Q.-C. Wang, J.-K. Meng, Z.-Q. Zhang, X.-J. Wu, X.-Q. Yang, Y.-N. Zhou, CoO nanofiber decorated nickel foams as lithium dendrite suppressing host skeletons for high energy lithium metal batteries, *Energy Storage Mater.*, 14 (2018) 335-344.
- [329] H. Chu, H. Noh, Y.-J. Kim, S. Yuk, J.-H. Lee, J. Lee, H. Kwack, Y. Kim, D.-K. Yang, H.-T. Kim, Achieving three-dimensional lithium sulfide growth in lithium-sulfur batteries using high-donor-number anions, *Nat. Commun.*, 10 (2019) 1-12.

- [330] X. Fan, X. Ji, F. Han, J. Yue, J. Chen, L. Chen, T. Deng, J. Jiang, C. Wang, Fluorinated solid electrolyte interphase enables highly reversible solid-state Li metal battery, *Sci. Adv.*, 4 (2018) eaau9245.
- [331] M.-J. Kim, K. Yang, H.-J. Kang, H.J. Hwang, J.C. Won, Y.H. Kim, Y.-S. Jun, Polyimide-Coated Glass Microfiber as Polysulfide Perm-Selective Separator for High-Performance Lithium-Sulphur Batteries, *Nanomaterials*, 9 (2019) 1612.
- [332] Q. Zhao, Z. Hao, J. Tang, X. Xu, J. Liu, Y. Jin, Q. Zhang, H. Wang, Cation-Selective Separators for Addressing the Lithium–Sulfur Battery Challenges, *ChemSusChem*, 14 (2021) 792-807.
- [333] H. Yoon, P. Howlett, A. Best, M. Forsyth, D. Macfarlane, Fast charge/discharge of Li metal batteries using an ionic liquid electrolyte, *J. Electrochem. Soc.*, 160 (2013) A1629.
- [334] A. Best, A. Bhatt, A. Hollenkamp, Ionic liquids with the bis (fluorosulfonyl) imide anion: electrochemical properties and applications in battery technology, *J. Electrochem. Soc.*, 157 (2010) A903.
- [335] A. Bhatt, A. Best, J. Huang, A. Hollenkamp, Application of the N-propyl-N-methylpyrrolidinium Bis (fluorosulfonyl) imide RTIL Containing Lithium Bis (fluorosulfonyl) imide in Ionic Liquid Based Lithium Batteries, *J. Electrochem. Soc.*, 157 (2009) A66.
- [336] D. Lu, J. Tao, P. Yan, W. Henderson, Q. Li, Y. Shao, M. Helm, O. Borodin, G. Graff, B. Polzin, Formation of reversible solid electrolyte interface on graphite surface from concentrated electrolytes, *Nano Lett.*, 17 (2017) 1602-1609.
- [337] C. Ma, Y. Feng, F. Xing, L. Zhou, Y. Yang, Q. Xia, L. Zhou, L. Zhang, L. Chen, D. Ivey, A borate decorated anion-immobilized solid polymer electrolyte for dendrite-free, long-life Li metal batteries, *J. Mater. Chem. A*, 7 (2019) 19970-19976.
- [338] Q. Li, S. Zhu, Y. Lu, 3D porous Cu current collector/Li-metal composite anode for stable lithium-metal batteries, *Adv. Funct. Mater.*, 27 (2017) 1606422.
- [339] C.-Z. Zhao, X.-Q. Zhang, X.-B. Cheng, R. Zhang, R. Xu, P.-Y. Chen, H.-J. Peng, J.-Q. Huang, Q. Zhang, An anion-immobilized composite electrolyte for dendrite-free lithium metal anodes, *Proc. Natl. Acad. Sci. U.S.A.*, 114 (2017) 11069-11074.
- [340] H. Huo, B. Wu, T. Zhang, X. Zheng, L. Ge, T. Xu, X. Guo, X. Sun, Anion-immobilized polymer electrolyte achieved by cationic metal-organic framework filler for dendrite-free solid-state batteries, *Energy Storage Mater.*, 18 (2019) 59-67.
- [341] Y. Cui, A. Abouimrane, J. Lu, T. Bolin, Y. Ren, W. Weng, C. Sun, V.A. Maroni, S.M. Heald, K. Amine, (De) Lithiation mechanism of Li/SeS_x (x= 0–7) batteries determined by in situ synchrotron X-ray diffraction and X-ray absorption spectroscopy, *J. Am. Chem. Soc.*, 135 (2013) 8047-8056.
- [342] A. Abouimrane, D. Dambournet, K.W. Chapman, P.J. Chupas, W. Weng, K. Amine, A new class of lithium and sodium rechargeable batteries based on selenium and selenium–sulfur as a positive electrode, *J. Am. Chem. Soc.*, 134 (2012) 4505-4508.
- [343] S.S. Zhang, Role of LiNO₃ in rechargeable lithium/sulfur battery, *Electrochim. Acta*, 70 (2012) 344-348.
- [344] S.S. Zhang, Effect of discharge cutoff voltage on reversibility of lithium/sulfur batteries with LiNO₃-contained electrolyte, *J. Electrochem. Soc.*, 159 (2012) A920.
- [345] H. Lv, R. Chen, X. Wang, Y. Hu, Y. Wang, T. Chen, L. Ma, G. Zhu, J. Liang, Z. Tie, High-performance Li–Se batteries enabled by selenium storage in bottom-up synthesized nitrogen-doped carbon scaffolds, *ACS Appl. Mater. Interfaces*, 9 (2017) 25232-25238.
- [346] S. Jiang, Z. Zhang, Y. Lai, Y. Qu, X. Wang, J. Li, Selenium encapsulated into 3D interconnected hierarchical porous carbon aerogels for lithium–selenium batteries with high rate performance and cycling stability, *J. Power Sources*, 267 (2014) 394-404.
- [347] Y. Qu, Z. Zhang, S. Jiang, X. Wang, Y. Lai, Y. Liu, J. Li, Confining selenium in nitrogen-containing hierarchical porous carbon for high-rate rechargeable lithium–selenium batteries, *J. Mater. Chem. A*, 2 (2014) 12255-12261.


- [348] K. Han, Z. Liu, J. Shen, Y. Lin, F. Dai, H. Ye, A free-standing and ultralong-life lithium-selenium battery cathode enabled by 3D mesoporous carbon/graphene hierarchical architecture, *Adv. Funct. Mater.*, 25 (2015) 455-463.
- [349] Y. Zhao, M. Liu, W. Lv, Y.B. He, C. Wang, Q. Yun, B. Li, F. Kang, Q.H. Yang, Dense coating of Li₄Ti₅O₁₂ and graphene mixture on the separator to produce long cycle life of lithium-sulfur battery, *Nano Energy*, 30 (2016) 1-8.
- [350] M.H.A. Shiraz, H. Zhu, Y. Liu, X. Sun, J. Liu, Activation-free synthesis of microporous carbon from polyvinylidene fluoride as host materials for lithium-selenium batteries, *J. Power Sources*, 438 (2019) 227059.
- [351] S. Bai, X. Liu, K. Zhu, S. Wu, H. Zhou, Metal-organic framework-based separator for lithium-sulfur batteries, *Nat. Energy*, 1 (2016) 1-6.
- [352] Z. Li, L. Yin, MOF-derived, N-doped, hierarchically porous carbon sponges as immobilizers to confine selenium as cathodes for Li-Se batteries with superior storage capacity and perfect cycling stability, *Nanoscale*, 7 (2015) 9597-9606.
- [353] S. Li, H. Yang, R. Xu, Y. Jiang, Y. Gong, L. Gu, Y. Yu, Selenium embedded in MOF-derived N-doped microporous carbon polyhedrons as a high performance cathode for sodium-selenium batteries, *Mater. Chem. Front.*, 2 (2018) 1574-1582.
- [354] H. Chen, Y. Xiao, C. Chen, J. Yang, C. Gao, Y. Chen, J. Wu, Y. Shen, W. Zhang, S. Li, Conductive MOF-modified separator for mitigating the shuttle effect of lithium-sulfur battery through a filtration method, *ACS Appl. Mater. Interfaces*, 11 (2019) 11459-11465.
- [355] C. Qi, L. Xu, J. Wang, H. Li, C. Zhao, L. Wang, T. Liu, Titanium-containing metal-organic framework modified separator for advanced lithium-sulfur batteries, *ACS Sustain. Chem. Eng.*, 8 (2020) 12968-12975.
- [356] S. Suriyakumar, M. Kanagaraj, M. Kathiresan, N. Angulakshmi, S. Thomas, A.M. Stephan, Metal-organic frameworks based membrane as a permselective separator for lithium-sulfur batteries, *Electrochim. Acta*, 265 (2018) 151-159.
- [357] R. Fang, G. Zhou, S. Pei, F. Li, H.M. Cheng, Localized polyselenides in a graphene-coated polymer separator for high rate and ultralong life lithium-selenium batteries, *Chem. Commun.*, 51 (2015) 3667-3670.
- [358] F. Zhang, X. Guo, P. Xiong, J. Zhang, J. Song, K. Yan, X. Gao, H. Liu, G. Wang, Interface Engineering of MXene Composite Separator for High-Performance Li-Se and Na-Se Batteries, *Adv. Energy Mater.*, 10 (2020) 2000446.
- [359] K.S. Walton, R.Q. Snurr, Applicability of the BET method for determining surface areas of microporous metal-organic frameworks, *J. Am. Chem. Soc.*, 129 (2007) 8552-8556.
- [360] J. Rouquerol, P. Llewellyn, F. Rouquerol, Is the BET equation applicable to microporous adsorbents, *Stud. Surf. Sci. Catal*, 160 (2007) 49-56.
- [361] Y. Fang, J. Wen, G. Zeng, F. Jia, S. Zhang, Z. Peng, H. Zhang, Effect of mineralizing agents on the adsorption performance of metal-organic framework MIL-100 (Fe) towards chromium (VI), *Chem. Eng. J.*, 337 (2018) 532-540.
- [362] D. Wang, F. Jia, H. Wang, F. Chen, Y. Fang, W. Dong, G. Zeng, X. Li, Q. Yang, X. Yuan, Simultaneously efficient adsorption and photocatalytic degradation of tetracycline by Fe-based MOFs, *J. Colloid Interface Sci.*, 519 (2018) 273-284.
- [363] H. Dong, X. Zhang, Y. Lu, Y. Yang, Y.P. Zhang, H.L. Tang, F.M. Zhang, Z.D. Yang, X. Sun, Y. Feng, Regulation of metal ions in smart metal-cluster nodes of metal-organic frameworks with open metal sites for improved photocatalytic CO₂ reduction reaction, *Appl. Catal., B*, 276 (2020) 119173.
- [364] S. Wongsakulphasatch, W. Kiatkittipong, J. Saupsor, J. Chaiwisesphol, P. Piroonlerkgul, V. Parasuk, S. Assabumrungrat, Effect of Fe open metal site in metal-organic frameworks on post-combustion CO₂ capture performance, *Greenhouse Gases Sci. Technol.*, 7 (2017) 383-394.

- [365] A. Dhakshinamoorthy, M. Alvaro, H. Chevreau, P. Horcajada, T. Devic, C. Serre, H. Garcia, Iron (III) metal–organic frameworks as solid Lewis acids for the isomerization of α -pinene oxide, *Catal. Sci. Technol.*, 2 (2012) 324-330.
- [366] H. Chevreau, A. Permyakova, F. Nouar, P. Fabry, C. Livage, F. Ragon, A. Garcia-Marquez, T. Devic, N. Steunou, C. Serre, Synthesis of the biocompatible and highly stable MIL-127 (Fe): from large scale synthesis to particle size control, *CrystEngComm*, 18 (2016) 4094-4101.
- [367] N. Prasetya, A.A. Teck, B.P. Ladewig, Matrimid-JUC-62 and Matrimid-PCN-250 mixed matrix membranes displaying light-responsive gas separation and beneficial ageing characteristics for CO₂/N₂ separation, *Sci. Rep.*, 8 (2018) 2944.
- [368] R. Mukkabla, Kuldeep, K. Killi, S.M. Shivaprasad, M. Deepa, Metal Oxide Interlayer for Long-Lived Lithium–Selenium Batteries, *Chem. Eur. J.*, 24 (2018) 17327-17338.
- [369] X. Peng, L. Wang, X. Zhang, B. Gao, J. Fu, S. Xiao, K. Huo, P.K. Chu, Reduced graphene oxide encapsulated selenium nanoparticles for high-power lithium–selenium battery cathode, *J. Power Sources*, 288 (2015) 214-220.
- [370] Y. Jiang, X. Ma, J. Feng, S. Xiong, Selenium in nitrogen-doped microporous carbon spheres for high-performance lithium–selenium batteries, *J. Mater. Chem. A*, 3 (2015) 4539-4546.
- [371] H. Lv, R. Chen, X. Wang, Y. Hu, Y. Wang, T. Chen, L. Ma, G. Zhu, J. Liang, Z. Tie, J. Liu, Z. Jin, High-Performance Li–Se Batteries Enabled by Selenium Storage in Bottom-Up Synthesized Nitrogen-Doped Carbon Scaffolds, *ACS Appl. Mater. Interfaces*, 9 (2017) 25232-25238.
- [372] Q. Peng, F. Yu, W. Wang, A. Wang, F. Wang, Y. Huang, Ultralight polyethylenimine/porous carbon modified separator as an effective polysulfide-blocking barrier for lithium-sulfur battery, *Electrochim. Acta*, 299 (2019) 749-755.
- [373] H. Zhao, N. Deng, W. Kang, G. Wang, Y. Hao, Y. Zhang, B. Cheng, The significant effect of octa (aminophenyl) silsesquioxane on the electrospun ion-selective and ultra-strong poly-m-phenyleneisophthalamide separator for enhanced electrochemical performance of lithium-sulfur battery, *Chem. Eng. J.*, 381 (2020) 122715.
- [374] Y. Fan, Z. Niu, F. Zhang, R. Zhang, Y. Zhao, G. Lu, Suppressing the Shuttle Effect in Lithium–Sulfur Batteries by a UiO-66-Modified Polypropylene Separator, *ACS Omega*, 4 (2019) 10328-10335.
- [375] S. Bai, K. Zhu, S. Wu, Y. Wang, J. Yi, M. Ishida, H. Zhou, A long-life lithium–sulphur battery by integrating zinc–organic framework based separator, *J. Mater. Chem. A*, 4 (2016) 16812-16817.
- [376] S. Suriyakumar, A.M. Stephan, N. Angulakshmi, M.H. Hassan, M.H. Alkordi, Metal–organic framework@ SiO₂ as permselective separator for lithium–sulfur batteries, *J. Mater. Chem. A*, 6 (2018) 14623-14632.
- [377] M. Li, Y. Wan, J.K. Huang, A.H. Assen, C.E. Hsiung, H. Jiang, Y. Han, M. Eddaoudi, Z. Lai, J. Ming, Metal–organic framework-based separators for enhancing Li–S battery stability: mechanism of mitigating polysulfide diffusion, *ACS Energy Lett.*, 2 (2017) 2362-2367.
- [378] Y. He, Z. Chang, S. Wu, Y. Qiao, S. Bai, K. Jiang, P. He, H. Zhou, Simultaneously Inhibiting Lithium Dendrites Growth and Polysulfides Shuttle by a Flexible MOF-Based Membrane in Li–S Batteries, *Adv. Energy Mater.*, 8 (2018) 1802130.
- [379] M. Tian, F. Pei, M. Yao, Z. Fu, L. Lin, G. Wu, G. Xu, H. Kitagawa, X. Fang, Ultrathin MOF nanosheet assembled highly oriented microporous membrane as an interlayer for lithium-sulfur batteries, *Energy Storage Mater.*, 21 (2019) 14-21.
- [380] J. He, Y. Chen, A. Manthiram, Vertical Co₉S₈ hollow nanowall arrays grown on a Celgard separator as a multifunctional polysulfide barrier for high-performance Li–S batteries, *Energy Environ. Sci.*, 11 (2018) 2560-2568.

- [381] X.J. Hong, C.L. Song, Y. Yang, H.C. Tan, G.H. Li, Y.P. Cai, H. Wang, Cerium based metal–organic frameworks as an efficient separator coating catalyzing the conversion of polysulfides for high performance lithium–sulfur batteries, *ACS Nano*, 13 (2019) 1923-1931.
- [382] Z. Chang, Y. Qiao, J. Wang, H. Deng, P. He, H. Zhou, Fabricating better metal-organic frameworks separators for Li–S batteries: Pore sizes effects inspired channel modification strategy, *Energy Storage Mater.*, 25 (2020) 164-171.
- [383] Y. Cao, H. Wu, G. Li, C. Liu, L. Cao, Y. Zhang, W. Bao, H. Wang, Y. Yao, S. Liu, F. Pan, Z. Jiang, J. Sun, Ion Selective Covalent Organic Framework Enabling Enhanced Electrochemical Performance of Lithium–Sulfur Batteries, *Nano Lett.*, (2021) DOI: 10.1021/acs.nanolett.1021c00163.

APPENDICES

Chapter 2 Copyright clearance from the publisher



Catalytic isomerization of dihydroxyacetone to lactic acid by heat treated zeolites

Author: Md Anwar Hossain, Kyle N. Mills, Ashten M. Molley, Mohammad Shahinur Rahaman, Sartrawut Tulaphol, Shashi B. Lalvani, Jie Dong, Mahendra K. Sunkara, Noppadon Sathitsuksanoh

Publication: Applied Catalysis A: General

Publisher: Elsevier


Date: 5 February 2021

© 2020 Elsevier B.V. All rights reserved.

Journal Author Rights

Please note that, as the author of this Elsevier article, you retain the right to include it in a thesis or dissertation, provided it is not published commercially. Permission is not required, but please ensure that you reference the journal as the original source. For more information on this and on your other retained rights, please visit: <https://www.elsevier.com/about/our-business/policies/copyright#Author-rights>

Chapter 3 Copyright clearance from the publisher



Catalytic cleavage of the β -O-4 aryl ether bonds of lignin model compounds by Ru/C catalyst

Author: Md Anwar Hossain, Thanh Khoa Phung, Mohammad Shahinur Rahaman, Sartrawut Tulaphol, Jacek B. Jasinski, Noppadon Sathitsuksanoh

Publication: Applied Catalysis A: General

Publisher: Elsevier

Date: 25 July 2019

© 2019 Elsevier B.V. All rights reserved.

Journal Author Rights

Please note that, as the author of this Elsevier article, you retain the right to include it in a thesis or dissertation, provided it is not published commercially. Permission is not required, but please ensure that you reference the journal as the original source. For more information on this and on your other retained rights, please visit: <https://www.elsevier.com/about/our-business/policies/copyright#Author-rights>

Chapter 5 Copyright clearance from the publisher

Metal–Organic Framework Separator as a Polyselenide Filter for High-Performance Lithium–Selenium Batteries



Author: Md. Anwar Hossain, Sarttrawut Tulaphol, Arjun K. Thapa, et al

Publication: ACS Applied Energy Materials

Publisher: American Chemical Society

Date: Dec 1, 2021

Copyright © 2021, American Chemical Society

PERMISSION/LICENSE IS GRANTED FOR YOUR ORDER AT NO CHARGE

This type of permission/license, instead of the standard Terms and Conditions, is sent to you because no fee is being charged for your order. Please note the following:

- Permission is granted for your request in both print and electronic formats, and translations.
- If figures and/or tables were requested, they may be adapted or used in part.
- Please print this page for your records and send a copy of it to your publisher/graduate school.
- Appropriate credit for the requested material should be given as follows: "Reprinted (adapted) with permission from {COMPLETE REFERENCE CITATION}. Copyright (YEAR) American Chemical Society." Insert appropriate information in place of the capitalized words.
- One-time permission is granted only for the use specified in your RightsLink request. No additional uses are granted (such as derivative works or other editions). For any uses, please submit a new request.

If credit is given to another source for the material you requested from RightsLink, permission must be obtained from that source.

[BACK](#)

[CLOSE WINDOW](#)

CURRICULUM VITAE

Md. Anwar Hossain

216 Eastern Parkway, Louisville, KY 40292 | 530-567-9276 | hossain.anwarcep13@gmail.com
| <http://tikgroup.org/anwar-hossain>

Summary

- 5.5+ years of experience in developing energy storage systems and noble catalysts.
- Extensive experience in cathode material synthesis and characterization.
- Hands-on experience in non-flammable, hybrid solid electrolyte development.
- Highly skilled multidisciplinary researcher with proven problem-solving skills.

Education

Doctor of Philosophy in Chemical Engineering University of Louisville, Louisville, KY	Apr. 2022 (expected)
Master of Engineering in Chemical Engineering University of Louisville, Louisville, KY	Dec. 2018
Bachelor of Science in Chemical Engineering Shahjalal University of Science and Technology, Sylhet, Bangladesh	Dec. 2012

Research experience

Ph.D. Student Researcher | University of Louisville

Material synthesis: (MOF, Zeolites, NMC, LFP, Solid & Liquid electrolyte)

Identified the desired properties of the materials for catalysis and energy storage.

- Synthesized transition metal oxide, Zeolites, and metal-organic framework (MOFs) using Solvothermal and Hydrothermal techniques.
- Tuned oxygen vacancy of metal oxide, zeolites utilizing solid-state reaction.
- Synthesized various cathode materials (NMC 811, NMC 622, and LFP) via the co-precipitation method.
- Developed Lewis acid-functionalized hybrid solid electrolyte with approximate conductivity of 10^{-3} S/cm.
- Invented bio-based organic deep eutectic solvent for Li-metal battery electrolyte.
- Invented Hybrid Solid electrolyte for the Li-metal battery.

Energy Storage: (*Li-Se, Li-LFP, Li-NMC cell*)

Investigated the challenges in developing high-energy-density rechargeable batteries.

- Invented non-flammable bio-based electrolytes with conductivity over 10^{-3} S/cm, wider temperature range (4°C to 70°C), and large potential window (up to 5.5V).
- Developed MOF functionalized separator for Li-selenium battery to achieve high-capacity retention over 500 charge-discharge cycles.
- Studied the derived hybrid solid electrolyte for Li-ion battery achieving capacity retention over 94% after 200 cycles.
- Assembled pouch cell with 1000mAh capacity to test developed materials.

Catalysis: (*Homogenous & Heterogeneous catalysis, Gas-phase, Packed bed reactor*)

Identified the active site for the catalytic up-gradation of lignin to valuable chemicals.

- Built a microreactor system integrated with online GC for catalyst screening and acid site determination.
- Discovered self-hydrogen transfer hydrogenolysis of lignin over metal oxide catalyst.
- Developed bio-based deep eutectic solvent for biomass pretreatment.
- Led a team to research hydrocracking, isomerization, and ketonization.

B.Sc. Student Researcher | Shahjalal University of Science and Technology, Sylhet, Bangladesh

Groundwater purification process for rural areas of Bangladesh by utilizing up-flow filtration system.

- Designed and fabricated all components of a water purification plant.
- Collected and graded adsorption materials based on their size.
- Coated filter materials with absorbent to remove arsenic.
- Developed a UV treatment process to kill bacteria in the treated water.

Technical Skills

Materials characterization: (*SEM, FTIR, NMR, XPS, ICP, UV-Vis, EIS, CV, LSV*)

- **Physical and structural properties:** Temperature program reduction (TPR), Temperature program oxidation (TPO), Thermogravimetric analysis (TGA), Temperature program disruption (TPD), Scanning electron microscopy (SEM), X-ray Photoelectron Spectroscopy (XPS), Inductively coupled plasma mass spectrometry (ICP-MS), NMR, UV-Vis, BET, FTIR, Raman, and XRD.

- **Electrochemical:** Electrochemical Impedance Spectroscopy (EIS), Cyclic voltammetry (CV), Linear sweep voltammetry (LSV), chronopotentiometry, Galvanostatic charge-discharge.

Laboratory Management: (*High-pressure reactor, Packed bed, Electrospinning*)

- **Operation and troubleshooting:** chromatographic equipment (GC and HPLC).
- **Reactor design and operation:** micro, packed bed, and high-pressure reactors.
- **Set-up:** Custom build Electrospinning set-up for lignin nano-fiber synthesis.
- **Set-up:** Micro Plasma reactor set-up for plastic depolymerization.

Computational: Reaction pathways, mechanisms, and kinetics.

Process simulation: PRO/II, ASPEN PLUS, CHEMCAD

Patents/ Discloser

1. Primary inventor on a provisional patent filed 27th November 2020 by University of Louisville “*Biomass-based solid composite electrolytes for batteries*”
2. Primary inventor on a provisional patent filed by University of Louisville “*CH₄-assisted catalytic hydrodeoxygenation of oxygenates over ZnO-MoO₃/TiO₂ catalysts*”
3. Primary Inventor on a provisional patent filed by University of Louisville “*CO₂-promoted catalyst-free dehydration of sorbitol leading to high 1,4-sorbitan selectivity*”

Publications Journals

1. **M.A. Hossain**, S. Tulaphol, A.K. Thapa, J. Jasinski, H. Wang, M.K. Sunkara, K. Ozdemir, N. Sathitsuksanoh “*Suppressing shuttling of lithium polyselenides by metal-organic framework-based separators*” ACS Appl. Energy Mater., 10.2021/acsaem.1c01806
2. **M.A. Hossain**, M.S. Rahaman, S. Tulaphol, D. Yelle, H. Shang, Z. Sun, S. Renneckar, N. Sathitsuksanoh “*Effects of polyol-based deep eutectic solvents on efficiency of rice straw enzymatic hydrolysis*” Ind. Crops Prod. 167 (2021) 113480.
3. **M.A. Hossain**, K.N. Mills, A.M. Molley, M.S. Rahaman, S. Tulaphol, S.B. Lalvani, J.Dong, M.K. Sunkara, N. Sathitsuksanoh “*Catalytic isomerization of dihydroxyacetone to lactic acid by heat treated zeolites,*” Appl. Catal. A,1

- 611, 117979 (2021).
4. **M.A. Hossain**, A.K. Tharpa, S. Tulaphol, H. Wang, M. Sunkara, and N. Sathitsuksanoh, *Deep Eutectic electrolytes for high-temperature lithium-ion batteries* (Under review).
 5. **M.A. Hossain**, S. Tulaphol, A.K. Thapa, J. Jasinski, H. Wang, M.K. Sunkara, N. Sathitsuksanoh: *Metal-Organic framework-based hybrid electrolyte for Li-ion battery*” (in preparation).
 6. M. S. Rahaman, S.Tulaphol, **M. A. Hossain**, C. Evrard, L. M. Thompson, and N. Sathitsuksanoh “ Kinetics of phosphotungstic acid-catalyzed condensation of levulinic acid with phenol to diphenolic acid: Temperature-controlled regioselectivity” *Molecular Catalysis* 514, 111848.
 7. M.S. Rahaman, S. Tulaphol, K. Mills, **M. A. Hossain**, Daniel Yelle, T. Maihom, N. Sathitsuksanoh “Metal triflates formation of C12-C22 phenolic compounds by simultaneous C-O breaking and C-C coupling of lignin-derived benzyl phenyl ether,” *Dalton Trans.*, 2021, 50, 17390-17396.
 8. M.S. Rahaman; S. Tulaphol; **M.A. Hossain**; J.Jasinski; N. Sun; A. George; B. Simmons; T. Maihom; M. Crocker; N. Sathitsuksanoh ”Cooperative Brønsted-Lewis acid sites created by phosphotungstic acid encapsulated metal-organic frameworks for selective glucose conversion to 5-hydroxymethylfurfural” *Fuel*, 2021, 122459
 9. M. S. Rahaman, T. K. Phung, **M.A. Hossain**, E. Chowdhury, S. Tulaphol, M. O’Toole, G. A. Willing, J. B. Jasinski, M. Crocker, & N. Sathitsuksanoh “*Hydrophobic functionalization of HY zeolites for efficient conversion of glycerol to solketal,*” *Appl. Catal. A*, 592, 117369 (2020).
 10. **M.A. Hossain**, M.S. Rahaman, D. Lee, T.K. Phung, C.G. Canlas, B.A. Simmons, S. Renneckar, W.Reynolds, A.George, S. Tulaphol, N. Sathitsuksanoh “*Enhanced Softwood Cellulose Accessibility by H3PO4 Pretreatment: High Sugar Yield without Compromising Lignin Integrity,*” *Ind. Eng. Chem.* 59 (2), 1010-1024 (2019).
 11. S. Tulaphol, **M.A. Hossain**, M. S. Rahaman, L. Liu, T. K. Phung, S. Renneckar, N. Grisdanurak & N. Sathitsuksanoh “*Direct production of levulinic acid in one pot from hemp hurd by dilute acid in ionic liquids,*” *Energy & Fuels* 34 (2), 1764-1772(2019).
 12. **M.A. Hossain**, T.K Phung, M.S. Rahaman, S. Tulaphol, J. Jasinski, N. Sathitsuksanoh “*Catalytic cleavage of the β -O-4 aryl ether bonds of lignin model compounds by Ru/C catalyst,*” *Appl. Catal. A*, 582, 117100 (2019).
 13. **M.A. Hossain**, T.Sae-Lee, T.K. Phung, M.S. Rahaman, S. Tulaphol, S.Praserthdam, N. Sathitsuksanoh “*Origin of cleavage of lignin β -O-4 over Ru/C and evidence of the Meerwein–Ponndorf–Verley reaction*” (under review).
 14. **M.A. Hossain**, M. S. Rahaman, S. Tulaphol, J.B. Jasinski, N. Sathitsuksanoh “*Reducible metal oxide catalyzed hydrogenolysis of lignin model compounds*” (under review).
 15. **M. A. Hossain**, L. Mushill, M. S. Rahaman, S. M. Mains, T. Vickers, S. Tulaphol, J. Dong, N. Sathitsuksano “*Upcycling agricultural waste to biodegradable polyhydroxyalkanoates by combined ambient alkaline treatment and bacterial fermentation*” (under review)

16. **M.A. Hossain**, B. Karki, R. K Hona, N. Sathitsuksanoh, A. K. Thapa “Mn-Rich NMC as Cathode Materials for High Voltage Sodium-Ion Batteries” (in preparation)

Selected presentations:

1. 2019 AIChE Annual Meeting, Orlando, Florida, Enhancing Lactic Acid Production from the Dihydroxyacetone by Extra Framework Alumina.
2. 2018 Frontiers in Biorefining, St. Simons Island, Georgia, November 5 – 8, 2018, Hossain MA, Sathitsuksanoh N., “Novel bioderived solvents for processing lignocellulose”.
3. AIChE 2017 Annual Meeting, Minneapolis, MN, October 29-November 3, 2017. Phung T.K., Hossain M.A., Prasomsri T., Sathitsuksanoh N., “Isosorbide production from aqueous sorbitol solution over Silica-Alumina”.

Media/ news coverage

- AZO Materials, September-30-2020- MOFs help to form a safer horizon for Li-ion batteries.
- Biofuel digest-April-13-2020, From weeds to wealth.

Awards & honors

- Doctoral Dissertation Completion Award, University of Louisville, Spring 2022
- Graduate Research Grant, Graduate Student Council, University of Louisville, 2019
- Frontier in Biorefining (FIB) Award for the 2018 Frontier in Biorefining Meeting, 2018
- Graduate Student Council (GSC) Travel Funds, University of Louisville, 2017
- Grosscurth Fellowship, University of Louisville, 2017
- R3 Conference travel grant, Conn Center, University of Louisville, 2017
- Pullin Fellowship, University of Louisville, 2016

Teaching & mentoring

During my Ph.D. my teaching experience is divided in two sections. Since 2018, I worked as a teaching assistant (TA) for several courses and mentored over 50 students for their research projects. Below are the courses I was TA for.

- Material Science.

- KIN Chemical Reactor.
- Unit Operation.

Students I mentored for their research were from high school to graduate level.
Some of them have publications with me.

Extra-curricular activities

General secretary of the Bangladeshi student Association UofL (2018-2019)

Chemical Engineering student representative of Graduate Student Council (2018)